Spontaneous Cluster Formation in Stoichiometric Quantum Critical Systems

---

A Dissertation

presented to

the Faculty of the Graduate School

University of Missouri

In Partial Fulfillment

of the Requirements for the Degree

Doctor of Philosophy

---

by

Alex Bretaña

Dr. Wouter Montfrooij, Dissertation Supervisor

May 2022

The undersigned, appointed by the Dean of the Graduate School, have examined the dissertation entitled

Spontaneous Cluster Formation in Stoichiometric Quantum Critical Systems

presented by Alex Bretaña, a candidate for the degree of Doctor of Philosophy of Physics, and hereby certify that in their opinion it is worthy of acceptance.

Dr. Wouter Montfrooij

Dr. Deepak Singh

Dr. David Singh

Dr. Carlos Wexler

Dr. Heather Hunt

DEDICATION

I would like to thank my wife Nicole Bretaña, without her guidance, her patience, her support, and most importantly her love, I would not have had the motivation to complete my dissertation. Thank you for all the long days, the tireless nights, and putting up with me for all these years.

I would also like to thank my immediate family, my parents Rose and Mark and my sister Jessica for their guidance, instruction, and love for the past 28 years. You helped me to grow and yet always pushed me when I needed it.

A special thank you to all my pets, my cats and fish for their love, company, and continued distractions.

A final thank you to all my friends and family members whom have shown me support and encouragement over these past few years.

ACKNOWLEDGMENTS

I would first like to thank Dr. Wouter Montfrooij and my research partner Dr. Sean Fayfar. I could try and list the innumerable things you both have done to help support and guide my research but I know with certainty I would miss a few. Just some of the big things which stick out, never giving up on me, always encouraging me to do my best work, and always pushing me to be a better scientist, thank you for it all.

I would next like to thank Dr. Thomas Heitmann and my thesis committee, Dr. Heather Hunt, Dr. Deepak Singh, Dr. David Singh, and Dr. Carlos Wexler for their critique and feedback without such I would not be the scientist I am today. I would also like to thank them for all their time spent answering my many, many questions.

I would also like to thank Dr. Karen King, Dr. Yun Zhang, Dr. Jesse Kremenak, and Dr. Dorina Kosztin for passing on their expertise and knowledge in teaching and instructing students. Your lessons have been invaluable in developing my teaching methodology.

A special thank you to Dr. Guang Bian and his student Jacob Cook for their help in performing ARPES measurements as well as Dr. Kurt Brorsen and his student Muhammad Ardiansyah for their help running DFT simulations on various cuprate structures.

A final thank you to everyone in the Physics and Astronomy Department at the University of Missouri, from my fellow graduate students to the tireless support staff, I would not have been able to keep my motivation going if it wasn't for your support.

Contents

List of Figures

Spontaneous Cluster Formation in Stoichiometric Quantum Critical Systems

Alex Bretaña

Dr. Wouter Montfrooij, Dissertation Supervisor

ABSTRACT

Metallic systems with magnetic ions embedded which have been prepared to undergo a second-order phase transition at zero Kelvin (called the quantum critical systems) historically appear to fall into two distinct categories: (chemically) heavily-doped systems in which the unusual properties can be attributed to a disorder-induced distribution of Kondo shielding temperatures, and (nearly) stoichiometric systems where the departures from Fermi-liquid theory have been attributed to intrinsic instabilities. We show that this distinction between doped and stoichiometric systems is no longer a clear-cut boundary and that magnetic clusters associated with a distribution of Kondo shielding temperatures found in the heavily doped quantum critical $Ce(Fe_{0.755}Ru_{0.245})_2Ge_2$ are also present in $CeRu_2Si_2$, a stoichiometric system close to a quantum critical point.

By revisiting published data on $CeRu_2Si_2$ and comparing them to the results of $Ce(Fe_{0.755}Ru_{0.245})_2Ge_2$, we show that clusters consisting of Ce-ions with their moments aligned with their neighbors exist in both systems at low temperatures and dominate the macroscopic response of these systems. We show these clusters form from a distribution of Kondo shielding temperatures which naturally arises from a distribution in inter-ionic separations; the chemical doping of ruthenium in $Ce(Fe_{0.755}Ru_{0.245})_2Ge_2$ and zero-point motion in stoichiometric $CeRu_2Si_2$. We show that the dominant physics which drives heavily-doped systems, namely spontaneous formation of mag-

netic clusters, also plays a leading role in the response of homogenous systems.

We investigate the presence of these spontaneous clusters in the heavily studied $YbRh_2Si_2$ where neutron scattering data have not been published. We show that the specific heat and susceptibility are naturally interpreted when ordered magnetic clusters are taken into account. Thus, cluster formation appears to be ubiquitous at the quantum critical point.

We end with potential implications of the findings (that small changes in inter-ionic separations ends up dominating the macroscopic response) to another class of highly correlated electron systems: the cuprate high T_c superconductors. We speculate that ionic displacements associated with hole doping leads to a pathway for the formation of Cooper pairs. We show that this pathway leads to an explanation for the many experimental observations, such as the striped phase and the hourglass dispersion.

Chapter 1

Introduction to Cluster Formation in Quantum Critical Systems

1.1 Introduction

We begin with an introduction into the dominant physics at play in cluster formation. We introduce Fermi-liquid theory, the Ruderman-Kittel-Kasuya-Yoshida (RKKY) interaction, and Kondo shielding. We show that cluster formation is rooted in a distribution of interatomic separations, which upon cooling, naturally leads to a distribution of Kondo shielding temperatures and percolation physics. We show that the introduction of finite size effects leads to the ordering of neighboring moments within the clusters that form upon cooling.

We use published data and results on heavily doped $Ce(Fe_{0.755}Ru_{0.245})_2Ge_2$ and show that these clusters consisting of Ce-ions with their moments aligned with their neighbors dominate the low temperature macroscopic response. We show that these clusters form from a distribution of Kondo shielding temperatures which naturally arises from a distribution in inter-ionic separations; the chemical doping of ruthenium in $Ce(Fe_{0.755}Ru_{0.245})_2Ge_2$.

1.2 Fermi Liquids and Strange Metals

In the early 90's, unexplained behavior in the resistivity was seen upon cooling certain metals[2]; at the root of this unexplained behavior is the quirky little particle known as an electron which must be described quantum mechanically. Electrons have both a particle and wavelike nature; therefore, a quantum mechanical wave function must be used to describe them. As such, we cannot determine the exact location of an electron inside a metal, we must use a probabilistic approach to finding the electron at any given location. The mathematical function that describes the probability of finding an electron at any specified location inside an atom is called an atomic orbital. These orbitals are characterized by three quantum numbers which describe the state of the electrons inside the orbital. Atomic orbitals are commonly labeled s, p, d, and f orbitals; each of which refers to the value of l, the eigenvalue of the angular momentum operator, where $l = 0, 1, 2, 3$ for each orbital s, p, d, and f respectively. Electrons also have a half integer spin creating a small magnetic moment associated with the electron. Half integer spins mean electrons are fermions thereby obeying Fermi-Dirac statistics as well as the Pauli Exclusion principle. Therefore, no two electrons can occupy the same quantum state. As such, each electron in a metal will fill a single state thereby making the ground state of any metal a "sea" of electrons all filling the lowest available energy states all the way up to the highest energy state for the final electron. This occupied final energy level in the ground state is known as the Fermi level, and is denoted as E_f[1].

In order to create a low temperature excitation in a metal, an electron below E_f must become excited to above E_f leaving behind an "electron hole". For an electron

with an initial energy E_i near the Fermi level to occupy a state above the Fermi level, the electron would need to be excited with enough energy E, such that $E_i + E \rightarrow E_f$. Therefore only electrons whose energies are close to E_f can be excited to unoccupied states above E_f and as a consequence only a small number of electrons contribute to the macroscopic properties of a metal. The range or bands of energy that cross the Fermi level are known as conduction bands and electrons which occupy states in the conduction band are known as conduction electrons. If an electron did become excited to a new state above E_f, the initial E_i would become unoccupied thereby creating an "electron hole"[1].

Ultimately, to accurately describe a metal at low temperatures, we must take into account the unique properties of the electron as well as the excitations and interactions these electrons and "electron holes" have with each other. In essence, we must describe the behavior of a group of interacting electrons. In 1956, Lev Davidovich Landau[3] proposed these strongly interacting electrons can be described as a "weakly" interacting degenerate gas of "quasiparticles" by assuming the electrons' interactions with the entirety of the metal lattice can be captured through an effective mass of the electron m^*. Landau first considered a non-interacting system of fermions (i.e. electrons) referred to as a Fermi gas. Landau then hypothesized that if we "turn on" interactions between these fermions, then the ground state of the Fermi gas would adiabatically transform into the ground state of the interacting system. When this interaction is "turned on" in the Fermi gas, the charge, momentum, and spin of the fermions remain unchanged, but the dynamic properties are renormalized to new values. This leads to a one-to-one correspondence in the excitations of the non-

interacting Fermi gas to the excited states of the interacting system. These excited states are known as "quasiparticles".

The one-to-one correspondence between a Fermi gas and the interacting system led Landau to theorize that the excitations at low temperatures in metals can be described using the mathematical framework of a non-interacting Fermi gas through these quasiparticle excitations (quasi-excitations); this model is known as Fermi liquid theory (FLT) and describes the low temperature behavior of metals. Considering the case in which the quasiparticles interact (the interaction has been "turned on"), we obtains the corresponding magnetic susceptibility χ, the specific heat c_V and the resistivity ρ as

$$\chi = \frac{m^* p_F \mu_B^2}{4\pi^2 \hbar} \frac{1}{1 + F_0^A} \tag{1.1}$$

$$c_V = \left(\frac{\partial S}{\partial T}\right)_V = \frac{m^* p_F}{3\hbar^3} {k_B}^2 T \tag{1.2}$$

$$\rho(T) \sim T^2 \tag{1.3}$$

where μ_B is the Bohr magneton, p_F is the Fermi momentum, k_B is the Boltzmann constant, T is the temperature, and m^* is the effective mass of the electron reflecting its interactions with the entirety of the metal lattice. The class of systems that were discussed in the 90's were characterized by very large values of m^*[2] and therefore these systems are known as heavy fermions. F_0^A is the Landau Fermi Liquid parameter and parametrizes the collective interactions between quasiparticles. Fermi liquid theory only works when strongly interacting electrons can be modeled as a group

of "weakly" interacting quasiparticles, but what happens when the strength of the interaction becomes so strong this model no longer holds?

As the interactions between quasiparticles get stronger and stronger, FLT breaks down entirely and exotic new phenomena emerge, such as superconductivity. These materials where Eq. 1.1-1.3 no longer hold are known as non-Fermi liquids (nFl) or sometimes "strange metals" for their unique properties[1]. nFl behavior can be observed experimentally in the specific heat, uniform susceptibility, resistivity and the dynamic susceptibility where E/T-scaling has been observed in some systems [7–10].

1.3 Magnetic Ordering vs Shielding

Fermi-liquid theory breaks down when quasiparticles are interacting too strongly; two such interactions that play a critical role in the formation of magnetic clusters are the Ruderman-Kittel-Kasuya-Yoshida (RKKY) interaction[4–6] which is responsible for the formation of long range order, and Kondo shielding [20][21] which is responsible for the prevention/destruction of long range order by shielding of magnetic moments.

The RKKY interaction is a long range coupling mechanism mediated by conduction electrons, in which two local (neighboring) magnetic moments align with each other. Conduction electrons can scatter off of magnetic moments after which the conduction electron's own magnetic moment reflects the direction of the magnetic moment it scattered off of. In other words, the conduction electron has become polarized by the magnetic moment via the exchange interaction, the strength of which is denoted as J. These newly reorientated conduction electrons continue to move through the material and by scattering off of a second magnetic moment, they effectively mediate an interaction between the first and second magnetic moments,

orientating their moments to be parallel with each other (ferromagnetic) or antiferromagnetic or even a more complicated incommensurate arrangement reflecting the topology of the Fermi surface[1]. This interaction with the second moment again involves the exchange interaction, and therefore the strength of the RKKY interaction, J_{RKKY}, is proportional to J^2. It is also oscillatory in nature and depends on the separation between magnetic ions (Appendix A). We note here that the RKKY interaction is an effective interaction between two neighboring magnetic moments and not between conduction electrons, it is only mediated by the conduction electrons. In competition with the RKKY interaction and the ordering of neighboring magnetic moments is Kondo shielding.

Kondo shielding was first proposed by J. Kondo [11]: conduction electrons interact so strongly with the magnetic moments that they become localized around the magnetic moments, thereby shielding the magnetic moment by having their intrinsic moment aligned opposite. Kondo was the first to describe the ability of conduction electrons to form a magnetic singlet with the magnetic ion (an ion is an atom or molecule with a net electric charge and a magnetic singlet refers to having the conduction electron(s) having their moments aligned antiparallel)[1]. While the Kondo model is accurate at high temperatures, the resistivity diverges upon cooling due to the model's logarithmic increase in scattering between conduction electrons and the magnetic impurity. Phillip Anderson[72] and Kenneth Wilson[13] later refined the Kondo Model, such that the strength J of the exchange interaction increases upon cooling while the magnitude of the scattering does not logarithmically increase thereby solving the low temperature divergence of the resistivity. Thus, upon cooling

a metal, the interaction between conduction electrons and magnetic moments begins to increase, until at a specific temperature, known as the Kondo Temperature T_k[11], the conduction electrons will find it energetically favorable to become localized around magnetic moments forming a singlet state (technically this is not entirely true as the cloud of electrons around a magnetic impurity is dynamic, meaning electrons are constantly leaving, while others are becoming localized around that same magnetic impurity). The Kondo temperature T_K depends on the bandwidth D of the conduction band, on the strength of the exchange interaction J, and on the density of states at the Fermi level ρ as[11]

$$T_K = De^{-1/\rho|J|}. \tag{1.4}$$

As the metal is cooled further, more and more conduction electrons become localized around magnetic impurities, in other words, the conduction electrons act as if they have become very massive. Due to the alignment of a localized conduction electron's spin being antiparallel to the direction of the magnetic impurity it is localized around, the more conduction electrons that bunch up around a single magnetic ion, the smaller its moment effectively becomes. This process is known as Kondo shielding and can become so strong that an ion's magnetic moment will become completely shielded by the conduction electrons and will cease to be magnetic[20, 21]. We make a small note here that Kondo shielding is a dynamic process and is not solely associated with the onset of T_K but happens gradually over the course of several decades of temperature.

Ultimately as we cool a metal down, there is direct competition between magnetic ordering through the RKKY interaction and shielding of the same moments through Kondo shielding. As both these interactions are rooted in the same exchange inter-

action between conduction electrons and magnetic moments, it is the strength of the exchange interaction J that will determine the ground state of the system. If J is large, the conduction electrons will favor becoming localized around a single electron and Kondo shielding will dominate leading to a disordered phase i.e., short range correlations and heavy-fermion behavior as displayed in Fig. 1.1. If J is small, the conduction electrons are not as strongly attracted to the magnetic moments and can move more freely through the lattice leading the RKKY interaction to dominate and long range order to emerge as shown in Fig. 1.1. Therefore, extremely small changes to the strength of the exchange interaction J can drive the system towards ordered or disordered behavior when it is delicately poised between these two regimes.

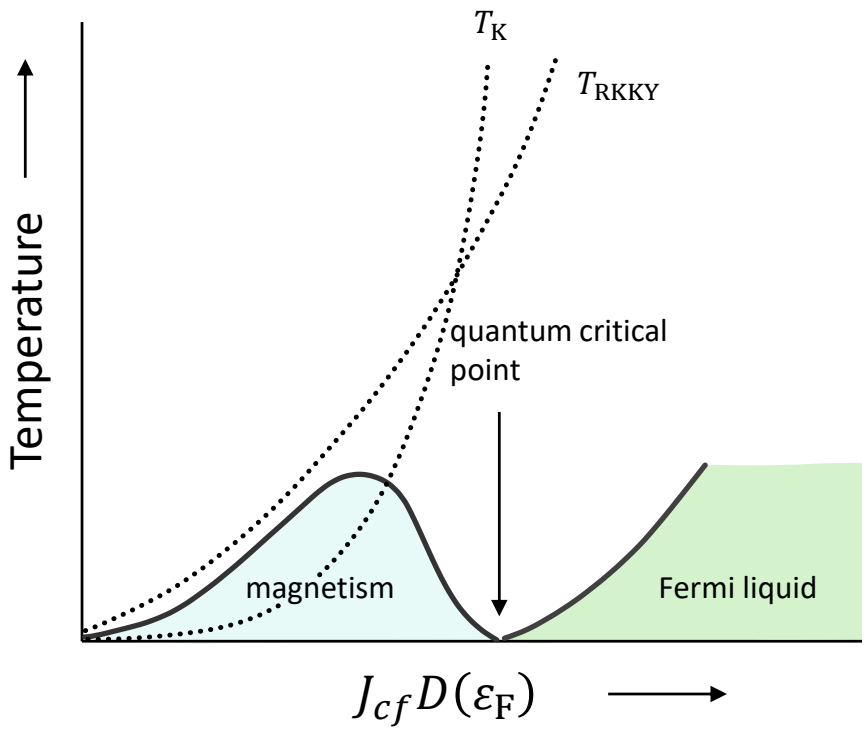

Figure 1.1: Doniach phase diagram [39] adapted from [54] showing the competition between order (the RKKY interaction) and disorder (the Kondo shielding mechanism). J_{cf} is the exchange interaction strength between conduction electrons and f-orbital electrons of a rare Earth ion. $D(\epsilon_F)$ is the electron density of states at the Fermi energy $D(\epsilon_F)$.

1.4 Quantum Critical Systems and Percolation

When the competition between magnetic ordering and shielding (disorder) persists all the way down to 0 K, systems end up neither in an ordered nor disordered phase but instead at the the so-called quantum critical point (QCP). This is shown in Fig. 1.1. In this region, these systems display low-temperature responses that do not follow Fermi Liquid theory and thus are non-Fermi liquids in this critical region. In a magnetic system, a change from longe-range magnetic order to disordered behavior (or vice versa) is known as a magnetic phase transition. When the phase transition occurs at 0 K, these systems are referred to as quantum critical systems. Since phase transitions at 0 K are not driven by thermal fluctuations, they (should) fall into new universality classes. Such second order (continuous) phase transitions are referred to as quantum phase transitions. We show a typical Doniach phase diagram in Fig. 1.1[39]. From Fig. 1.1 we see that for high J, Kondo shielding dominates and we end up with Fermi-liquid and heavy fermion behavior, while for small J the RKKY interaction dominates resulting in long range order. However, if the competition between order and disorder survives all the way down to 0 K, we end up in a non-Fermi liquid regime at the quantum critical point.

In nature, most materials are not quantum critical, however, there are two common methods we can use to tweak or push a material towards the quantum critical point; hydrostatic pressure and chemical pressure (doping). Hydrostatic pressure compresses the material such that the ions are pushed just a little closer together. This directly affects the atomic orbital overlap between neighboring ions. The strength of the exchange interaction J depends extremely sensitively on this orbital overlap and

therefore, applying hydrostatic pressure allows increases J. This increase in J will drive the system towards the Fermi liquid regime where Kondo shielding dominates (Fig. 1.1). "Life finds a way" and in some rare cases, applying just a small amount of hydrostatic pressure is enough to affect the exchange interaction J to the point the system ends up at the QCP. However, in most cases the amount of pressure required is immense and difficult to implement for large single crystal samples and thus, chemical doping is preferred.

In the case of chemical pressure, we substitute an atom in the material with another similar (iso-electronic, meaning the same number of valence electrons) atom of different size. In order to not affect the magnetic ions, a smaller (or larger) iso-electronic atom is used to substitute for a non-magnetic atom. Doping larger atoms generally increases inter-atomic separations while doping smaller atoms generally decreases inter-atomic separations, both of which directly affect inter-atomic separations. This in turn alters the orbital overlap between neighboring atoms and subsequently changes the strength of the exchange interaction J, driving the material towards an ordered or disordered phase (closer to the QCP). Chemical doping is considered to be "dirty", as we can never be sure how the microscopic properties of the material change by introducing new atoms. However from this point on, we will focus solely on chemical doping as this is (in practice) how large samples are prepared to be at the QCP. In such a chemically doped system, the doped atoms are randomly substituted throughout the material and therefore we end up with a local distribution (local meaning in the vicinity of the doped atom) of inter-atomic separations as some atoms are pushed closer together while other atoms are forced further apart.

In practice, systems that have been tuned to be at the QCP fall into two categories, and the efforts at a theoretical understanding of the low temperature response of these systems reflect this dichotomy. On the one hand there exist (nearly) stoichiometric compounds whose composition is already so close to a QCP that they can be fine-tuned to be exactly at the quantum critical point by applying hydrostatic pressure, or by small amounts of chemical substitution to expand or shrink the lattice, thereby affecting the degree of orbital overlap in order to achieve the fine-tuning. Naturally, these systems have received the bulk of theoretical attention and various theories have been forwarded to describe the low-temperature response either as a localized instability against moment formation[16] or as a collective instability against ordering rooted in the topology of the Fermi surface.[17, 18] On the other hand, systems far from a QCP can still be tuned but now chemical pressure is required, resulting in high levels of chemical dopants, introducing a high degree of disorder[2]. Given the high degree of disorder, theoretical efforts have focused on disorder related effects in these systems, such as a distribution of Kondo shielding temperatures and manifestations of a Griffith phase[19] where rare ordered subvolumes of the sample have a disproportionate influence on the overall response. A perusal of the literature on quantum critical systems leads one to believe that heavily-doped systems do not shed light on the true nature of quantum phase transitions in (non-disordered) stoichiometric systems.

From Eq. 1.4 we can see that changes to J affect the temperature at which a moment will become shielded and therefore, a distribution of interatomic separations due to chemical doping necessarily leads to a distribution of Kondo shielding tem-

peratures. This causes a network of isolated clusters to form (a percolation network emerges): upon cooling such a doped system, at a given temperature T some moments have become Kondo shielded while others still survive. This is illustrated in Fig. 1.2. The shielded moments are shown in grey (the orientation is shown to be random as the magnetic moments are Kondo shielded), while we can see groups of moments that are not shielded shown in red. Thus, a percolation network has emerged in the material in which isolated clusters of un-shielded moments form.

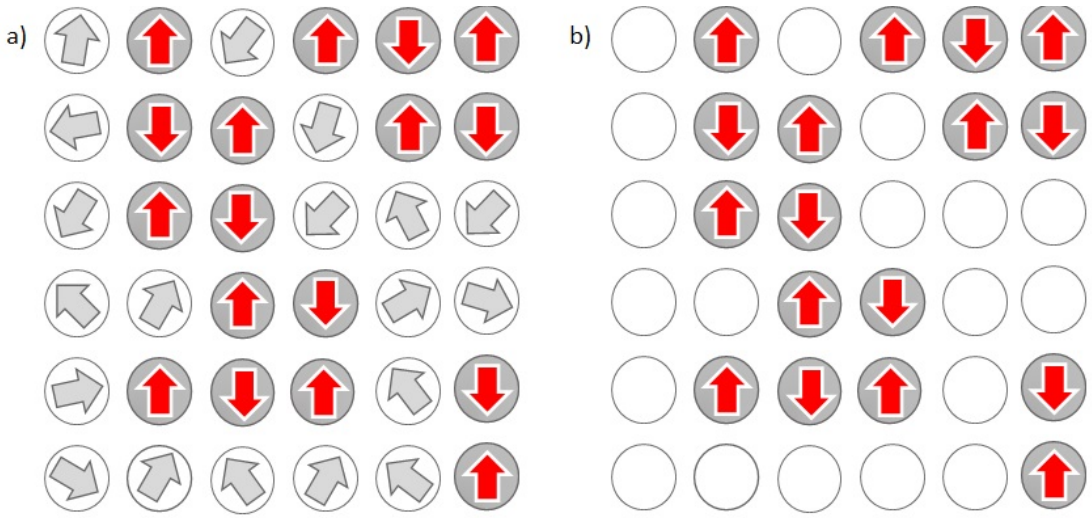

Figure 1.2: Schematic of magnetic moments arranged in a crystalline lattice. Left Panel a): Kondo shielded moments are shown in grey, while groups of isolated unshielded moments are shown in red. Right Panel b): Finite size effects (see text) force the moments in a cluster to align with their neighbors. Counting the number of moments on individual clusters reveals a net uncompensated moment.

From Fig. 1.2, we see that once a group of isolated moments have formed (in red), the moments inside that cluster order with their respective cluster members due to finite size effects. At a given temperature T, thermal fluctuations will attempt to destroy this ordering inside an isolated cluster, however, this type of disordering fluctuation simply costs too much energy to occur due to quantum mechanical finite size effects. Finite size effects occur because the wavelength of any disordering fluctuation

must be proportional to the size of the cluster it is disordering. Thus, for clusters with a small size the energy required to produce a disordering fluctuation is quite large (as energy and wavelength are inversely related, a short wavelength fluctuation requires a large energetic cost). Thus we can calculate an ordering temperature T for a given cluster of radius R (Fig. 1.3)[34]. Assuming an antiferromagnetic system as an illustration; for a cluster of radius $R = 16$ Å, the ordering temperature is $\simeq 45$ K and thus at temperatures below $\simeq 45$ K, any clusters of size 16 Å and smaller must order due to finite size effects. Once a group of moments forms and orders (due to finite size effects), the cluster is protected from further Kondo shielding (spin-flips are necessary for Kondo shielding and are severely impeded in an ordered environment) and thus, once these isolated clusters form and order, they survive down to the lowest possible temperatures.

This restriction on Kondo shielding manifests in the fact that only moments from the lattice spanning cluster (the infinite (largest) cluster that spans from one side of the crystal lattice to the other) may become Kondo shielded at low temperatures. The infinite cluster has an infinite radius. With an infinite radius, any disordering fluctuation (with any wavelength, large or small) would have no problem fitting inside the bounds of the infinite cluster and thus, the moments on the infinite cluster never order but are constantly fluctuating. It is for this reason that moments on the infinite cluster can still become Kondo shielded. Thus upon cooling, when moments from the infinite cluster will become shielded, groups of moments can peel away from the lattice spanning cluster and order due to finite size effects (forming groups of isolated order clusters shown in red in Fig. 1.2). The point at which the infinite cluster breaks apart

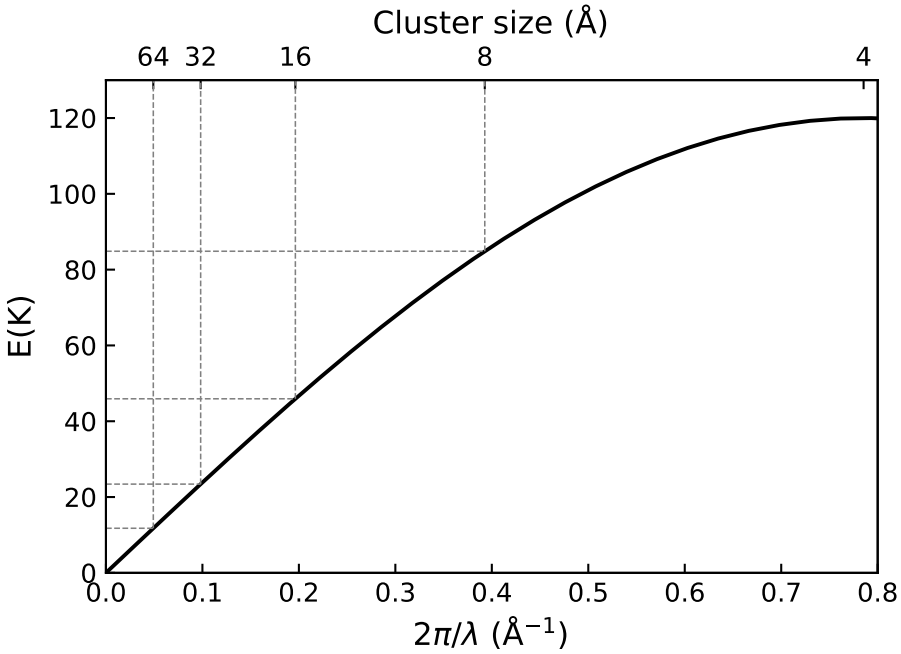

Figure 1.3: Magnon dispersion curve for an antiferromagnetic system in which the minimum excitation energy for a magnon in a cluster of radius R is calculated using finite size effects. The ordering temperatures for several clusters (of size shown above the figure) are displayed using dotted lines. In this example, below $T = 20$ K clusters with a radius of size 32 Å and smaller will order magnetically. This figure was adapted from [34].

is known as the percolation threshold. This particular type of percolation is referred to as protected percolation and falls into its own universality class [33, 55–57]. We see from Fig. 1.4 that in the high J region where Kondo shielding dominates, most of the infinite cluster has become shielded and thus only short range order exists (small isolated clusters shown in blue). For low J when the RKKY interaction dominates and long range order is reached, we see not only the infinite cluster (shown in red) but also groups of isolated clusters which have formed and ordered (shown in blue).

Depending on the size and shape of the these ordered clusters, a single cluster can have a (large) number of uncompensated moments and therefore, the net moment of the cluster will be nonzero. Such a net moment is known as the super spin of that cluster. Effectively, these clusters behave like ferromagnetic impurities. As

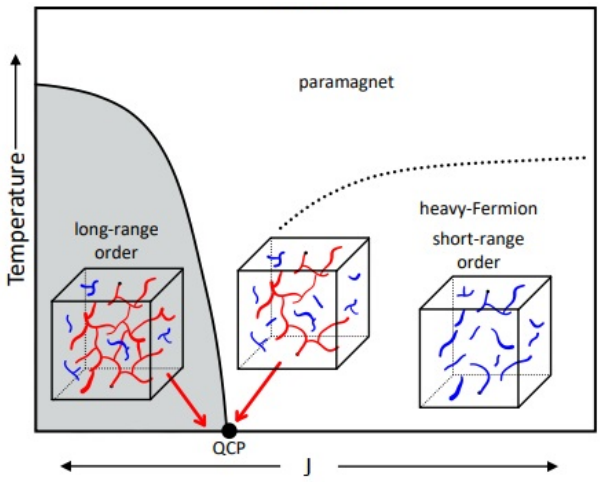

Figure 1.4: The phase diagram for a quantum critical system under the effects of cluster formation caused by changes in interatomic separations via chemical disorder or pressure viewed from a cluster perspective. The size of ordered clusters are shown for each phase. Upon cooling, a magnetically ordered long-range phase (shaded in grey) can be reached. We see the largest cluster shown in red spans the entire lattice i.e., connects two opposite sides (for example the top and bottom). We can apply pressure or magnetic fields in order to drive this transition temperature down to 0 K; the quantum critical point (shown as black dot QCP). The introduction of chemical doping introduces changes in interatomic separations which induces a distribution of Kondo shielding temperatures. Upon cooling, some moments will become shielded before others and a percolation network will form. These clusters are subject to finite size effects and therefore must order, protecting them from further Kondo shielding (spin-flips are necessary for Kondo shielding and are severely impeded in an ordered environment, the ordered clusters). The temperature at which such isolated clusters form and order is given by the dashed line. Below this line, only small isolated clusters exists (shown in blue), and they lead to the appearance of short-range order. We see that at the quantum critical composition upon cooling, the average cluster size increases until at the quantum critical point where the lattice spanning cluster survives all the way down to 0 K. At this point, the infinite cluster is about to order magnetically which would result in long range order. This figure is adapted from [33].

an illustration of this super spin effect, the number of uncompensated moments are circled in blue in the largest ordered cluster that we showed in Fig. 1.2 (and now shown in Fig. 1.5) revealing the super spin associated with this cluster of two uncompensated moments. This super spin can align with external magnetic fields and it contributes to the system's magnetic susceptibility. The ordered environment of these isolated clusters gives us two more experimental predictions. First, because Kondo shielding

of moments is random, we should expect equal number of moments to be correlated along different directions in the material independent of the interaction strength J along that direction and second, we should see the entropy loss associated with the formation of ordered clusters in the specific heat of the material.

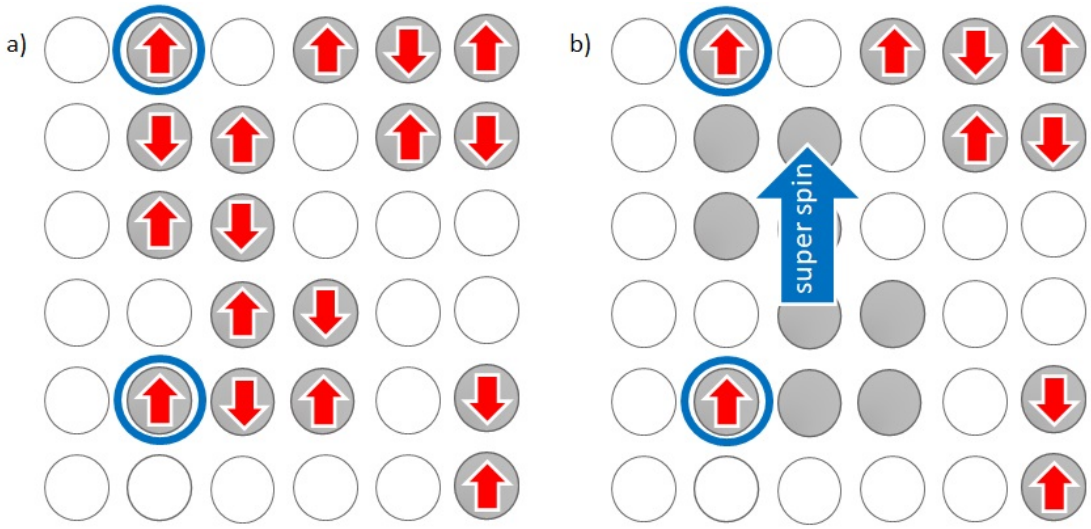

Figure 1.5: Schematic of magnetic moments arranged in a crystalline lattice. Left Panel a): Groups of isolated moments, clusters, are shown in red and the uncompensated moments of the largest isolated cluster are circled in blue. Right Panel b): The same clusters are shown in red but the compensated moments have been removed from the largest isolated cluster and the super spin of that cluster is shown.

In summary, doping leads to a distribution of interatomic separations. This distribution of interatomic separations affects the orbital overlap between neighboring atoms. The changes in orbital overlap greatly affect the strength of the exchange interaction J and ultimately the temperature at which moments will become Kondo shielded. Thus, doping leads to a distribution of Kondo shielding temperatures. Upon cooling, some moments will become shielded before others and a percolation network emerges. Once a group of moments peels away from the lattice spanning cluster, that group of moments must order due to finite size effects and we are left with groups of ordered magnetic clusters. We will show how these ordered clusters can be seen in

the system's susceptibility, specific heat, and in the number of moments correlated along a crystallographic direction (in the next section Section 1.5).

1.5 Cluster Formation in $Ce(Fe_{0.755}Ru_{0.245})_2Ge_2$

We will use the doped compound $Ce(Fe_{0.755}Ru_{0.245})_2Ge_2$ as a reference to understand cluster formation in a quantum critical system with a static distribution of interatomic separations. The published results on this compound that we discuss below formed the inspiration for this thesis. In Chapter 2 and 3 we will apply the same reasoning to stoichiometric compounds, a new avenue. We show that the static distribution of interatomic separations present in $Ce(Fe_{0.755}Ru_{0.245})_2Ge_2$ is created by the random doping of ruthenium, creating local lattice distortions, pushing some cerium atoms closer, while pushing others further apart. This static distribution of interatomic separations induces a distribution of Kondo shielding temperatures. Upon cooling, this leads to fragmentation of the magnetic lattice and to cluster formation. We show that these magnetic clusters dominate the low temperature response of $Ce(Fe_{0.755}Ru_{0.245})_2Ge_2$. For heavily-doped systems, the distribution of atomic separations is (mostly) static. Randomly substituting smaller or larger ions locally leads to lattice shrinking and expansion, necessarily leading to a permanent distribution of inter-ionic separations. Of course, time-dependent changes are also present in heavily-doped systems. For simplicity, we treat the distribution of Kondo temperatures in heavily-doped systems as if they were entirely static, we return to dynamic, zero-point motion induced distributions when we discuss stoichiometric systems (Chapter 2-3).

1.5.1 Non-Fermi Liquid, Structure, and Phase Diagram

$Ce(Fe_{0.755}Ru_{0.245})_2Ge_2$ is a heavy-fermion compound where expansion of the tetragonal lattice from the stoichiometric $CeFe_2Ge_2$ by a substitution of one in four iron atoms for ruthenium atoms drives the system to the quantum critical point where it experiences both short and long range fluctuations. $Ce(Fe_{0.755}Ru_{0.245})_2Ge_2$ crystallizes in the $ThCr_2Si_2$ structure[25] or 122-structure (panel a) of Fig. 1.6) and it displays a strong Ising character in which the easy axis for the moment of the Ce-ions is along the c-axis[36]. Iron and ruthenium do not carry a local moment in this compound, therefore from a magnetic point of view, the Ce-Ions form a body centered tetragonal lattice with the length of the c-axis being approximately 2.5 times the length of the a-axes[35]. The random doping of one in four iron atoms for ruthenium creates local lattice distortions around each doping site, pushing some atoms closer together while forcing others further apart as illustrated in panel b) of Fig. 1.6. Thus, the doping of ruthenium naturally leads to a distribution of Kondo shielding temperatures. Elastic neutron scattering experiments[33] on $Ce(Fe_{0.755}Ru_{0.245})_2Ge_2$ demonstrated that it is on the verge of ordering magnetically. The ordering wave vector was found to be $(0, 0, 0.45)$ implying a spin density wave (SDW) instability and confirming that the RKKY interaction is indeed responsible for any long range order observed. Therefore, $Ce(Fe_{0.755}Ru_{0.245})_2Ge_2$ appears to be in the paramagnetic phase just shy of long range ordering and thus, extremely close to its quantum critical point and an ideal candidate to understand cluster formation.

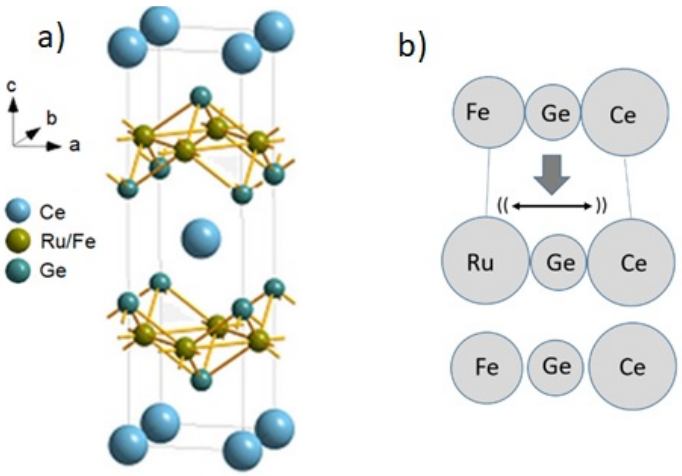

Figure 1.6: Left Panel a): $ThCr_2Si_2$ crystal structure, reproduced from Sven *et al.*[15]. Right Panel b): Schematic showing the lattice distortions associated with the chemical doping of ruthenium for iron atoms in $Ce(Fe_{0.755}Ru_{0.245})_2Ge_2$.

1.5.2 Evidence of Static Cluster Formation

Montfrooij *et al.*[33] discovered through neutron scattering experiments the presence of magnetic clusters in $Ce(Fe_{0.755}Ru_{0.245})_2Ge_2$: upon cooling the system, identical number of magnetic moments were observed to be correlated along distinct crystallographic directions. This is reproduced in Fig. 1.7. The horizontal axis in Fig. 1.7 is in reciprocal lattice units and therefore, the inverse of the width is directly proportional to how many moments are correlated along that particular direction in the crystal. We see that for all temperatures, the curves for all directions fall directly on top of one another, meaning that there are identical numbers of moments lined up along the c-direction (red) as there are along another distinct (in plane) direction (black). We know the RKKY interaction is responsible for long range order in $Ce(Fe_{0.755}Ru_{0.245})_2Ge_2$ and depends on the distance r between moments. In the tetragonal lattice the strength of the exchange interaction J varies along different crystallographic directions as well. Thus, we would expect to see the number of mo-

ments aligned along the c-direction to be vastly different than along the a-direction because of to the tetragonal lattice ($c/a = 2.5$). As this is not the case, we are not dealing with incipient long-range range order due to the RKKY interaction and therefore, the most likely culprit for this magnetic intensity are groups of ordered clusters which formed upon cooling. After all, the only situation in which the strength of the ordering interaction no longer plays a role is when all moments have ordered. This is clear indication of the presence of ordered clusters in the sample as was detailed in reference [33].

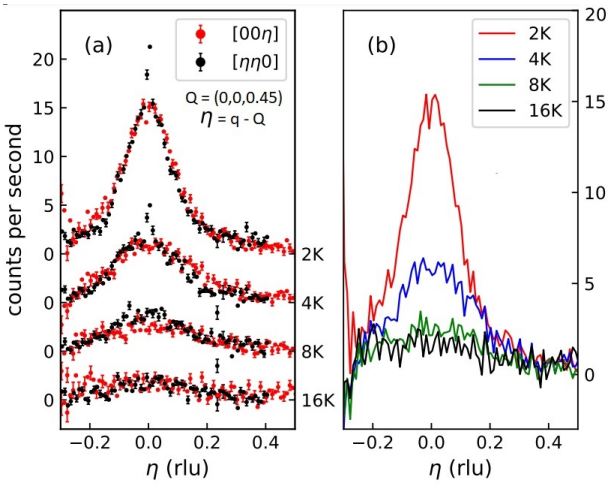

Figure 1.7: Figure reproduced from [33]. Left Panel (a): The temperature dependence of the magnetic scattering in $Ce(Fe_{0.755}Ru_{0.245})_2Ge_2$, measured by means of neutron scattering. The peaks observed were associated to cluster formation by Montfrooij *et al.*[33]. Upon cooling, we observe that the magnetic scattering begins to emerge around 16K and increases in intensity while also narrowing in width in q-space. The inverse of this width is directly proportional to how many moments are correlated and thus, we see that there are identical number of moments ordered along the c-direction (red symbols) as there are along another distinct high symmetry direction (black symbols). This holds for all temperatures observed. In $Ce(Fe_{0.755}Ru_{0.245})_2Ge_2$, the lengths of the c and a axes differ by 2.5, and thus, this is clear indication that we are dealing with ordered magnetic moments. These clusters have formed via random Kondo shielding of moments. The curves have been offset along the vertical axis. Right Panel (b): Displays the same data, but now plotted on top of each other, the curves are not offset. We observe that once clusters form and order, that these clusters remain intact upon cooling. Upon cooling further, we observe that new (and larger, as observed by the narrowing width) clusters form, and that the scattering from these clusters augments the scattering of any clusters already present. Thus, isolated clusters are protected from further Kondo shielding upon forming and subsequently ordering.

In protected percolation, once clusters form, they must order due to finite size effects and are protected from further Kondo shielding [33]. Upon cooling, these clusters cannot be further shielded and keep contributing to the magnetic scattering. Therefore we should see increased magnetic scattering appear on top of or in addition to already existing magnetic scattering upon cooling. Looking at Fig. 1.7, we see that upon cooling, new (and larger, as implied by the narrowing width) clusters form and order. This scattering augments the scattering of the clusters already present. This is clear indication that isolated magnetic clusters are protected from any further Kondo shielding once they have formed (and ordered due to finite size effects).

When clusters form and order in $Ce(Fe_{0.755}Ru_{0.245})_2Ge_2$, they shed their entropy. This can be seen in the specific heat of the sample. When a single moment "peels away" from the lattice spanning cluster in an Ising system, a total of $k_B \ln 2$ in entropy is shed. If a cluster of n moments peels away from the lattice spanning cluster, the cluster moments must order and a total of $(n-1)k_b \ln 2$ in entropy is shed. The loss of entropy is proportional to $n-1$ because the cluster still has a single degree of freedom remaining related to the super spin of the cluster[46]. As we approach the point at which the lattice spanning cluster breaks apart closer and closer, the clusters which peel away become larger and larger. Effectively the entropy of the system is locked into the lattice spanning cluster as the super spins do not shed their entropy in the absence of an applied field. Gaddy *et al.*[42] calculated the entropy of $Ce(Fe_{0.755}Ru_{0.245})_2Ge_2$ through numerical integration of the specific heat and then performed protected percolation simulations as a function of occupancy p and used this entropy-lattice spanning cluster correspondence to determine the occupancy as

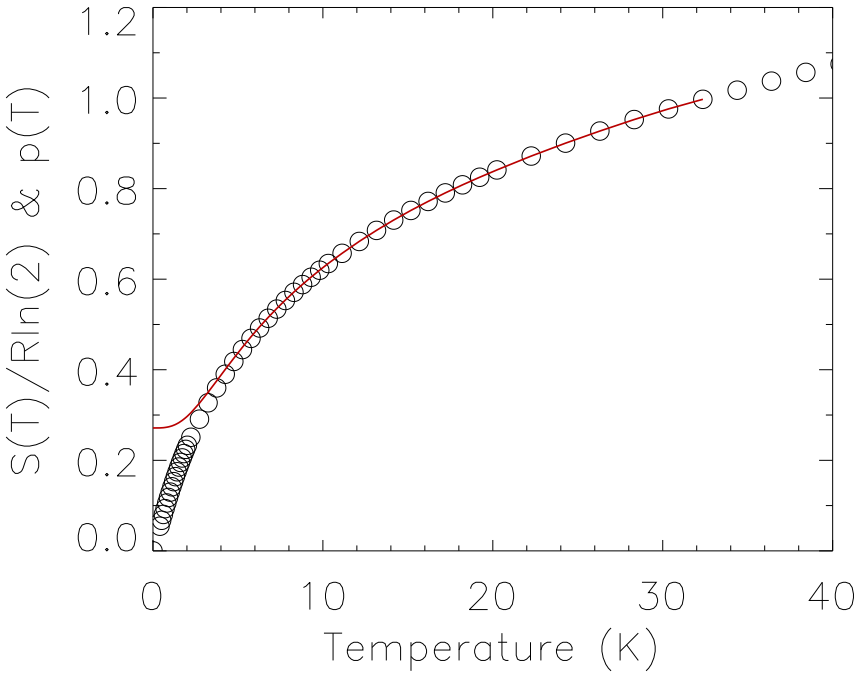

Figure 1.8: The entropy of $Ce(Fe_{0.755}Ru_{0.245})_2Ge_2$ (circles) determined through numeral integration of specific heat data. By equating entropy to the occupancy, we can plot the occupancy as a function of temperature $p(T)$. We note here that while the occupancy changes relatively little at low temperatures, the system is on the verge of a phase transition and therefore even small changes in occupancy give rise to large changes in the strength of the lattice spanning cluster as larger and larger clusters break away from the lattice spanning cluster.

a function of temperature. We show this in Fig. 1.8.

The ordered clusters that have formed in $Ce(Fe_{0.755}Ru_{0.245})_2Ge_2$ also have a super spin associated with them. This super spin can align with external magnetic fields and can be seen in the system's susceptibility. Interestingly, we can completely bypass any in-between computer simulations and relate the measured specific heat to the observed uniform susceptibility using the above entropy-lattice spanning cluster correspondence. Assuming moments in $Ce(Fe_{0.755}Ru_{0.245})_2Ge_2$ follow protected percolation, then $k_B$ln2 is lost in entropy every time a single Ce-moment becomes shielded from the lattice spanning cluster. Thus, we can make the assumption that the susceptibility of the infinite cluster, χ_∞, while undergoing Kondo shielding of its

moments, can be written as

$$\chi_\infty = \frac{S(T)}{\mathrm{Rln2}}\chi_{free}(T). \tag{1.5}$$

where $S(T)$ is the entropy of the system calculated by numerical integration of the specific heat $c(T)/T$, R is the gas constant, and χ_{free} is the known susceptibility of an individual cerium ion placed in the local tetragonal crystal electric field (CEF) of $Ce(Fe_{0.755}Ru_{0.245})_2Ge_2$. Thus, $S(T)S$ is the number of remaining Rln2 unshielded moments on the infinite cluster. From experiments on $CeRu_2Si_2$, it is known[35] that the three ground state doublets are split by 33 and 55 meV, and therefore barely influence the specific heat below 100 K. However, we do not know the CEF levels for $Ce(Fe_{0.755}Ru_{0.245})_2Ge_2$. Considering both systems' similarity, in order to model χ_{free}[38] we assume the CEF levels in $Ce(Fe_{0.755}Ru_{0.245})_2Ge_2$ to be similar to those seen in $CeRu_2Si_2$. We chose a value of the moment of the individual free cerium ion to be of 1.43 μ_B per Ce-ion; this value was found to yield the best agreement between entropy and susceptibility. Note that, based on the admixture of the $|J_z = 5/2\rangle$ and $|J_z = 3/2\rangle$ states, we could have expected a free moment of around 1.85 μ_B (using g_J =6/7), fairly close to the value obtained from the fit.

As seen in Fig. 1.9, the agreement proposed in Eq. 1.5 is nearly perfect from 10 K to 120 K (with 120 K being the upper bound of the measured specific heat data). Of special note is the underestimation of the predicted susceptibility (solid curve) seen around 10 K. This is around the same temperature at which neutron scattering data (Fig. 1.7)[38] suggests isolated clusters begin to emerge. The super spin of isolated clusters can align with an external magnetic field and thereby contribute to the susceptibility measurements. Therefore, as isolated clusters emerge, Eq. 1.5 should

indeed underestimate χ_∞ as it leaves out the super spin contribution. In conclusion, Eq. 1.5 appears to correctly describe the susceptibility of the disordered moments and is useful as a diagnostic tool when looking for the appearance of magnetic clusters that form from a static distribution of Kondo shielding temperatures.

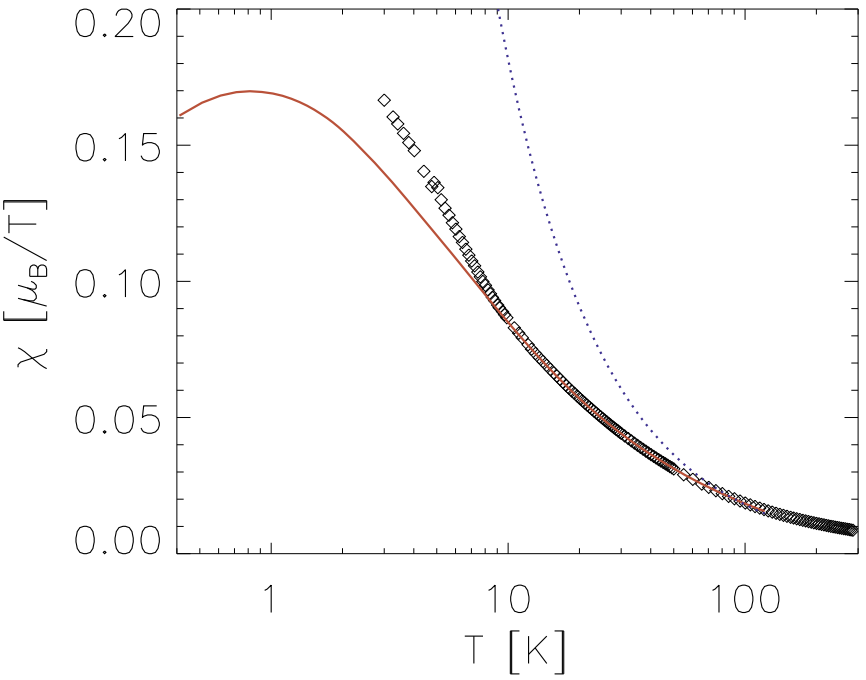

Figure 1.9: The uniform susceptibility for $Ce(Fe_{0.755}Ru_{0.245})_2Ge_2$ (diamonds) measured[33] for a field of 0.2 T parallel to the crystallographic c-axis in this (almost) Ising system. The dotted curve follows the Curie Weiss law at high temperatures which has only a very limited range of validity. The solid curve (Eq. 1.5) is the measured entropy of the sample, divided by $R\ln 2$ and multiplied by the temperature dependence of the magnetic response of a three level doublet system with energy gaps of 33 and 55 meV[35], with the ground state magnetic moment taken to be $1.43\mu_B$ (and the two excited state moments reduced by a similar factor, although the excited states do not play a factor in this visual comparison). The measured susceptibility and the specific heat based prediction start to deviate below $T < 10$ K where clusters first appear in the neutron scattering spectra.

Im summary, we have discussed here a distribution of interatomic separations creates a distribution of shielding temperatures. Upon cooling, some moments will become shielded before others, leading to fragmentation of the magnetic lattice into

groups of ordered moments. These ordered magnetic clusters dominate the low temperature response seen in $Ce(Fe_{0.755}Ru_{0.245})_2Ge_2$ [33, 38]. Next we address the mechanism through which clusters can form in a stoichiometric system and we show that not only are magnetic clusters present in such systems, they also dominate the low-temperature response near the QCP.

Chapter 2

Cluster Formation in Stoichiometric $CeRu_2Si_2$

2.1 Introduction

When describing stoichiometric systems that are (very) close to a quantum critical point, such as $CeRu_2Si_2$[26], $CeCu_6$[70], and $YbRh_2Si_2$[63], disorder is not taken into account. Instead, the experimental observations are compared to the theoretical predictions, such as the spin density wave scenario,[18, 24] local moment scenario,[8, 16] or the self-consistent spin renormalization (SCR) model.[24] We will not detail the various scenarios here; none of the scenarios describe all quantum critical systems, but each scenario appears to capture the essence of particular systems quite well. As mentioned, these theories tend to be applied solely to (near) stoichiometric systems while the response of heavily-doped systems is viewed as being disorder driven. We show that this is not the case: we show that the effects of a static distribution of Kondo shielding temperatures induced by chemical doping are very similar to the effects of a dynamic distribution of Kondo temperatures originating from zero point motion. We have chosen stoichiometric $CeRu_2Si_2$ as the reference system for understanding cluster formation in a disorder free system as this compound has been investigated

by many groups.[22, 26–29] In particular, we use the data gathered by Tabata[22] on susceptibility and specific heat measurements, and the neutron scattering data on single crystal samples by Kadowaki *et al.*[27, 28].

Stoichiometric $CeRu_2Si_2$ and heavily doped $Ce(Fe_{0.755}Ru_{0.245})_2Ge_2$ show quite a lot of similarities: both systems crystallize in the $ThCr_2Si_2$ structure (Fig. 1.6)[25] and neutron scattering experiments[27, 29] on both systems demonstrated a strong Ising character, i.e., the ordered moments point along the tetragonal c-axis. The crystal electric fields split the J_Z-energy levels into three doublets[35] with the first excited state in $CeRu_2Si_2$ being well separated from the lowest level ($\Delta > 30$ meV). The ground state of both systems displays mostly a $|J_Z = 5/2\rangle$ character[35]. Flouquet *et al.*[29] showed $CeRu_2Si_2$ to be on the cusp of a spin density wave (SDW) transition. This was confirmed by Kadowaki *et al.*[27] using inelastic neutron scattering experiments on two large single crystals, one of $CeRu_2Si_2$ and subsequently, on a lightly doped crystal of $CeRu_{1.94}Rh_{0.06}Si_2$ [28]. Montfrooij *et al.*[33] also observed the tell-tale SDW incommensurate ordering wavevectors (short-range correlations) in $Ce(Fe_{0.755}Ru_{0.245})_2Ge_2$. Ultimately, both $Ce(Fe_{0.755}Ru_{0.245})_2Ge_2$ and $CeRu_{1.94}Rh_{0.06}Si_2$ appear to be in the paramagnetic phase just shy of long range ordering. Long range order has been observed[33, 37] in both systems when chemically doped a little bit more into the SDW-range. Therefore, we conclude that $CeRu_{1.94}Rh_{0.06}Si_2$ and $Ce(Fe_{0.755}Ru_{0.245})_2Ge_2$ are at nearly identical points in their Doniach[39] phase diagrams.

As we are dealing with ordering in both compounds that was unambiguously identified as a spin density wave[28, 33], we know the ordering interaction must be the

RKKY interaction discussed in Chapter 1. This interaction is oscillatory in nature and depends on the separation between magnetic ions as $\sim 1/r^4$ (Appendix A). Again, similar to $Ce(Fe_{0.755}Ru_{0.245})_2Ge_2$, $CeRu_2Si_2$ is tetragonal with Ce-Ce distances distances along the c-axis larger than along the in plane directions. In detail, d_{Ce-Ce} (distance from Cerium to Cerium atom) along the a-axis is 4.08 Å in $Ce(Fe_{0.755}Ru_{0.245})_2Ge_2$ while it is 4.20 Å in $CeRu_2Si_2$; along the body diagonal (c-axis) we have $d_{Ce-Ce} = 5.97$ Å in $Ce(Fe_{0.755}Ru_{0.245})_2Ge_2$ and 5.73 Å in $CeRu_2Si_2$. Thus, in the absence of clusters we would expect to find different number of moments correlated along different crystallographic directions reflecting the difference in interaction strength along each direction. In contrast, if clusters were to be present in stoichiometric $CeRu_2Si_2$, then we would expect to see identical number of magnetic moments correlated along different directions. Ultimately, considering the similarities between $Ce(Fe_{0.755}Ru_{0.245})_2Ge_2$ and $CeRu_2Si_2$, the latter is the ideal stoichiometric compound to look for cluster formation resulting from a distribution of shielding temperatures.

2.2 Zero Point Motion and Cluster Formation

In a disorder-free stoichiometric system, what could cause a distribution of interatomic separations and, upon cooling, lead to magnetic cluster formation? At low temperatures (even at 0 K) atoms are still jiggling back and forth in a process known as zero point motion. This back and forth motion is equivalent to vibrations that travel through the system known as phonons. These phonons produce changes in interatomic separations; the amplitude of such changes can be assessed in neutron scattering experiments and is found to be on the order of 0.05 Å[25], extremely simi-

lar to that of chemical doping. These distributions in interatomic separations affect the orbital overlap, thereby changing the strength of the exchange interaction J, and driving the system towards an ordered or disordered phase or even towards quantum criticality. Upon cooling, this leads some moments to become shielded before others and a percolation network emerges. The introduction of finite size effects leads to groups of ordered, isolated clusters to form. Thus, a distribution of ordered clusters will indeed form, albeit a time-varying distribution, following the dynamic distribution of interatomic separations.

Whether the dynamic distribution of Kondo temperatures will actually be reflected in experimentally accessible quantities is a matter of timescales. Should the electronic timescale associated with Kondo shielding of moments be fast enough that it appears to the electrons as if this ever-changing distribution were static, then we could see the effects of the distribution in the experiments. This is none other than the adiabatic approximation in phonon theory. On the other hand, if the electronic timescales are comparable to those associated with zero point motion, or if (the timescales of) the experiments are such that the probes only measure time-averaged values, then we would not see a reflection of this instantaneous disorder. Since ionic motion is significantly slower than electronic motion, to moving electrons as well as to neutrons, this dynamic distribution of clusters will appear as a static distribution. Therefore, despite the fact that this distribution of shielding temperatures is dynamic, it should (upon cooling) create a measurable percolation network and associated distribution of magnetic clusters. These ordered clusters should, provided they are present, dominate the low temperature response of $CeRu_2Si_2$ similar to the low temperature response

of the heavily doped $Ce(Fe_{0.755}Ru_{0.245})_2Ge_2$ (Section 1.5).

2.2.1 Distribution of Shielding Temperatures $P(T_K)$

In order to understand cluster formation in stoichiometric $CeRu_2Si_2$, we must first begin to understand what a dynamic distribution of Kondo shielding temperatures induced by zero-point motion looks like. To do so, we have modified the distribution of Kondo temperatures used by Bernal *et al.* to describe the non-Fermi liquid behavior seen in $UCu_{3.5}Pd_{1.5}$ and UCu_4Pd. This distribution is known as the Kondo disorder model[20, 21] in which the response of a heavily-doped quantum critical system is described as the response of a collection of non-interacting magnetic ions that are being Kondo shielded at different temperatures. The advantage of this model is that, given a distribution of Kondo shielding temperatures $P(T_K)$, the known expressions[22] for susceptibility and specific heat for dilute magnetic moments can be applied and weighed with the overall distribution in order to arrive at the response of the doped system at any temperature. The parameters of the distribution can then be fine-tuned (fitted) to arrive at the best overall agreement with the experimental results for susceptibility and specific heat. Moreover, the idea of there being a distribution of Kondo temperatures in the first place in doped systems has a solid physical foundation as the Kondo temperature depends exponentially on the degree of overlap of neighboring orbitals, which in turn depends on the interatomic separation[23] r as $\sim 1/r^{10}$ or $\sim 1/r^{12}$.

Bernal *et al.*[20] used three free parameters to describe their distribution of Kondo shielding temperatures $P(T_K)$: D the bandwidth of the conduction band, $\langle\lambda\rangle = \rho|J|$, and the width w of the Gaussian. This allowed the authors to model the

susceptibility and specific heat simultaneously by using one Gaussian distribution of the exchange interaction J, representing the physical overlap between localized moment-carrying orbitals and extended conduction electron orbitals. Applications to other disordered systems also showed that disorder plays a role, although it was not always possible to model both the susceptibility and specific heat with one set of parameters (such as when modeling[22] heavily-doped $CeRuRhSi_2$). While this particular disorder model does capture some of the experimental observations, we note that the model is unphysical: the assumption of a Gaussian in λ introduces an $\ln(T_K)$ divergence. We introduce an improvement on this distribution of shielding temperatures, $P(T_K)$, that is free from this artifact and that is based upon the average deviations of ions from their equilibrium lattice positions, the so-called Debye-Waller factor. This factor can be directly measured using neutron scattering experiments[32] and therefore reduces the number of "free" parameters in the distribution of Kondo shielding temperatures. To create such a distribution, we will use the method outlined by Endstra et al.[23].

The effective exchange interaction J between a d-electron and an f-electron in a metal can be written as

$$J_{df} \propto V_{df}^2/(E_f - \epsilon_f) \propto 1/r^{12} \tag{2.1}$$

where V_{df} is the hybridization matrix element for $d-f$ electron hybridization, ϵ_f is the location of the f level relative to the Fermi energy E_f and r is the average separation between neighboring ions. Endstra et al.[23] reasoned that the variation in $E_f - \epsilon_f$ could be ignored, resulting in a $1/r^{12}$ dependence for J. Thus the Kondo

temperature (Eq. 1.4) can now be written as

$$T_K = De^{-r^{12}/A}, \tag{2.2}$$

where A is the constant of proportionality encapsulating ρ (Eq. 1.4).

We build a distribution of shielding temperatures $P(T_K)$ by assuming a Gaussian distribution of interatomic separations r given by

$$P(r) = \frac{\sqrt{\ln 2}}{\sqrt{\pi}\sigma} e^{-(r-r_c)^2/\sigma^2 \ln 2}, \tag{2.3}$$

where σ is the width of the Gaussian and r_c is the average center-to-center distance of two ions. The distribution $P(r)$ is rooted in neutron scattering experiments and amounts to neglecting anharmonic contributions to the motion of ions around their equilibrium position[30]. This distribution naturally describes how zero-point motion can induce a distribution of shielding temperatures by atoms oscillating back and forth about a central position. Building a distribution of shielding temperatures $P(T_K)$ based upon a Gaussian distribution in $P(r)$ removes the $\ln(T_K)$ divergence seen Bernal's approach[20] that comes from assuming a Gaussian distribution in λ. Using conservation of probability, we relate the distribution $P(T_K)$ to the distribution of interatomic separations $P(r)$ as

$$P(T_K) = |\frac{\mathrm{d}r}{\mathrm{d}T_K}|P(r) = [\frac{A}{12r^{11}T_K}]P(r). \tag{2.4}$$

We note that we can then relate the parameters to those of the Bernal distribution by equating the mean Kondo temperature and the width of the distribution yielding

$$A = \langle\lambda\rangle r_c^{12}; \quad \frac{\sigma}{r_c} = \frac{w}{12\langle\lambda\rangle}. \tag{2.5}$$

For example, using the distribution parameters published for UCu_4Pd[20] and the measured[31] U-Cu distance of 3.49 Å, we find $\sigma = 0.049$ Å. Using the parameters

listed by Tabata[22] for $CeRuRhSi_2$, we find $\sigma = 0.038$ Å. These are reasonable values for the Debye-Waller factor at low temperatures: for instance, the measured[32] isotropic Debye-Waller factors for Ce and Ru in $CeRu_2Si_2$ are 0.039 Å and 0.058 Å, respectively (although reported[32] with large uncertainties). Note that since the Debye-Waller factor is experimentally accessible, this reduces the number of adjustable parameters in the distribution of Kondo shielding temperatures from three to two.

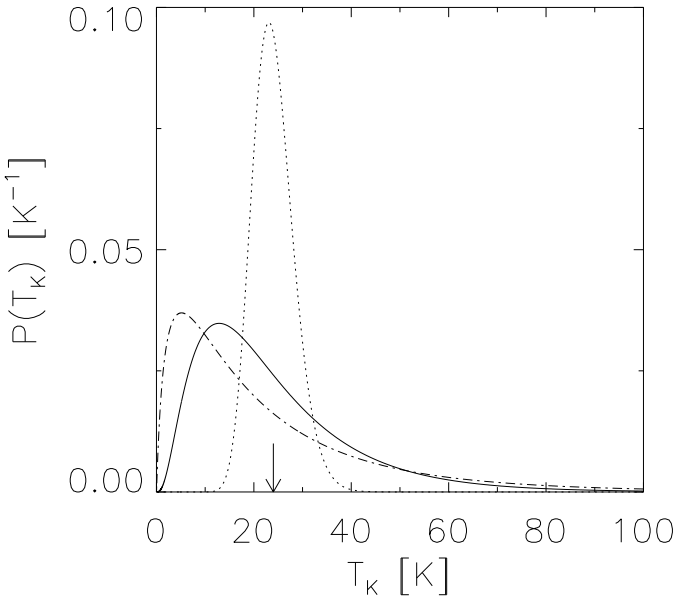

Figure 2.1: The distribution of Kondo temperatures according to Eq. 2.4 for three values of σ: $\sigma = 0.001$ Å (dotted curve), $\sigma = 0.039$ Å (solid curve), $\sigma = 0.058$ Å (dash-dotted curve). All the distributions have the same average Kondo temperature $< T_K >= 24$ K (arrow). Note the absence of the $\ln(T_K)$ divergence as $T_K \to 0$ K.

Fig. 2.1 shows the distribution of Kondo temperatures, $P(T_K)$ according to Eq. 2.4 for three values of σ (one being the measured Debye-Waller factor), the reported value for $\langle\lambda\rangle = 0.18$ for $CeRuRhSi_2$, and the average Kondo $\langle T_K\rangle = 24$ K for $CeRu_2Si_2$. Whereas this value for $\langle\lambda\rangle$ will not be exactly correct for stoichiometric $CeRu_2Si_2$, the figure offers a good indication of what an instantaneous distribution of Kondo

temperatures looks like in a disorder-free system. As can be seen in this figure, for realistic values for the amplitude of zero point motion of the order of $\sim$ 0.05 Å, the instantaneous distribution of Kondo temperatures is very wide. It is only for unphysical values of $\sigma \sim 0.001$ Å, as opposed to the two realistic values shown in the figure, that the distribution is sharp at $T =< T_K >$. What is clear from this figure is that theoretical approaches describing quantum critical physics in stoichiometric systems wherein the Kondo temperature is treated as a uniform parameter throughout the lattice and throughout time are simply not justified as a starting assumption.

2.2.2 ARPES Measurements

We have taken angle-resolved photoemission spectroscopy (ARPES) measurements on pieces of $Ce(Fe_{0.755}Ru_{0.245})_2Ge_2$ in an attempt to measure the bandwidth of the conduction band D to reduce the number of "free" parameters in the distribution of Kondo shielding temperatures. Cuts from the top and bottom of a large single crystal of $Ce(Fe_{0.755}Ru_{0.245})_2Ge_2$ were used (Fig. 2.2 (a)); the bottom piece was untreated, while the top was remelted and allowed to cool and recrystallize in order to prepare a uniformly flat surface. Both top and bottom pieces produced results which were inconclusive and showed extensive polycrystalinity as well as roughness of the surface. As such, we did not obtain accurate estimates for the bandwidth D in $Ce(Fe_{0.755}Ru_{0.245})_2Ge_2$. To estimate D more accurately, we therefore looked at the wealth of data published on $CeRu_2Si_2$. Yano *et al.*[64] performed just such an ARPES experiment (Fig. 2.2 b)); considering that conduction electrons which participate in Kondo shielding result in a Kondo resonance at the Fermi level, we can identify the Kondo band (b of Fig. 2.2) and estimate D to be ~ 0.6 eV. This estimate is entirely

consistent with estimates from $Ce(Fe_{0.755}Ru_{0.245})_2Ge_2$ and in principle, reduces the number of free parameters in the distribution of Kondo shielding temperatures to just one. Therefore, the distribution function shown in Fig. 2.1 is grounded entirely in experiment.

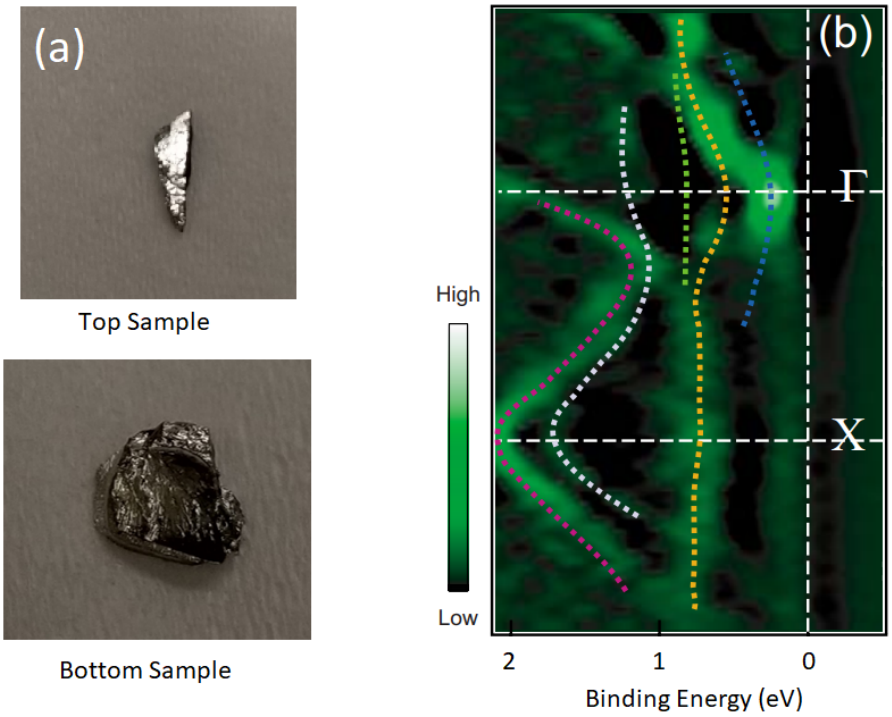

Figure 2.2: Left Panel (a): Top and bottom pieces of $Ce(Fe_{0.755}Ru_{0.245})_2Ge_2$ used for ARPES measurements (data not shown) yielding an estimate for the bandwidth of the conduction band $D \sim 0.5 - 0.8$ eV. Right Panel (b): ARPES spectra of $CeRu_2Si_2$ near E_f at 20 K with $h\nu = 725$ eV. Second order differential image along the $\Gamma - X$ directions. Energy resolutions are set to about 100 meV and the dashed lines representing each band are guides to the eye. The Kondo band is seen in the top right part of this figure, from Γ dispersing downward by about 0.6 eV. Right panel (b) reproduced from [64].

2.3 Dynamic Cluster Formation in $CeRu_2Si_2$

2.3.1 Neutron Scattering

$CeRu_2Si_2$ is an heavily studied system with a host of experimental data published[22, 26–29]; Kadowaki *et al.*[27][28] have performed neutron scattering experiments similar

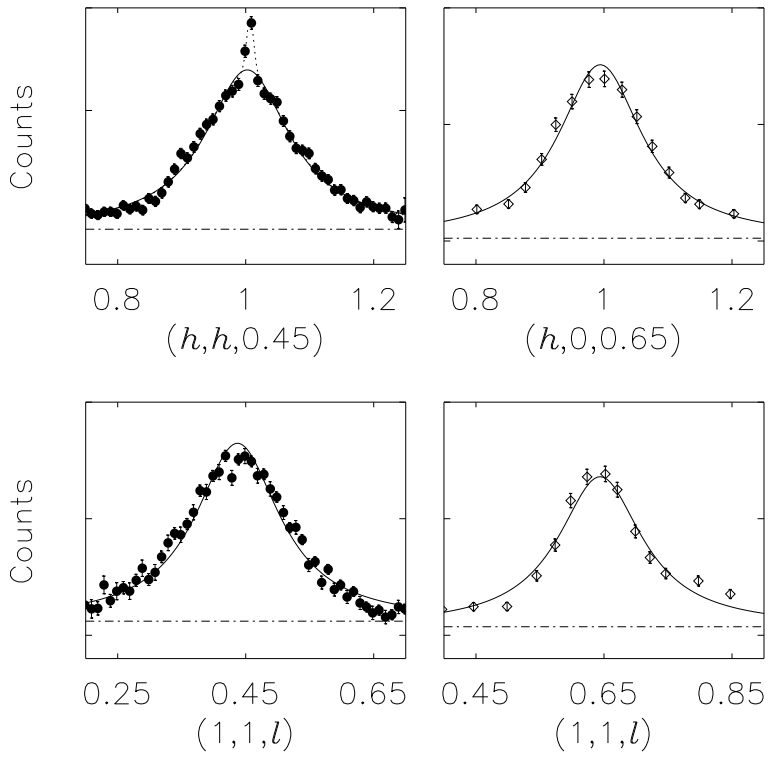

Figure 2.3: Elastic neutron scattering data for $Ce(Fe_{0.755}Ru_{0.245})_2Ge_2$ [33] at $T = 2\,K$ (left two panels) and for $E = 0.2\,meV$ for $CeRu_{1.94}Rh_{0.06}Si_2$ [28] at $T = 1.6\,K$ (right two panels) as a function of momentum transfer along the directions specified on the axes. The solid line through the data is a Lorentzian fit with a width of $0.166/2\,r\ell u$ for all four panels ($r\ell u$ = reciprocal lattice units).

to the ones seen in Fig. 1.7 taken by Montfrooij *et al.*[33], albeit at an energy transfer of $E = 0.2\,meV$ (nearly elastic). We reproduce each group's results in Fig. 2.3. We observe in $CeRu_{1.94}Rh_{0.06}Si_2$ [27, 28] (Fig. 2.3 right panel) that the number of moments aligned along the a- and c-directions is identical. Moreover, the solid curve through all four data sets is a Lorentzian fit with a width of $0.166/2$ $r\ell u$ (reciprocal lattice units) which reasonably describes all four panels. This indicates that we not only have identical numbers of moments correlated along each direction in each compound, but that the cluster distribution in both $CeRu_{1.94}Rh_{0.06}Si_2$ and $Ce(Fe_{0.755}Ru_{0.245})_2Ge_2$

[33] is nearly identical despite one being dynamic and the other one static. We are not aware of any other explanation other than ordered magnetic clusters that could explain short-range order appearing because of an interaction whose strength depends on separation between neighboring magnetic ions, but whose spatial extent does not depend on this intermoment separation.

Identical number of correlated moments along different directions might not in itself be conclusive, but taken with the ratios of $d^{\text{diagonal}}_{Ce-Ce}/d^{a}_{Ce-Ce}$ for the two compounds (1.463 for $Ce(Fe_{0.755}Ru_{0.245})_2Ge_2$ and 1.365 for $CeRu_{1.94}Rh_{0.06}Si_2$), we can rule out an accidental effect intrinsic to the RKKY interaction. Using data taken by Kadowaki *et al.* at higher temperatures (Fig. 1 reference [28]), it appears that the correlation lengths between the a and c-directions continue to be identical at all temperatures (within the accuracy of the experiments). This was also seen by Montfrooij et al.[33] and can be seen in Fig. 1.7.

So far, we have shown that neutron scattering experiments offer strong evidence for the presence of ordered magnetic clusters in (nearly) stoichiometric quantum critical $CeRu_2Si_2$. As discussed in the previous section (Section 2.2), neutron scattering experiments cannot reveal whether these clusters are fleeting or permanent as the speed of the probing neutron is much faster than the speed of ionic motion.

2.3.2 Uniform Susceptibility

We turn to the specific heat and susceptibility of $CeRu_2Si_2$ to investigate how these dynamic clusters may differ from a static distribution. Applying Eq. 1.5 to the uniform susceptibility measured by Tabata et al.[22] on $CeRu_2Si_2$, we only see agreement in the low temperature region (see Fig. 2.4) where the magnetic specific heat curve $c(T)/T$

as well as the uniform susceptibility were found to be T-independent[22, 43, 44] for moderate field values ($H = 0.1$ T) and low temperatures ($1.5\,\mathrm{K} < T < 5\,\mathrm{K}$). The specific heat curve below $T = 5$ K was found to have a constant value of $\gamma = c/T = 0.38$ J/mol/K^2, while the value for the slightly doped $CeRu_{1.94}Rh_{0.06}Si_2$ is higher with a weak temperature dependence[22] ($\gamma = 0.5$ J/mol/K^2 at $T = 0.2$ K). We note that for $CeRu_2Si_2$ the specific heat curve was found to differ by as much as 50% at $T = 10\,\mathrm{K}$ between three independent sources (inset of Fig. 2.4). We choose to use the data measured by Tabata[22] since the sample used is the same sample used in the susceptibility measurements shown in Fig. 2.4.

When c/T reaches a constant value at low temperatures, then the entropy of the system depends on temperature as $S = \gamma T$ and in this region, we approximate the non-interacting Ising susceptibility as $\chi_{free} = (g_J J_{\mathrm{eff}}\mu_B)^2/k_B T$ as $\mu_B \mathrm{H}/k_B T \ll 1$ when $H = 0.1$ T. Eq. 1.5 then reduces to

$$\chi_\infty = \frac{\gamma}{\mathrm{Rln2}} \frac{(g_J J_{\mathrm{eff}}\mu_B)^2}{k_B} = 0.1166\gamma(g_J J_{\mathrm{eff}})^2 \frac{\mu_B}{\mathrm{T.Ce}}. \tag{2.6}$$

where g_J is the Landé g-factor which has a value of 6/7 for Ce^{3+}[30].

Applying Eq. 2.6 to Fig. 2.4 we deduce a low temperature moment value for the Ce-ions (which constitute the lattice spanning cluster) of 1.21 μ_B per Ce-ion. This value appears entirely reasonable when compared to the high-temperature susceptibility (Fig. 2.4) yielding a ground state moment of 1.68 μ_B/Ce-ion when fitting to a system that is an isolated doublet (and 2.33 μ_B/Ce-ion when fitting to a pair of doublets). Moreover, even though the values for χ differ by 30% (Fig. 2.4) between the doped and undoped compounds, the low temperature unshielded moment values inferred from Eq. 2.6 remain identical, as should be expected upon minimal doping.

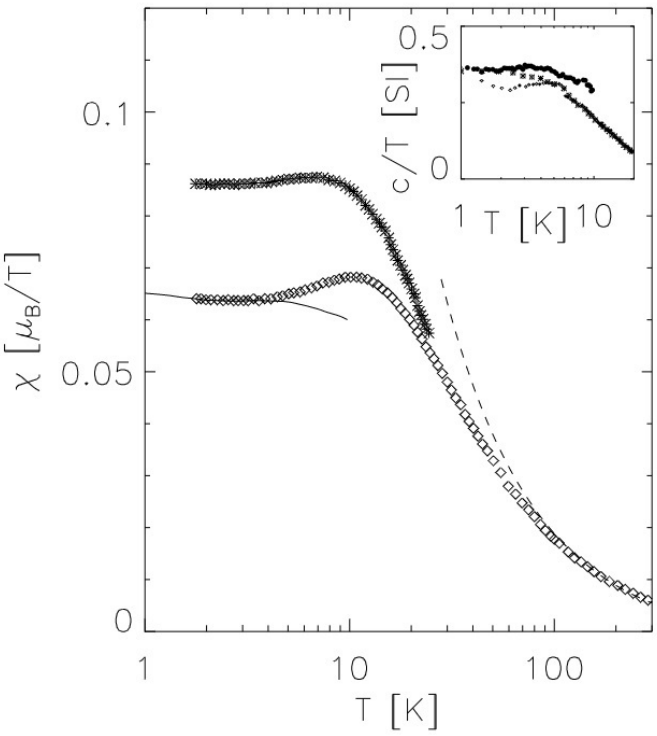

Figure 2.4: The uniform susceptibility for $CeRu_2Si_2$ (diamonds) and $CeRu_{1.94}Rh_{0.06}Si_2$ (stars) measured for an applied field of 0.1 T parallel to the c-axis[22]. The solid curve (Eq. 1.5) is the measured entropy of the sample using the data by Tabata[22] for c/T, divided by Rln2 and multiplied by the temperature dependence of the magnetic response of a three level doublet system with energy gaps of 33 abd 55 meV[35], with the ground state magnetic moment taken to be 1.21 μ_B. The measured susceptibility and the specific heat based prediction start to deviate around $T = 5$ K, with the prediction underestimating the measured susceptibility. The dashed curve is the high temperature susceptibility using the same energy gaps, but now with a ground state moment of 1.68 μ_B. The inset shows the c/T data for $CeRu_2Si_2$ measured by three groups: Laquerda et al.[44] (diamonds), Besnus et al.[43] (starts), and Tabata[22] (circles).

Applying Eq. 1.5 to Fig. 2.4 in the intermediate temperature regime ($5 < T < 30$ K), we observe clear deviations (even when taking into account the variations seen in the specific heat curves, see inset of Fig. 2.4). A similar deviation was seen in the doped $Ce(Fe_{0.755}Ru_{0.245})_2Ge_2$ when isolated clusters formed below $T_K = 10$ K. Assuming isolated clusters also form in $CeRu_2Si_2$, we expect to see their super spins contribute to the susceptibility; the difference being that once the clusters form in $CeRu_2Si_2$, they do contribute to the susceptibility but they can still dissipate upon

lowering T[13]. This is in contrast to what is seen in $Ce(Fe_{0.755}Ru_{0.245})_2Ge_2$ where the isolated clusters are protected from any further Kondo shielding owing to the static nature of the shielding distribution. We cannot ascertain whether the above scenario is a reasonable interpretation for this discrepancy or not, however we do know from neutron scattering data that isolated clusters begin to appear around $T_K = 24$ K[22]. Thus, in the intermediate temperature regime ($5 < T < 30\,\mathrm{K}$), isolated clusters likely begin to appear and their super spins contribute to the susceptibility.

We end this subsection with a discussion of Eq. 2.6. A temperature independent ratio of the susceptibility and the linear coefficient of the specific heat is anything but a new finding: the Wilson ratio R_W captures exactly this:

$$R_W \equiv \frac{\pi^2 k_B^2 \chi}{3\mu_B^2 \gamma} \quad \left(= \frac{g_J^2 J_{\mathrm{eff}}^2 \pi^2}{3\ln 2} = 4.75 g_J^2 J_{\mathrm{eff}}^2 \right), \tag{2.7}$$

where for the part in brackets we have used Eq. 2.6 to evaluate the ratio. Using the measured values for $CeRu_2Si_2$ ($\gamma = 0.38$ J/mol/K^2 and $\chi(T = 1.8\ \mathrm{K}) = 0.064$ μ_B/T/Ce-ion), we find $R_W = 6.9$ and a corresponding moment of 1.21 μ_B. However, Eq. 2.6 does *not* represent the standard Wilson ratio: the Wilson ratio pertains to the electronic susceptibility and the electronic specific heat[1]. We arrived at a T-independent ratio based on the susceptibility associated with localized, unshielded moments and the specific heat reflecting the disappearance of these moments; the two entities that go into the ratio do not involve the effective electron mass nor the density of states at the Fermi-level.

2.3.3 Super-paramagnetic Response

When clusters are present at low temperatures, some of these clusters will have a large super spin. In fact, this super spin is on average of the order of $2-3$ μ_B as we

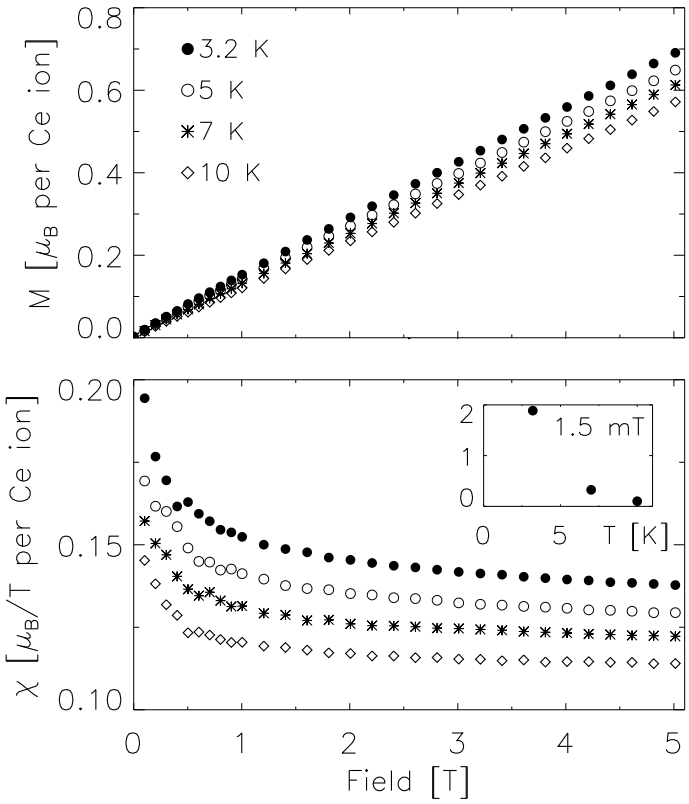

Figure 2.5: Top Panel: Magnetization data[33] for $Ce(Fe_{0.755}Ru_{0.245})_2Ge_2$ as a function of applied field along the c-axis for the temperatures indicated in the figure. Bottom Panel: Displays the accompanying susceptibility data for $Ce(Fe_{0.755}Ru_{0.245})_2Ge_2$. Note, the upturn at fields below $H = 1\,\mathrm{T}$. The inset shows the temperature dependence of the susceptibility, on the same scale, in a very small applied field of 1.5 mT.

show in the next section, with some rare clusters that have a very large super spin. Such very large clusters take on the role of ferromagnetic entities, capable of locally enhancing the applied external magnetic field, i.e., when clusters with the largest super spin align with the external magnetic field, they themselves enhance the external field, more strongly allowing neighboring super spins to align with the external field. This leads to a rapid growth in the susceptibility known as a super-paramagnetic response[45]. We show in Fig. 2.5 and 2.6 that this super-paramagnetic response is present in both $Ce(Ru_{0.755}Fe_{0.245})_2Ge_2$[33] measured at low temperatures and in high-purity $CeRu_2Si_2$[26] measured at very low temperatures and very low fields. While

a super-paramagnetic response is to be expected when ferromagnetic contamination is present in the sample, the level of which can be calculated[45] to be on the order of $10^{-3}\,\mu_B$ per Ce-ion for $CeRu_2Si_2$ (or an impurity level of 1 : 1000). This level of impurity is extremely large considering the starting materials for $CeRu_2Si_2$ were of $5N$ purity. We also mention that Tabata[22] observed this behavior in $CeRuRhSi_2$ and observed that it could not be satisfactorily explained by modeling it with the Kondo disorder model. Note, the Kondo disorder model does not include the formation of clusters.

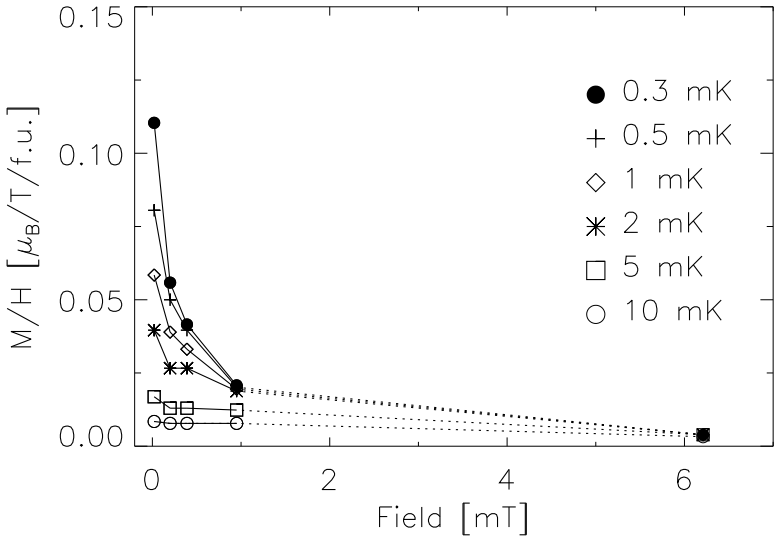

Figure 2.6: The susceptibility as a function of applied field a few tens of a degree away from the c-direction[26] for $CeRu_2Si_2$ at very low temperatures. The data have been normalized to the observed paramagnetic, temperature independent susceptibility[26] measured for $T >$ 50 mK, that is, the zero on the vertical axis corresponds to this paramagnetic level. The sharp upturn in the susceptibility below $H = 1$ mT is quite pronounced, especially as the temperature is lowered to $T = 0.3$ mK.

Based on the prevalence of the observation of this super-paramagnetic effect in multiple samples, we believe it is much more likely that we are actually seeing a feature of the system's response rather than a manifestation of unintended contamination at a level exceeding the purity of the starting ingredients. We can also turn the

reasoning around: should clusters be present, then percolation theory[41] tells us that there must be a large number of clusters with a net moment, and a small number of clusters with a very large net moment. Therefore, for the cluster model to be valid, we must observe a super-paramagnetic response. While the presence of this effect is not necessarily proof of the presence of clusters, an absence of this effect would have implied an absence of (large) ordered clusters. In summary, the cluster scenario does offer a very natural explanation for the super-paramagnetic behavior observed in the 122-systems, even in compounds that have been prepared using a purity of starting materials higher than the observed ferromagnetic effects should they be attributable to impurities.

2.3.4 AC Susceptibility

We have shown substantial evidence for ordered cluster formation in stoichiometric $CeRu_2Si_2$ through neutron scattering experiments, susceptibility and specific heat measurements. A series of ac-susceptibility and magnetization experiments performed by Takahashi et al.[26] at very low temperatures (milliKelvin range) and fields (milliTesla) showed considerable temperature and field dependence where earlier experiments at higher temperatures ($T > 2\,\mathrm{K}$) and larger fields ($0.1 - 0.2\,\mathrm{T}$) had found[29] that the susceptibility would reach a constant value for $T < 10\,\mathrm{K}$ (see Fig. 2.4), although at a level that was strongly dependent on rhodium concentration[22].

From the ac-susceptibility data (see Fig. 2.7), Takahashi *et al.*[26] determined two vastly different Ce-moment values; one moment value of $0.01\mu_B$ per Ce-ion from the low $\mu_B H/k_B T$-region using a Curie-behavior fit to the susceptibility data and another much lower (by nearly a factor of 1000) moment value from the saturation

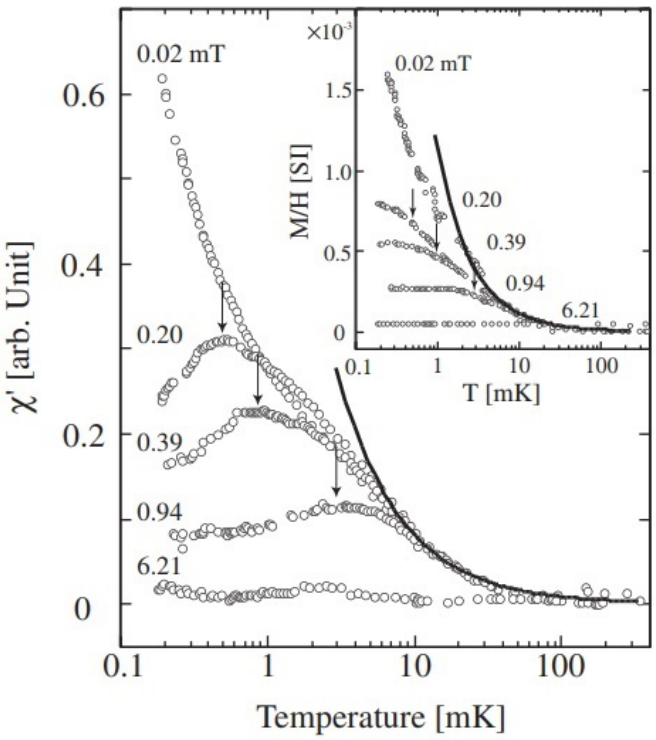

Figure 2.7: Figure reproduced from Takahashi *et al.*[26]. The low temperature ac-susceptibility ($\partial M/\partial H$) of $CeRu_2Si_2$ for extremely small applied field values. Inset: The low temperature static susceptibility of $CeRu_2Si_2$ in the same temperature region and applied field values. Plotted on a logarithmic scale. The arrows indicate the peaks observed in both curves, while the solid lines are Curie law fits.

magnetization at high $\mu_B H/k_B T$-values. In fact, there is a third moment value that can be inferred from their data[26]: the ac-susceptibility (Fig. 2.7) shows a distinct maximum in fields of 0.2, 0.39, 0.95 mT at temperatures of $T = 0.5$, 0.9, and 3 mK respectively.

Clusters provide a natural explanation for these disparate moment values. Considering that $CeRu_2Si_2$ is an Ising system at low T, we know that the super spin of any given cluster, J_{cluster}, can have two possible orientations along the easy axis[35]. Therefore, the ac-susceptibility associated with a particular cluster with super spin

J_{cluster} is given by

$$\chi_{ac} = \frac{(g_J J_{\text{cluster}} \mu_B)^2}{k_B T} \frac{1}{\cosh^2(g_J J_{\text{cluster}} \mu_B H / k_B T)}. \tag{2.8}$$

Thus, the ac-susceptibility peaks at a maximum value of $k_B T = 1.296 g_J J_{\text{cluster}} \mu_B H$ and therefore, we can apply Eq. 2.8 (and its predicted peak position) to associate the observed peaks (Fig. 2.7) with a Ce-moment value of $3 \pm 0.5\ \mu_B$. We find this moment value to differ by a factor of up to 100,000 when compared to the other moment values determined by the authors and far exceeds the value for a single unshielded Ce-ion. Thus, even though $CeRu_2Si_2$ is generally considered to be well understood as a compound on the verge of a SDW transition, the scrutiny reveals that only a rudimentary understanding of the low temperature physics in $CeRu_2Si_2$ can be claimed. We show in the following how cluster formation can account for this discrepancy in average moment values.

We stop briefly and take note that the magnetization level referred to as a saturation magnetization by Takahashi *et al.*[26] where the values become independent of H/T is not a saturation magnetization as normally understood. Takahashi *et al.*[26] used this saturation magnetization to determine a saturation moment of $10^{-5}\ \mu_B$ per Ce-ion. Despite the fact that the magnetization becomes independent of H/T for $H/T \geq 1$ T/K, the actual level was seen to still depend on applied magnetic field (Fig. 2.8), and thus, these values should not be viewed as a saturation magnetization. We also note that the data were presented with reference to the paramagnetic level observed in the susceptibility for T > 50 mK. It is unclear what reference level the author's are referring to, whether presented with reference to the level of 0.03 emu/mol[22, 29] as measured in much higher fields for T > 1 K or whether an entirely

different paramagnetic level was used as an offset. Also, while the authors did not discuss the moment value associated with the peak in the ac-susceptibility, they did rule out[26] small amounts of disorder and a putative spin glass phase as the cause of the factor $1,000$ discrepancy between susceptibility and saturation magnetization inferred Ce-moment values.

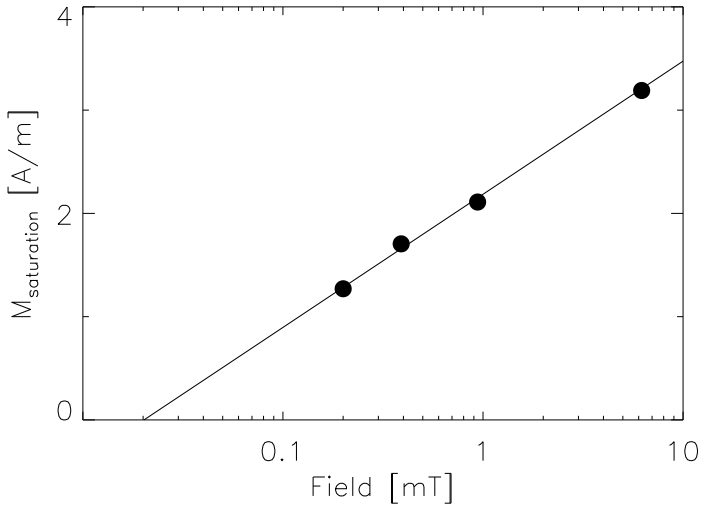

Figure 2.8: The saturation magnetization for $CeRu_2Si_2$ measured in low fields and plotted as a function of the logarithm of applied field[26]. Fitting the data to a log dependence, we find the saturation magnetization reaches zero at $H = 0.02\,\mathrm{mT}$.

In order to understand the factor of 1,000 difference seen in moment values as well as the even much larger moment value observed in the ac-susceptibility, we invoke cluster formation in stoichiometric $CeRu_2Si_2$. Based on the understanding of cluster formation caused by a static (permanent) distribution of Kondo temperatures, we propose the following for stoichiometric $CeRu_2Si_2$ based on a dynamic distribution of Kondo temperatures. At any moment in time, $CeRu_2Si_2$ is subject to a distribution of Kondo temperatures. The Kondo temperature at any given Ce-site dictates

whether that Ce-moment will be (mostly) shielded, or persist as an unshielded moment. Therefore, at any temperature we can expect manifestations of percolation physics, and at low temperatures we can expect the appearance of isolated clusters. As in $Ce(Ru_{0.755}Fe_{0.245})_2Ge_2$, the moments on isolated clusters have to line up with their neighbors due to finite-size effects, provided that the temperature is low compared to the allowed quantized energies of disordering spin fluctuations on the cluster.

An isolated cluster can acquire a net super spin. When the moments line up inside a cluster, pairs of neighboring moments will cancel each other out, but there will be dangling moments on the surface of the cluster, the sum of which is known as super spin. Of course, surface is a term we use loosely here as the topology of a cluster that formed by random removal of moments is closer to that of a fractal than that of a solid object.[41] In susceptibility measurements, one observes only the net moments of the clusters. The net moment only represents a small fraction of all the moments on any given cluster given the anti-ferromagnetic ordering of clusters. Additionally, only a small fraction of the moments will end up in clusters. For reference, in quantum critical $Ce(Ru_{0.755}Fe_{0.245})_2Ge_2$, 27% of the moments are believed to end up in clusters at the QCP. This number corresponds to the percolation threshold for protected percolation.[55] For large clusters, somewhere in the neighborhood of 1% of the moments may end up not being compensated, as we detail below. The main consequence of cluster formation is that the entities that give rise to the susceptibility signal are far less numerous than the number of Ce-ions in the sample: there are far fewer clusters than there are unit cells, and there are far fewer uncompensated moments on a cluster than there are compensated moments on a cluster.

We illustrate how these considerations lead to an artificially large ratio between the moment determined from the high temperature susceptibility compared to that determined from the saturation magnetization. When we determine the moment per Ce-ion from the high temperature susceptibility, we compare the measured signal to $N\mu^2$, with N the known number of Ce-ions in the sample. Similarly, for determining the moment based on the saturation magnetization μ_s, we compare the signal to $N\mu_s$. We can then simply divides both terms by N and compares the two moments. Provided saturation has been reached, the two moment values should be identical. However, when only a fraction f of all the moments end up being the uncompensated cluster moments that produce the measured susceptibility and magnetization, then the normalization is wrong by a factor of f, and after taking the square root of $N\mu^2$, the factor f does not cancel, but we end up with an overestimation of μ based on the high temperature susceptibility by a factor of $1/\sqrt{f}$. From computer simulations we estimate f to be in the range of $0.1 - 2\%$, accounting for a factor of $5 - 30$ in the observed[26] discrepancy of $\sim 1,000$ discussed previously.

There are three more factors that reduce the observed discrepancy. First, the authors[26] assumed that the high temperature term in the susceptibility would be proportional to $\mu^2/3k_B$, but for an Ising system, the proportionality is given by μ^2/k_B, removing a factor of $\sqrt{3}$. Second, the level of discrepancy is dependent on the applied field (Fig. 2.8), with the highest field in the study ($H = 6.2$ mT) yielding the smallest discrepancy factor of 720. Using the data in Fig. 2.8, the discrepancy would be reduced by another factor of 2 by the time the applied field reaches 0.1 T. Third, when there is a distribution of net moments, then the moment derived from the high temperature

susceptibility will exceed that of the saturation magnetization. This is a result of averaging over μ^2_{cluster} versus averaging over μ_{cluster}. Large net moments will skew the μ^2_{cluster} averaging towards higher values. For example, imagine applying the averaging procedure to a system of 101 clusters, one with a net moment of 100, and 100 clusters with a net moment of 1. With these numbers the moment determined from the saturation magnetization would be 2, but the one determined from the susceptibility would be 10. This illustrates how large clusters can skew what is measured in the high temperature susceptibility. When we combine all these factors, we see that the discrepancy is greatly reduced. Given the uncertainties, we cannot tell whether it will disappear completely, but from computer simulations (to be discussed below), we estimate that the discrepancy is reduced to within a factor of $5 - 10$.

The appearance of clusters with a super spin leads to a very natural explanation for the high-moment value peak in the ac-susceptibility, as well as the overall small level for the average moment. We performed computer simulations to model the protected percolation network [55] described in Section 1.4 in order to determine the cluster super spins for a given cluster distribution. We chose a lattice of size $400 \times 400 \times 400$ magnetic sites using a body-centered nearest neighbor topology. We followed the restriction governed by protected percolation, namely sites are only removed from the lattice spanning cluster. Sites were characterized by 3 integer coordinates. The individual moment directions (up/down) were determined by the z-direction integer being odd or even, representing an Ising system with anti-ferromagnetic interactions. Periodic boundary conditions were implemented to ensure the data were free from any artificial edge-induced effects. We removed sites until the last connection in

the lattice spanning cluster was severed such that the cluster would no longer have a single continuous path from one side of the lattice to the other; in other words, until the percolation threshold was reached. We used the distribution of clusters at the percolation threshold in the comparison with experiment. We kept track of the number of uncompensated moments in each cluster and used this to determine the super spin of all clusters present. The data from the simulations are shown in Fig. 2.9. Calculating the average moment, and the average of the square of the moments, we find a mismatch factor of 18 between the two. Including the two additional factors discussed previously (a factor of 2 to account for the dependence of the saturation level on applied field, and the factor of $\sqrt{3}$), we find an ensuing mismatch about 100 times smaller than the mismatch reported by Takahashi *et al.*[26].

We note here that this protected type of percolation[55] is the one that describes the clusters that form[33] in heavily doped $Ce(Ru_{0.755}Fe_{0.245})_2Ge_2$. Of course, a fleeting distribution of Kondo temperatures is not the same as a permanent distribution, nor is stoichiometric $CeRu_2Si_2$ truly quantum critical; for that we need[22] 3.5% rhodium doping on the ruthenium sites. Notwithstanding, using the cluster distribution at the percolation threshold generated through random moment removal while leaving isolated clusters intact is expected to shed light on how many moments become dangling moments (uncompensated), how many clusters we can expect to see appear that have a super spin, and what the average net moment is associated with such super spins.

At the threshold of this finite-sized simulation, 24.3% of the moments are in isolated clusters, and 3% are in the lattice spanning cluster that is about to fracture.

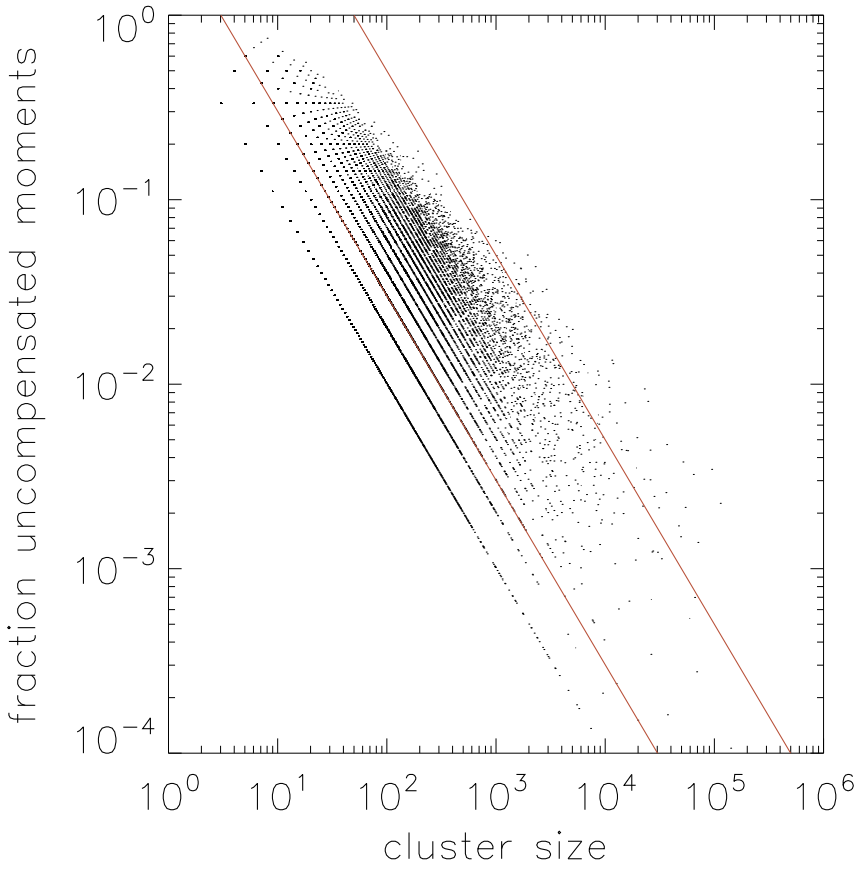

Figure 2.9: The distribution of uncompensated moments as a function of cluster size as determined from a computer simulation at the percolation threshold. Clusters of size one and clusters with a zero net moment have been omitted. The two solid lines correspond to an average number of uncompensated moments per cluster of 3 (lower line) and to a high super spin of 50 uncompensated moments (upper curve).

This 0.243 fraction of the 64 million moments (400^3) are divided over 2.6 million clusters, or 0.041 clusters per lattice site using percolation notation.[41] Removing clusters with a super spin of zero (since they do not show up in magnetization and susceptibility experiments) and clusters of size one (since these are simply isolated moments that are not in an environment that protects them from shielding), we find that the total fraction (compared to the number of sites in the lattice) of uncompensated moments is 0.0147. Thus, the average moment per Ce-ion is of the order of 0.02

μ_B using the value of 1.21 μ_B per uncompensated moment (see Fig. 2.4). This value is in agreement with μSR experiments.[47] The average number of uncompensated moments per cluster equals 1.87. Note, this is the average number of uncompensated moments of all clusters whose super spin does not equal zero and who have more than one cluster member, divided by the total number of such clusters. This large average value is what determines the peak position in the ac-susceptibility: this position is independent of any normalization we performed to determine the value of the average moment from susceptibility or magnetization data, and it is not affected by whether the clusters are fleeting or static in nature. Note that it is actually the full distribution of cluster moments that determines the exact peak position as the averaging involves μ^2_{cluster}. For completeness, we mention that the largest net moment of a cluster in this simulation was a cluster with $94,000$ members and a net moment of 326 uncompensated moments (see Fig. 2.9).

Thus, a distribution of clusters successfully explains the very large moment value observed in the peak in the ac-susceptibility (as we will discuss shortly when scrutinizing the ac-susceptibility[26]) as well as the smallness of the moment value when inferred from a Curie-Weiss law and normalizing the average moment value to the number of lattice sites. Whereas it does not fully remove the discrepancy in the moment values found by Takahashi et al.[26] of ~ 1000, it does greatly reduce the discrepancy to a factor of about 10. Even taking into account that $CeRu_2Si_2$ is not exactly at the QCP but extremely close, and that the applied field makes an angle of a few tens of a degree with the easy axis, we still cannot remove this discrepancy factor entirely. This remaining factor of 10 mismatch may actually be the fact that

the distribution of clusters seen in the stoichiometric $CeRu_2Si_2$ is dynamic in nature as the dynamic nature leads to a different experimental response when different measurement techniques are used. Scrutinizing the literature data[26] for dc- and ac-susceptibility, we see that the dc susceptibility follows the Curie-Weiss law down to 2mK, while the ac susceptibility only does do down to 8mK. This hints at the fleeting distribution of clusters does indeed create a different signal based upon the chosen measurement technique. In dc measurements, the sample is moved physically during the measurement cycle, whereas in ac measurements the signal is being detected instantaneously. Thus, if the clusters form and disappear on a timescale faster than the measurement cycle, we may not see evidence of their presence. However, since ac-susceptibility measurements detect clusters the moment they form, ac-susceptibility measurements may help to reveal the dynamic nature of any cluster distribution present.

We compare the ac-susceptibility data taken by Takahashi in a field of 0.2 mT and for very small temperatures (mK) to the calculated ac response for the collection of clusters (in Fig. 2.9) using Eq. 2.8. In order to model the ac-susceptibility, we assumed a value for the unshielded Ce-moments of 1.21 μ_B (the value determined from the low temperature fit using Eq. 2.6 in Fig. 2.4). We have applied an overall vertical scale factor to accommodate the arbitrary units the data[26] were reported in. We show the results of the comparison in Fig. 2.10.

The agreement between the calculated curve based on the simulated cluster distribution and the measured ac-susceptibility data is highly encouraging (Fig. 2.10). Whereas there clearly is not perfect agreement, there is no trace of a large discrep-

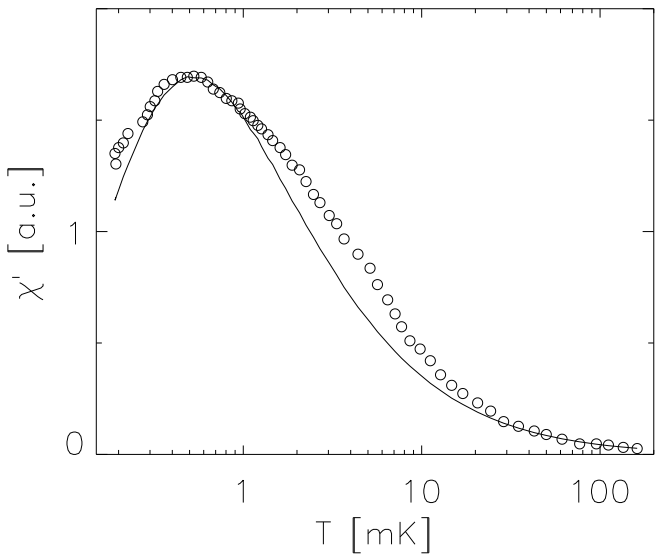

Figure 2.10: The measured ac susceptibility[26] in an applied field of 0.02 mT (circles). The solid line is the result of a computer simulation where each cluster at the percolation threshold was analyzed for uncompensated moments to arrive at the net moment (super spin). The temperature dependence of each super spin was modeled using (Eq. 2.6), with each uncompensated moment in these clusters taken to be 1.21 μ_B. This number for the unshielded Ce moments was inferred from the ratio of the uniform susceptibility and the specific heat at low temperatures (see text). An overall scale factor was applied to accommodate the arbitrary units the data were reported in. Note, the agreement for both the peak level as well as for the higher temperature. In addition, the position of the peak is also in agreement between the data and simulation. There is zero indication of a mismatch of a factor of $100,000$.

ancy between the higher temperatures (the Curie-Weiss law region) and the low temperatures (the saturation magnetization region). For reference, the peak position corresponds to a temperature where the magnetization in the magnetization measurements[26] had already reached more than 90% of its saturation value. Thus, with one (vertical) scale factor we are able to capture all three moment values (as the peak position of the ac-susceptibility does not depend on the vertical scale factor). As such, we conclude that the discrepancy of a factor of $\sim 100,000$ between the highest and lowest moment values as determined from the peak in the ac-susceptibility and the saturation magnetization can be accounted for when taking into account that

clusters form, and that these clusters have a fleeting nature.

We end this section with a discussion on the in-phase and out-of-phase components of the ac-susceptibility, also referred to as the real part χ' and the imaginary part χ'' of the complex susceptibility χ. The real part represents the response to the applied external field, whereas the imaginary part yields information about the dissipation of this response. Typically, the imaginary part is small compared to the real part unless the system is close to a phase transition. In contrast, Takahashi *et al.*[26] showed that the imaginary part displayed an identical temperature dependence to the real part (Fig. 1 in reference [26]). In fact, in an earlier publication[48] it was reported that $\chi' \approx \chi''$ at a frequency of 16 Hz. Using more measurement frequencies and assuming the validity of the thermodynamic theory for a magnetic system relaxing through coupling with the lattice [49], the authors inferred a relaxation time of approximately 11 ms.

The dynamic nature of the Kondo distribution allows for an alternative explanation in $CeRu_2Si_2$. Because of the ever-changing distribution, resulting in an ever-changing cluster morphology, we could also view the measured ac-response as clusters appearing spontaneously and aligning with the external field. But these clusters also disappear spontaneously, with the result that the signal we observe would not be very strongly dependent on the field-amplitude of the probing ac field, but much more on the primary static field. If this were the case, then we actually would expect that $\chi' = \chi''$ as clusters appear and disappear, neither in-phase nor out-of-phase with the ac-signal, but with an overall magnetization only depending on the static field. In ac-susceptibility measurements, the sample is placed in an ever present (static)

magnetic field while a much smaller (dynamic) magnetic field probes the sample for changing magnetization. We are not sure what will prove the better explanation for the observed equality of χ' and χ'' for all fields and temperatures reported in reference [26], but if it turns out to be the fleeting nature of clusters in stoichiometric systems, then the ac-susceptibility could act as a direct test for their presence.

In summary, we have shown that in disorder free stoichiometric $CeRu_2Si_2$, a dynamic distribution of interatomic separations is induced by zero-point motion. This distribution of interatomic separations will upon cooling, lead to a distribution of Kondo shielding temperatures and a dynamic percolation network forms. These dynamic isolated clusters dominate the low temperature response of $CeRu_2Si_2$. This is very similar to $Ce(Fe_{0.755}Ru_{0.245})_2Ge_2$, bearing in mind that the chemical doping of ruthenium induces the static distribution of interatomic separations that creates the static distribution of clusters seen in $Ce(Fe_{0.755}Ru_{0.245})_2Ge_2$ (Section 1.5). Next we apply the same methodology to another stoichiometric system close to a QCP: $YbRh_2Si_2$ (Chapter 3). We demonstrate that clusters are also present in that system.

Chapter 3

Cluster Formation in $YbRh_2Si_2$

3.1 Introduction

We investigate the potential presence of spontaneous clusters in the heavily studied $YbRh_2Si_2$ compound for which, unfortunately, neutron scattering data have not been published. However, we show that the specific heat and susceptibility data are naturally interpreted when ordered magnetic clusters are taken into account.

3.2 $YbRh_2Si_2$ vs $CeRu_2Si_2$ and $Ce(Fe_{0.755}Ru_{0.245})_2Ge_2$

$YbRh_2Si_2$ is a heavy fermion system located very close to an antiferromagnetic quantum critical point. $YbRh_2Si_2$ crystallizes in a 122−tetragonal lattice structure very similar to $CeRu_2Si_2$ and $Ce(Fe_{0.755}Ru_{0.245})_2Ge_2$. $YbRh_2Si_2$ displays easy-plane magnetic anisotropy (the magnetic moments like to align in-plane) which is different from the Ising character found in $CeRu_2Si_2$ and $Ce(Fe_{0.755}Ru_{0.245})_2Ge_2$ (magnetic moments align along the easy c-axis)[62]. At zero fields, the system shows very weak AF order (T_N = 70 mK, solid line boundary in Fig. 3.1), while small fields (B_c = 0.06 T) applied perpendicular to the c-axis (field applied in-plane) can push this system to its QCP and to a suppression of the ordering[63]. At this point, $YbRh_2Si_2$ displays strong non-Fermi liquid behavior down to the lowest temperatures and specific

heat[66], resistivity[68], and ac-susceptibility[67] data have been published on this system in this temperature region. Thus, $YbRh_2Si_2$ is an excellent candidate to look for cluster formation. Note that unlike the compounds we previously discussed, this stoichiometric system "misses" the QCP by being in an ordered phase.

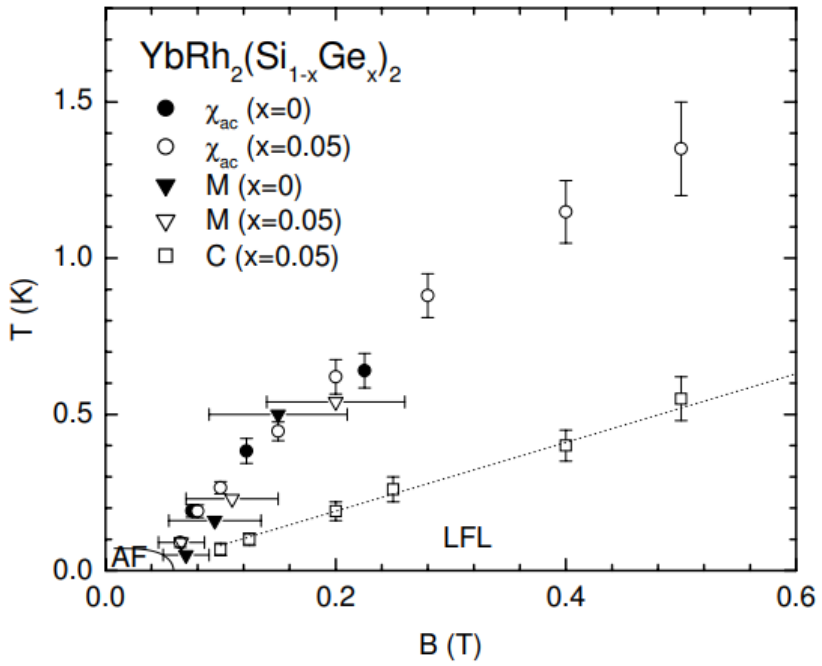

Figure 3.1: Figure adapted from Gegenwart *et al.*[65]. Temperature vs magnetic field phase diagram for $YbRh_2Si_2$ (open symbols) and $YbRh_2(Si_{0.95}Ge_{0.05})_2$ (closed symbols). The magnetic field was applied perpendicular to the c-axis. The positions of the peaks in ac-susceptibility $\chi(T)$ (circles) and the inflection points of differential susceptibility $\mathrm{d}M/\mathrm{d}B$ (triangles) are shown (see text). The maxima in specific heat coefficient (squares) (which according to Gegenwart *et al.*[63] represents the upper limit of Fermi Liquid behavior) are shown as well.

In the compounds previously discussed, the size of the lattice spanning cluster decreased upon cooling as more and more moments become Kondo shielded and break away from the infinite cluster (see left panel of Fig. 3.2). In $YbRh_2Si_2$, the situation is slightly more complex due to the system ending up in an ordered phase upon cooling (rather than disordered as we have previously discussed in $CeRu_2Si_2$ and $Ce(Fe_{0.755}Ru_{0.245})_2Ge_2$). We propose that upon cooling in $YbRh_2Si_2$, more and more

moments become shielded, i.e., the strength of the lattice spanning cluster decreases with decreasing temperature until the ordering temperature T_N. At T_N, the infinite cluster breaks apart entirely into groups of ordered moments. We believe that the super spins of these clusters can align, which constitutes the antiferromagnetic order seen. This proposal is illustrated in the right panel of Fig. 3.2. We further illustrate this proposal in Fig. 3.3 by amending the phase diagram of $YbRh_2Si_2$ (Fig. 3.1). We see from Fig. 3.3 and 3.2 that increasing the magnetic field can push the system further from the QCP or vice versa, a decreasing magnetic field can drive the system towards the QCP.

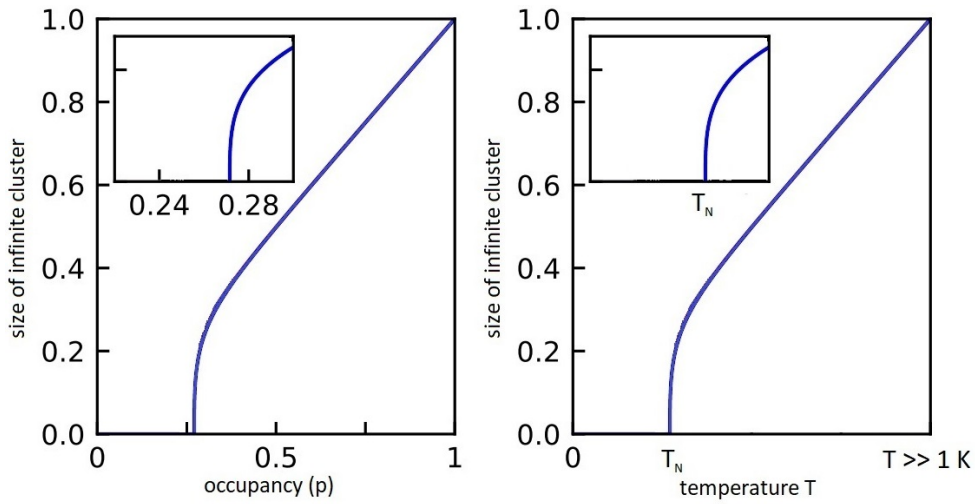

Figure 3.2: Left Panel: Size of the infinite (lattice spanning) cluster as a function of occupancy p. The inset shows the exact occupancy the size of the infinite cluster goes to zero, the percolation threshold. Right Panel: Size of the infinite cluster proposed in $YbRh_2Si_2$ as a function of temperature. Upon cooling, more and more moments become shielded and the size of the infinite cluster decreases until T_N where the infinite cluster has completely broken apart into ordered magnetic clusters.

We focus on the data collected by a group of Custers and Gegenwart who took low temperature and low field measurements on high quality samples and who have disseminated their evolving views on this system in various publications during 2000 –

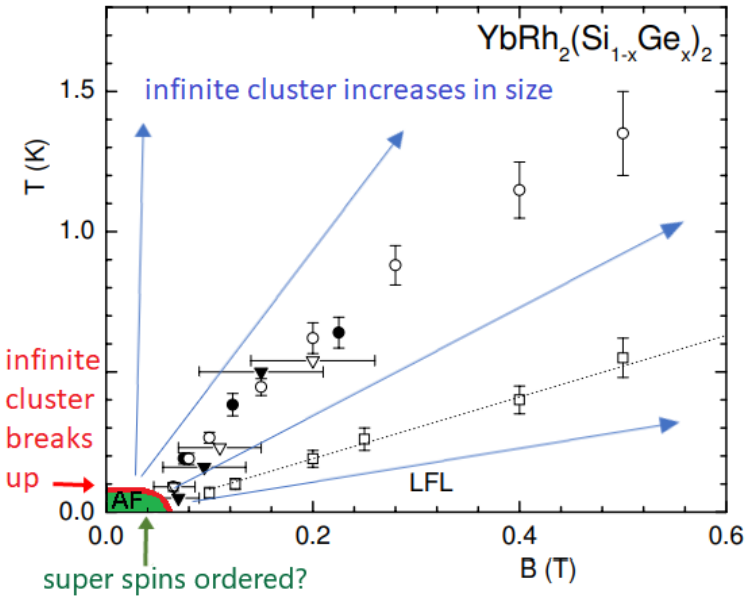

Figure 3.3: See Fig. 3.1 for precise meaning of the symbols. Temperature vs magnetic field phase diagram for $YbRh_2Si_2$ (open symbols) and $YbRh_2(Si_{0.95}Ge_{0.05})_2$ (closed symbols). As more and more moments become shielded upon cooling, the more and more the size of the lattice spanning cluster decreases. Thus, we can make the assumption that the infinite cluster increases in size with increasing temperature and/or magnetic field (shown as blue arrows). The red arrow indicates the point at which the infinite cluster breaks apart and the green shaded region depicts the area in which isolated cluster super spins may become ordered.

2010[63, 65–68]. Driving $YbRh_2Si_2$ towards its quantum critical point can be done in multiple ways, by chemical doping of germanium for silicon, as well as by applying a magnetic field. Chemical doping of isoelectronic but larger germanium for silicon atoms at a concentration of 1 : 20 atoms ($x = 0.05$) suppresses the ordering temperature from $T_N = 70$ mK down to $T_N = 20$ mK and subsequently the critical field from $B_c = 0.06$ T to $B_c = 0.027$ T. Upon cooling from 1 K down to T_N, evident non-Fermi liquid behavior is observed[63] (the dotted line in Fig. 3.1 is the upper limit for Fermi liquid behavior according to Gegenwart *et al.*[63]).

In summary, the behavior in $YbRh_2Si_2$ is markedly different from $CeRu_2Si_2$ and $Ce(Fe_{0.755}Ru_{0.245})_2Ge_2$ with these systems being on the verge of long ranger order but

located just in the paramagnetic (disordered) phase. In contrast, $YbRh_2Si_2$ is close to the border of long range magnetic order but is in an ordered phase showing very weak AF order[63]. Thus, in $Ce(Fe_{0.755}Ru_{0.245})_2Ge_2$ and $CeRu_{1.94}Rh_{0.06}Si_2$, doping is used to push the system from a disordered phase closer to the ordered phase to reach their respective quantum critical point, whereas in $YbRh_2Si_2$, an ordered system is driven closer to the disordered phase (through the doping of germanium or the application of a magnetic field) to arrive at its quantum critical point. This makes $YbRh_2Si_2$ a significantly more complex system, as it is already ordered and order must be suppressed to drive the system to quantum criticality. Therefore, interpretation of cluster formation will not be as straight-forward as in $Ce(Fe_{0.755}Ru_{0.245})_2Ge_2$ or $CeRu_2Si_2$, especially as we have not had to consider the effects of an external field in stepping through the phase diagram. However, we will show that the specific heat and susceptibility measurements are naturally interpreted when ordered magnetic clusters are taken into account.

3.3 Dynamic Cluster Formation in $YbRh_2Si_2$

3.3.1 Specific Heat

Custers *et al*. performed[66] specific heat measurements on single crystals of $YbRh_2Si_2$ and $YbRh_2(Si_{0.95}Ge_{0.05})_2$ which showed a low temperature peak associated with an ordering temperature T_N (Fig. 3.4). The integrated $c)el/T$ curve showed that the entropy associated with the ordering was a mere 0.008Rln2[68]. From Fig. 3.4, we see c_{el}/T is proportional to -ln(T) for temperatures greater than 0.3 K while magnetization measurements performed by Gegenwart *et al*.[63] indicate a second order phase transition. Extrapolating down to 0 K when c_{el}/T = constant = $\gamma_0 = 1.7 \pm 0.2$ J/K^2

reveals that the loss of entropy associated with the antiferromagnetic phase transition at T_N is only 0.008Rln2[68]. Performing a similar extrapolation on dc magnetization data[63] towards zero field reveals a moment value of $\mu_s < 0.1\mu_B$, indicating that the size of the ordered moments present in the AF region is much smaller than the effective moment observed above T_N ($\approx 1.4\mu_B$)[65]. At least this is how the data have been interpreted by the group of Custers and Gegenwart [63, 65–68].

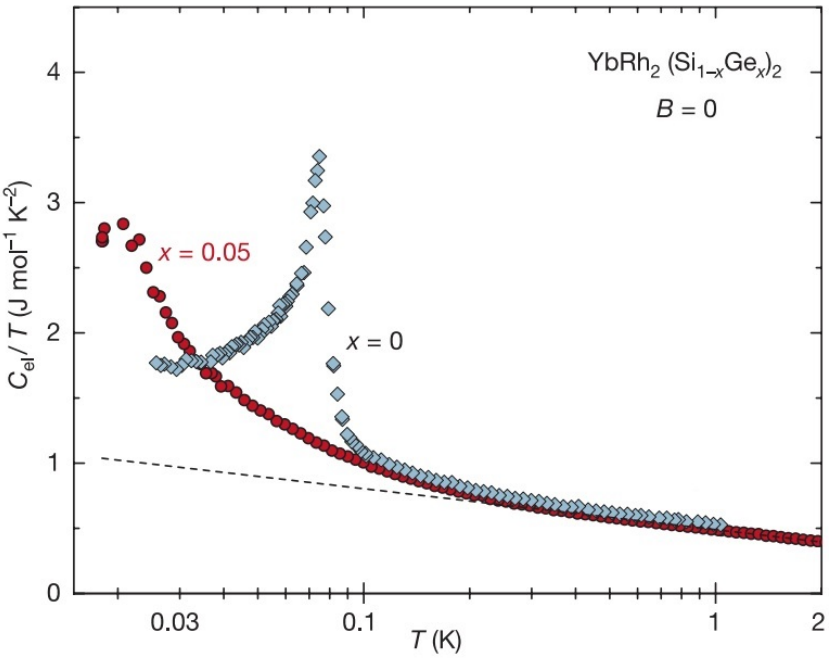

Figure 3.4: Figure adapted from Custers *et al.*[66]. The low temperature specific heat divided by temperature for high quality single crystals of $YbRh_2Si_2$ (x=0, blue squares) and $YbRh_2(Si_{0.95}Ge_{0.05})_2$ (x=0.05, red circles) as a function of temperature at zero applied field. Note the semi-logarithmic horizontal scale. The cusp at 0.07 K indicates the loss of entropy entering the ordered phase. This loss is pushed down to 0.02 K upon doping with germanium (Ge).

The extremely small entropy associated with the AF phase transition at T_N as well as the small size of the ordered moment can be naturally explained within the cluster formation scenario. Upon cooling to T_N, more and more moments become shielded from the infinite cluster and thus, the infinite cluster decreases in size upon cooling as isolated clusters form and order. At T_N, we propose that these isolated clusters

order with one another and account for the weak antiferromagnetic order seen. We can estimate the entropy involved with such super spin ordering as follows. Using the protected percolation simulations described earlier (Section 2.3.4), on average there are only 0.045 clusters per lattice site at the percolation threshold. Excluding clusters with a zero net moment and clusters of size one as they can still become Kondo shielded, we find that 0.0078 clusters per lattice site remain that can align with other clusters. When these clusters order at T_N, the entropy loss of the system will be proportional to $0.0078R\ln 2$, accounting for the experimental entropy seen in the AF transition seen at T_N[68]. This behavior can also been seen in doped $YbRh_2(Si_{0.95}Ge_{0.05})_2$ where the germanium doping has pushed the ordering down to $T_N = 20$ mK. The total net moment of all super spins present at the threshold is 0.0147 unpaired moments, therefore the average total moment per Yb ion left to order below T_N is less than $0.03\mu_B$ (taking $2\mu_B$ per surviving Yb ion as the upper limit of the moment value of a single Yb moment). Thus, the cluster scenario naturally accounts for both the small entropy and ordered moment of this transition.

Looking at the specific heat data as a function of applied field (Fig. 3.5) in $YbRh_2(Si_{0.95}Ge_{0.05})_2$ we see additional behavior attributable to cluster formation. The weak maxima associated with antiferromagnetic order and the ordering temperature T_N (as seen in Fig. 3.4) shift towards higher temperatures with the application of larger magnetic fields (Fig. 3.5). c_{el}/T is seen to be T-independent for $T(\mathrm{K}) < B(\mathrm{T})$ for all but the lowest field values. We proposed in Fig. 3.3 that applying a magnetic field pushes the system away from the quantum critical point and thus, according to the cluster formation scenario, further from the percolation threshold.

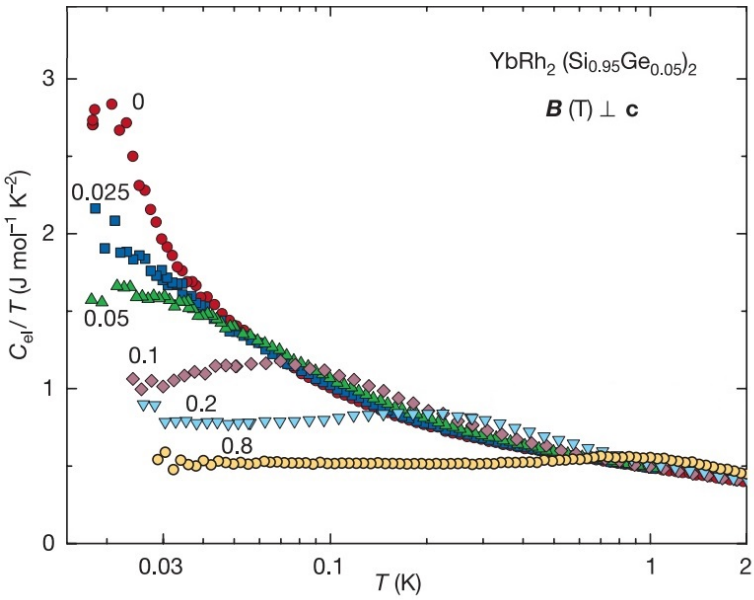

Figure 3.5: Figure adapted from Custers *et al.*[66]. The specific heat divided by temperature of a high quality single crystal of $YbRh_2(Si_{0.95}Ge_{0.05})_2$ as a function of temperature for various applied fields, displayed as a semi-logarithmic plot. Note that the curves for $B > 0.1$ T display a weak maximum, and that they trend towards constant c_{el}/T values at the lowest temperatures.

Upon cooling such a system in a magnetic field, cluster formation occurs as moments become shielded before others, but now the demise of the infinite cluster is cut off by the magnetic field. This cutoff is illustrated in Fig. 3.6. This behavior is expected as pushing a system further from the QCP also pushes the system further from the percolation threshold, i.e., the system stays in the higher occupancy ranges $p > p_c$ (see Fig. 3.2). Once the demise of the infinite cluster is cut off, cluster formation stops and the response of the system is a mixture of the infinite cluster as well as of groups of isolated clusters, a cluster froth if you will. Overall, it is the ratio of magnetic field to temperature B/T that determines the response of the system.

We now detail the high and low B/T limits and interpret the specific heat curve in terms of the cluster scenario. At small B/T values, the specific heat curve reflects the Kondo shielding of the moments on the infinite cluster and the loss of entropy

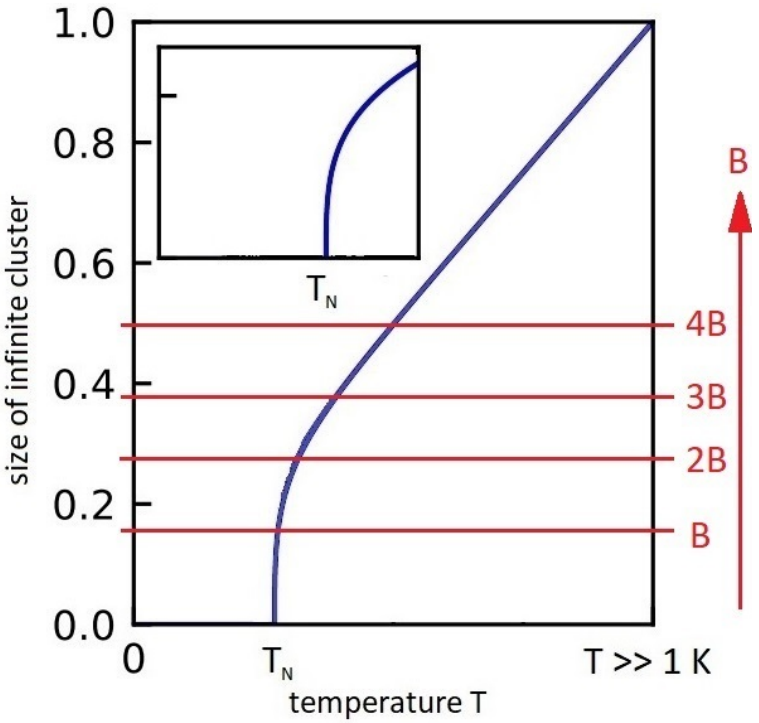

Figure 3.6: Size of the infinite cluster proposed in $YbRh_2Si_2$ as a function of temperature. Upon cooling, more and more moments become shielded and the size of the infinite cluster decreases until T_N where the infinite cluster has completely broken apart into ordered magnetic clusters. With the application of a magnetic field, the infinite cluster is cutoff (at the level of the red lines) from further demise.

associated with the breaking off of (small) clusters. As long as the demise of the infinite cluster is not cut off yet by the application of the magnetic field (red lines in Fig. 3.6), then the rate at which Kondo shielding removes entropy from the system is determined by the temperature. As a consequence, at small B/T, the specific heat curves depend on temperature, but not on applied field[66]. At the other end of the spectrum ($B/T \gg 1$), we have the situation that the demise of the infinite cluster is cut off by the external field, and cluster formation has ceased. Therefore, the only contribution left in the specific heat is the response of the (heavy i.e., $m^* \gg m_{electron}$) conduction electrons producing a response of $c/T \sim m^*$[66]. The maxima in the c_{el}/T curves for $B > 0.1$ T are interpreted as follows. The maxima reflect the highest rate

of cluster formation at a given field when the temperature is lowered. Depending on the strength of the field, these clusters can still fluctuate if B is small, while if B is large, these clusters become (fully) aligned with the applied field B.

The strength of Kondo shielding not only depends on temperature but also upon the application of an external magnetic field: lowering the field increases the Kondo interaction strength[67]. Upon lowering of the magnetic field, more and more moments become Kondo shielded, with more and more conduction electrons partaking in the shielding. These conduction electrons become increasingly more massive due to these interactions with the lattice. Thus, upon lowering the magnetic field, not only does the interaction strength increase, increasing the effective mass m^* of any conduction electrons involved in Kondo shielding but it also increases the number of conduction electrons involved in this dynamic Kondo shielding process. It is the combined effect of an increase in m^* as well as an increase in the number of these heavy electrons which causes the increase in the constant value seen in c_{el}/T with decreasing field in the region when $B/T \ll 1$.

3.3.2 Entropy and Resistivity

Linear behavior in the resistivity of $YbRh_2Si_2$ can be naturally explained taking into account magnetic clusters. Gegenwart *et al.*[68] observed that the low temperature entropy of $YbRh_2(Si_{0.95}Ge_{0.05})_2$ scales linearly in temperature as (left panel in Fig. 3.7) while separate experiments revealed that the resistivity scaled linearly in a similar temperature regime (right panel in Fig. 3.7)[67].

From Section 1.5.2, we know that the entropy of the system is locked into the infinite cluster and therefore the entropy of the system is determined by the number

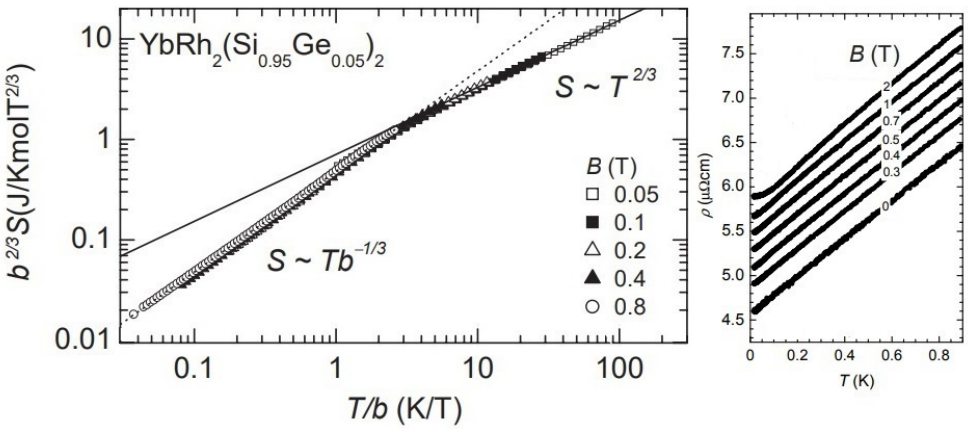

Figure 3.7: Figure adapted from [68] and [67]. Left panel: Entropy scaling in $YbRh_2(Si_{0.95}Ge_{0.05})_2$ as a function of temperature temperature T and applied field B. Shown is a log-log plot of the entropy S as $b^{-2/3}S$ vs T/b. Right Panel: The electrical resistivity of $YbRh_2(Si_{0.95}Ge_{0.05})_2$ at low temperatures for fields applied perpendicular to the c-axis, showing $\rho(T) = \rho_0 + AT$.

of unshielded moments at a given temperature T. In other words, the entropy follows the strength of the lattice spanning cluster as a function of temperature. Conduction electrons scatter off the fluctuating moments in the lattice spanning cluster and as a consequence, resistivity should be proportional to the strength of the lattice spanning cluster. Ultimately, resistivity then becomes proportional to the entropy S of the system (electrons can also scatter off of phonons, but we will ignore their contribution at low T as the number of phonons goes as T^3). Thus, percolation physics and magnetic clusters naturally account for the low temperature scaling of the resistivity seen in $YbRh_2Si_2$: as long as $S = \gamma T$, then the leading temperature dependence of the resistivity should be linear in temperature.

3.3.3 Super-paramagnetic Response

Similar to the QCP-compounds ($CeRu_2Si_2$ and $Ce(Fe_{0.755}Ru_{0.245})_2Ge_2$) discussed before, we expect to see a super-paramagnetic response in $YbRh_2Si_2$. At the lowest temperatures when isolated clusters are present, these clusters have a super spin which

can align with an external magnetic field. When clusters with the largest super spin align with the external field, they themselves will produce a field which amplifies the external field. This allows for nearby super spins to more strongly react to the external field and thus leads to a rapid growth in the susceptibility of the system (Fig. 3.8). The rapid increase in the system's susceptibility is a super-paramagnetic response (Section 2.3.3)[45]. Both $CeRu_2Si_2$ and $Ce(Fe_{0.755}Ru_{0.245})_2Ge_2$ also display this super-paramagnetic response (Figs. 2.5 amd 2.6), as does $CeRuRhSi_2$ [22]. Considering that this behavior is found in four different samples, it is highly unlikely that any ferromagnetic contamination could dominate the low temperature response of all four systems in an identical way. Therefore, we believe this behavior must be a feature of the system's response, i.e., the super spins of clusters acting as ferromagnetic entities aligning with and amplifying the external field. We therefore take this behavior as strong indication that super spins are indeed present in $YbRh_2Si_2$. We note that in the literature this behavior has been ascribed to ferromagnetic fluctuations at the QCP[65].

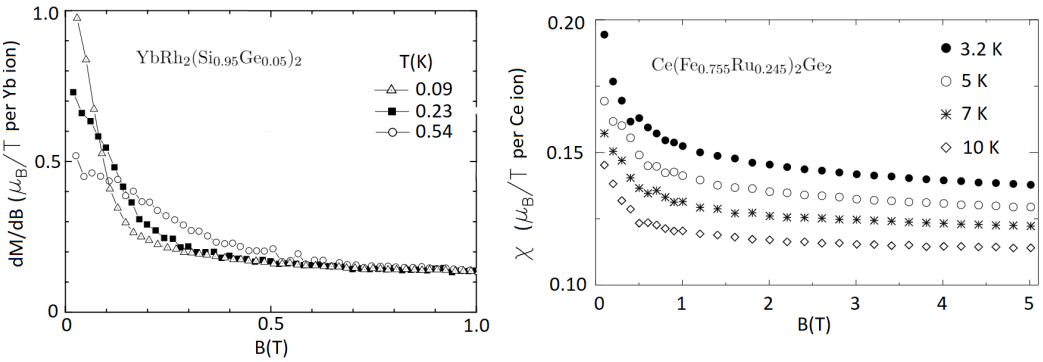

Figure 3.8: Left panel: Adapted from Gegenwart *et al.*[65]. The differential susceptibility dM/dB as a function of magnetic field B for the temperatures indicated in the figure with the field applied perpendicular to the c-axis. Right panel: The susceptibility $\chi = M/B$ for $Ce(Fe_{0.755}Ru_{0.245})_2Ge_2$ as a function of applied field along the easy-axis for the temperatures indicated in the figure.

3.3.4 AC-Susceptibility

Ac-susceptibility measurements performed on $YbRh_2Si_2$ and $YbRh_2(Si_{0.95}Ge_{0.05})_2$ show a globally similar temperature and field dependence (Fig. 3.9) as the data obtained on $CeRu_2Si_2$ (Fig. 2.7). From Fig. 3.9 we see that χ_{ac} becomes field independent for temperatures greater than 2 K while displaying a field and temperature dependent peak (Fig. 3.9). At the lowest temperatures for fields $B > 0.1$ T, we see that χ_{ac} approaches a constant value. We will explain these three observations using our cluster scenario.

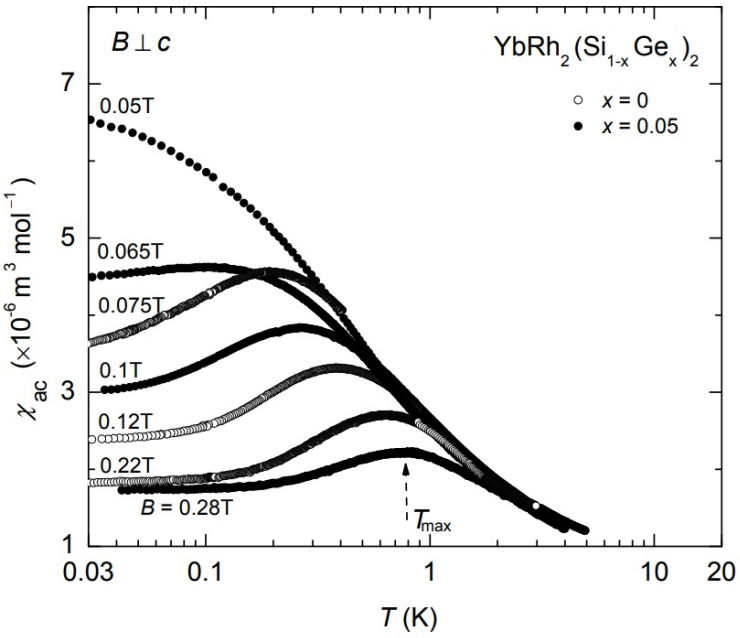

Figure 3.9: Figure adapted from Custers *et al.*[67]. Displayed are the ac-susceptibility for $YbRh_2Si_2$ (open circles) and $YbRh_2(Si_{0.95}Ge_{0.05})_2$ (closed circles). The external field was applied perpendicular to the c-axis.

When $B/T \ll 1$, the specific heat of the response of the system was seen to be dominated by the infinite cluster (Section 3.3.1). The susceptibility of the system is also dominated by the unshielded moments of the infinite cluster. Thus, we expect

the susceptibility to be given by

$$\chi(B \ll T) = \frac{S(T)}{\mathrm{Rln2}}\,\chi_{free}(B,T) \tag{3.1}$$

where $S(T)/\mathrm{Rln2}$ is a measure of the number of unshielded moments left in the infinite cluster, and χ_{free} is the response of an individual moment, uncorrelated with its neighbors. As $\chi_{free}(B,T)$ is independent of B for $B \ll T$, the observed χ_{ac} should be field independent. This is observed at $T > 2$ K in Fig. 3.9[67].

When $B/T \gg 1$, the specific heat of the system was found to be given by the response of the heavy conduction electrons (Section 3.3.1). We expect the susceptibility in this region to consist of two components. First, the heavy electrons contribute their respective temperature independent Pauli susceptibilities (Eq. 1.1). However, due to the dynamic nature of cluster formation in $YbRh_2Si_2$ in combination with the details of ac-susceptibility measurements, there is an additional effect seen in the ac-susceptibility not seen in c_{el}/T. In ac-susceptibility measurements, the sample is placed in an ever present static magnetic field and then a dynamic field probes the sample for changes in magnetization: $\chi_{ac} = \mathrm{d}M/\mathrm{d}B$. Upon cooling, isolated clusters form and order but these clusters are dynamic, they phase in and out of existence. The moment these clusters form, they align with the ever present static field when $B/T \gg 1$. These "freshly" (re)formed clusters will produce a signal in the pick up coil and register in the ac-susceptibility. When these isolated clusters form and disappear dynamically (the cluster froth state) we expect a temperature independent addition to the ac-susceptibility. This together with the Pauli paramagnetic susceptibility results in the temperature independent behavior seen in Fig. 3.9 when $B/T \gg 1$. Interestingly, we would expect χ'' (the dissipative part of the susceptibility) to also

produce a temperature independent level as clusters form and disappear while always aligning with respect to the ever present static field. In other words, the phase of the secondary dynamic probing field has no impact on the clusters which have formed and aligned to the primary field. Thus, we would expect a large out-of-phase component to χ_{ac}, similar to what was reported in $CeRu_2Si_2$ [26]. It is unclear whether such a signal was observed in $YbRh_2Si_2$. We have contacted Jeroen Custers, who reported that a χ'' signal was observed[90] but that it was attributed to electronic pick-up and removed from the study.

From Fig. 3.3, we can see that the lower the magnetic field, the closer the system is to the QCP. Upon lowering the field (Fig. 3.3), more and more moments become shielded and isolated clusters break away from the lattice spanning cluster. The lower the field, the more isolated clusters are present. The super spins of these clusters can align with an external field and contribute to the susceptibility. This was seen in the system's super-paramagnetic response in Section 3.3.3. Thus, lowering the field increases the number of super spins contributing to the susceptibility and is the dominant effect causing the increase in the constant value of χ_{ac} seen with decreasing field (Fig. 3.9) when $B/T \gg 1$. However, the increase in m^* (Eq. 1.1) linked to increased Kondo shielding may also contribute to the increase upon lowering the field observed in χ_{ac}.

Similar to the specific heat data, the ac-susceptibility curves show a maximum as a function of temperature for fields $B > 0.07$ T (denoted T_{max} in Fig. 3.9). This peak position does not coincide with the peak positions in c_{el}/T. This is shown in Fig. 3.3 where it can be seen that (for a given field), the peak in the ac-susceptibility

occurs at a higher temperature than the peak in c_{el}/T. We believe that our cluster scenario also naturally explains this observation without having to resort to more exotic explanations[67].

The peak position in c_{el}/T reflects the highest rate of entropy loss, or the highest rate of cluster formation. However, depending on the ratio of B/T, the super spin of these clusters might be "frozen"(aligned with the primary field field) and not respond to the secondary ac-field. We illustrate this by following two trajectories in the phase diagram. For the first trajectory, imagine cooling the system down in a constant field, such as $B = 0.2$ T in Fig. 3.1. Upon cooling, more and more clusters with super spins appear, shedding their entropy and reacting to the ac-field. However, upon cooling more (increasing B/T), these clusters as well as any newly minted clusters become more and more unresponsive to the ac-field as the primary field lines up the super spins. Thus, we expect the ac-susceptibility signal to drop, even when the maximum rate of cluster formation has not been achieved yet. Upon cooling even further, cluster formation still increases down to the field cut-off (Fig. 3.6), explaining why the peak in c_{el}/T occurs at a lower temperature.

Lowering the field at constant temperature produces the same insights, such as reducing the field at a constant temperature of 0.3 K (Fig. 3.1). At a fixed $T > T_N$, the potential demise of the infinite cluster is cut off by the finite temperature. Starting out at high field values and going down, we see more and more clusters form, down to the cut-off value determined by the finite temperature. This produces a peak in c_{el}/T, reflecting the maximum possible rate of cluster formation. However, these clusters do not react much to the secondary ac-field for reason already discussed. It

is not until the field is lowered enough so that the cluster spins "unfreeze" that we see the clusters show up un ac-susceptibility measurements. Thus, the ac-susceptibility peaks at a lower field than the specific heat.

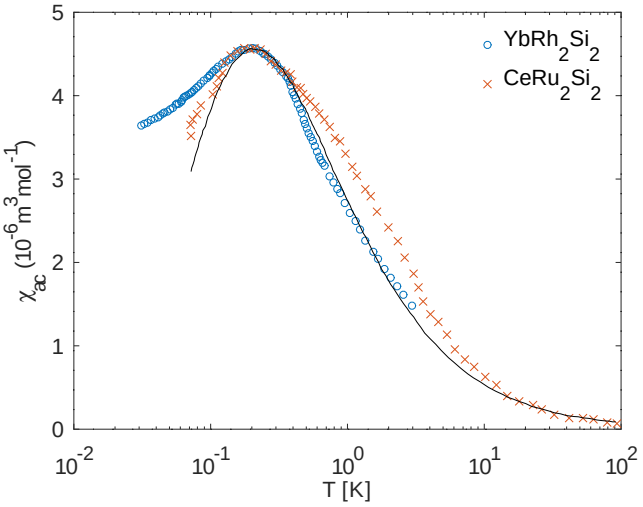

Figure 3.10: Ac susceptibility of $YbRh_2Si_2$ [67] (blue open circles) and $CeRu_2Si_2$ [26] (orange crosses) at fields of 0.075 T and 0.2 mT, respectively. The solid line is the result of a computer simulation discussed in Chapter 2, where the susceptibility of each isolated cluster was modeled using Eq. 2.6. As the argument of the function in this equation depends on $\mu H/T$ (with μ the moment of a magnetic ion), we also applied a horizontal scale factor. The expected scale factor using the free moment value of Yb and Ce ions as well as the ratio of field values used in each experiment, is given by $s_x = B_{Yb} \times \mu_{Yb}/B_{Ce} \times \mu_{Ce} = (1.91 \times 0.075)/(0.2 \times 1.21) = 0.59$. However we have chosen a value of s_x to be 0.55 for best visual agreement and corresponding to an uncompensated moment value for of $1.8\mu_B$ per Yb ion. The value of $1.91\mu_B$ per Yb ion us based on the Wilson ratio, see text.

While the $YbRh_2Si_2$ data are more difficult to interpret than $CeRu_2Si_2$ data we discussed in Chapter 2, a direct comparison between the two systems reveals many similarities. We compare the ac-susceptibility in Fig. 3.10 for $YbRh_2Si_2$ at a field of $B = 0.075$ T to the ac susceptibility for $CeRu_2Si_2$ shown in Section 2.3.4. For this direct comparison, an overall scale factor has been applied in both directions to accommodate for the arbitrary units used in $CeRu_2Si_2$ by Takahashi *et al.*[26] as well as to account for the difference in magnetic field and moment values between the two experiments and systems, respectively. The expected scale factor along the

x-axis s_x can be calculated using the free moment value of Yb and Ce ions as well as the ratio of field values used in each experiment as $s_x = B_{Yb} \times \mu_{Yb}/B_{Ce} \times \mu_{Ce} = (1.91 \times 0.075)/(0.2 \times 1.21) = 0.59$, very close to the value of s_x= 0.55 that yields the best visual agreement (corresponding to a moment value for a free Yb ion of $1.8\mu_B$). The value of $\mu_{Yb} = 1.91\mu_B$ follows from the observed Wilson rations of $R_W = 17.5$, yielding $\mu_{Yb} = 1.91\mu_B$ using Eq. 2.7. Thus, using a straightforward scale factor, we observe a very similar response in both systems, with both responses close to the expected response of a collection of isolated clusters. Based on this, we now show that this collection of super spins can also quantitatively reproduce the measured susceptibility of $YbRh_2Si_2$ and $YbRh_2(Si_{0.95}Ge_{0.05})_2$.

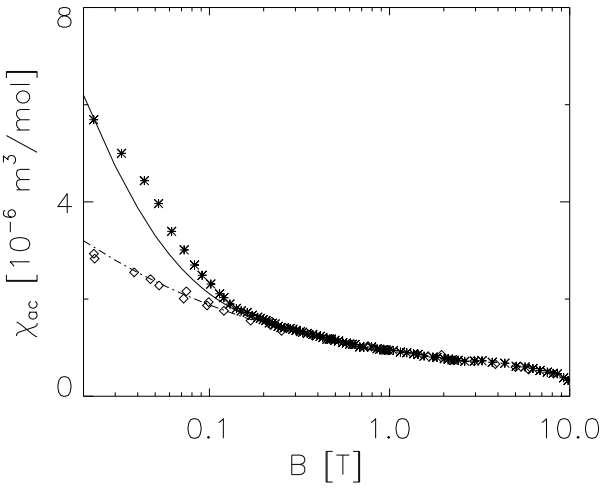

Figure 3.11: Extrapolated $T \to 0$ value as a function of field for both χ_{ac} (stars) and c_{el}/T (diamonds and scaled to coincide with χ_{ac} at high fields). Using protected percolation simulations to model the super spin distribution at the percolation threshold, we can then model the magnetic response of such a distribution. Adding that response in addition to (on top off) the response of the c_{el}/T produces the solid black curve (where we have used an uncompensated moment value of $\mu = 1.91\mu_B$). Figure adapted from Gegenwart *et al.*[69].

The low temperature behavior of both χ_{ac} and c_{el}/T is shown in Fig. 3.11. This figure is adapted from Gegenwart *et al.*[69] and displays the extrapolated $T \to 0$ values as a function of field for both χ_{ac} and c_{el}/T. We have argued, qualitatively, that

the low-T behavior reflects that of the conduction electrons in both the specific heat and ac-susceptibility measurements. However, the ac-susceptibility should also reflect how well super spins respond to a secondary ac-field, provided the super spins are not "frozen". The χ_{ac} data shown in Fig. 3.11 were actually taken at $T = 0.09$ K; as a result, the super spins remain frozen for fields $B > 0.2$ T and the two curves (specific heat and ac-susceptibility) track each other. Once the super spins "unfreeze", we see their response in the susceptibility. The solid line in Fig. 3.11 quantifies this. We have taken the cluster distribution at the percolation threshold, assigned a moment value of $1.91\mu_B$ to each unshielded Yb ion and calculated the susceptibility of the collection of clusters at $T = 0.09$ K as a function of field, using Eq. 2.8. We then added this contribution on top of the contribution of the conduction electrons (given by the $T \to 0$ values of the c_{el}/T curve) to arrive at the solid line. The solid line tracks the susceptibility data quite well. This is remarkable as the susceptibility data were reported in absolute units so that our comparison is free from any scale factors.

3.4 Conclusion

In summary, we have shown that our cluster scenario accounts for all observed features in the specific heat and susceptibility, and even comes with a natural explanation for the linear T-independence of the resistivity. In the literature, this system has been described as being close to an AF-QCP, but with strong ferromagnetic fluctuations. We view these ferromagnetic fluctuations as super-paramagnetic behavior. The smallness of the loss in entropy and ordered moment has been ascribed (in the literature) to the weakness of the ordering while at the same time viewing the QCP as the point where the large moments re-appear. We proposed a much simpler explana-

tion with unshielded moments that are very similar throughout the phase diagram. We attributed the smallness of the entropy loss to the fact that the only remaining entropy that could be removed being the orientation of the super spins. In our scenario, the smallness of the ordered moment reflects that more moments in clusters are compensated by their neighbors, not a small moment by itself.

We also differ in whether this compound displays multiple quantum critical[67] points as opposed to just one. We view the maxima observed in the specific heat and susceptibility curves as being related to whether clusters are "frozen" in ($B/T \gg 1$) or free to respond to a small field ($B/T \ll 1$), Finally, a direct comparison between the cluster distribution at the QCP and the measured susceptibility and specific heat data shows that our cluster model yields the correct predictions, free from any adjustable parameters.

Chapter 4

Connection to the Pairing Mechanism in High-T_c Cuprate Superconductors

4.1 Introduction

In this chapter we make the connection between the findings concerning the influence of small ionic displacements on the response of strongly correlated quantum critical systems with the pairing mechanism in the cuprate superconductors, another family of strongly correlated electron systems. While this chapter is speculative, we argue that by considering the effects of small ionic displacements introduced by hole doping into the parent compounds of the cuprates, we naturally arrive at a mechanism for Cooper pairs to form, as well as other experimentally observed features such as a striped phase.

This chapter is subdivided as follows. We first give a brief overview of the general properties of the cuprate superconductors as well as of some salient details of the response of these systems that all layered cuprates have in common. We pay special attention to the so-called striped phase and the hourglass dispersion. Next, we show how the introduction of holes in the CuO_2 planes leads to small distortions that

favor the formation of singlet Cooper pairs bound together by the anti-ferromagnetic pairing of two intermediate copper atoms, driven both by an unscreened Coulomb interaction as well as by electron-phonon coupling involving half-breathing modes.

Next, we show that a reasonable description of a dressed hole state leads to the formation of a striped phase whose incommensurate ordering wave vector saturates at doping levels above p = 1/8. We apply linear spin wave theory to the emerging striped phase and observe an hourglass dispersion for the magnetic excitations. However, the interpretation of this dispersion, as well as the role of AF stripes in the underdoped superconducting phase departs from interpretations in the literature. We finish with a comparison to the superfuid state of helium-4 and speculate that the superconducting transition temperature is not linked to the breakup of Cooper pairs but rather to a low energy gap that is likely associated with the spin anisotropy that forces the copper spins to be confined to the Cu-O planes.

We define several acronyms commonly used in high cuprate superconductors to refer to the various cuprates: $La_{2-x}Ba_xCuO_4$, known as LBCO; $La_{2-x}Sr_xCuO_4$, known as LSCO; $YBa_2Cu_3O_{6+\delta}$, known as YBCO; $Bi_2Sr2CaCu_2O_{6+\delta}$, known as BISCO.

4.2 The Phase Diagram of the cuprates, Incommensurate Order and hourglass Dispersion

In this section, we review what has emerged over 35 years as universal features between all the superconducting cuprates[58]. We emphasize the phase diagram as a function of doping the AF-parent compound with holes, the emergence of incommensurate magnetic order, and the magnetic excitation spectra in the superconducting phase. We will leave out many details as to how this information was acquired over the past

decades, as well as features that are not necessarily universal between the cuprates. However, we will use such details in later sections when the model makes predictions about certain aspects of the low temperature response.

The parent compounds of the high-T_c superconductors are anti-ferromagnetic (AF) systems characterized by high transition Néel-temperatures T_N[71]. Below T_N, the spin-1/2 Cu ions that are located in the square lattice that form the CuO_2 planes order in an AF-pattern[58]. The Cu-Cu interaction that is responsible for this ordering is the superexchange mechanism of the Cu-O-Cu bond. The singly occupied $3d_{x^2-y^2}$ Cu-orbitals overlap with the neighboring $2p_x$ and $2p_y$ O-orbitals, resulting in a net AF superexchange interaction J between neighboring Cu-ions[72]. The value of J is typically between 100 and 150 meV[73]. This mechanism is illustrated in Fig. 4.1. All cuprates have the CuO_2 layers, either as single layers, or as bi-layers, 3-layers or 4-layers. These layers are separated by non-magnetic layers along the c-axis. The Cu-O layers are only weakly coupled (magnetically) along this c-axis[86].

Chemical doping in the non-magnetic layers removes electrons from the Cu-O planes, a process referred to as hole doping. It is observed that for as little as one hole doped for every 50 Cu-ions that the AF order collapses and disappears[58]. This leaves a phase rich in magnetic Cu-ions, but without long range order. Numerous experiments have shown that the holes are predominantly located on the oxygens [74]. Thus, to good approximation, we can treat the undoped systems as consisting of a square lattice of Cu^{2+}-ions and O^{2-}-ions. With doping, some of the oxygen ions become O^-. Copper ions that are linked through such an O^--ion no longer align anti-ferromagnetically. In fact, there now is a tendency to line up ferromagnetically (FM).

This is illustrated in Fig. 4.1. Both AF and FM alignment can be viewed as direct consequences of lowering the energy of a state through delocalization of electrons, a process also referred to as 'hopping'[75].

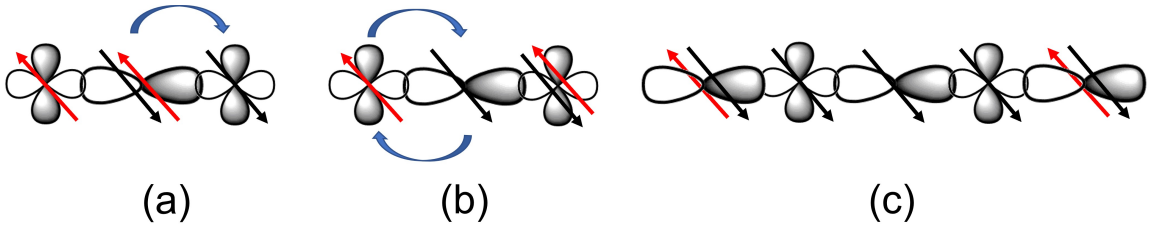

Figure 4.1: In the cuprates, there is an overlap between the half-filled copper $d_{x^2-y^2}$ orbitals and the oxygen $2p$ orbitals as shown in the left panel. The localized electrons can lower their kinetic energy through virtual hopping processes such as the one shown in the middle panel. This process requires the spins of the unpaired Cu-electrons to be aligned anti-parallel. Introduction of a hole in the system that predominantly resides on the oxygen results in a parallel spin alignment of the Cu-electrons as shown in the right panel. In this sketch, all electrons (red arrows) that reside on dually occupied sites can hop to their neighbors without restriction.

Once a doping level p ≈ 0.05 has been reached, the system becomes superconducting. Upon increased doping, T_c rises and peaks at a doping level of p $\approx 1/6$, then falls off again and the superconducting phase disappears at p < 0.3[76]. In addition, the development of T_c with p can show a kink at p $= 1/8$ (LSCO), or even a severe reduction (LBCO)[77]. Various other energy scales (besides $k_B T_c$) have been identified, such as the pseudo gap energy scale observed at less than optimal doping for temperatures above T_c, and a spin gap energy scale for doping levels near optimal doping and higher[58].

Mapping out the magnetic excitations as a function of doping by means of neutron scattering experiments has revealed that the spin-waves present in the AF phase cast their shadow into the superconducting phase in the sense that magnetic excitations can still be observed, albeit not as well defined. Moreover, incommensurate (IC) mag-

netic Bragg peaks with accompanying spin-waves have been observed below optimal doping levels, transitioning into IC fluctuations for higher doping levels[76]. The IC fluctuations exhibit an energy gap, referred to as the spin gap. The size of the spin gap increases upon increased doping. The incommensurate position of these peaks are captured by the parameter δ: Bragg peaks are observed [near the AF $(1/2, 1/2)$ Bragg peaks of the parent compound] at $(1/2, 1/2 \pm \delta)$ and $(1/2 \pm \delta, 1/2)$. At least, this is the case for moderate doping levels such as p = 1/8[78]. For much lower doping levels, the peaks occur in a pattern rotated by 45 degrees, either indicating diagonal order, or a staircase type of structure[58]. We ignore this region (p < 0.06) in this chapter.

The appearance of these IC lattice peaks is accompanied by the appearance of satellite peaks around nuclear Bragg peaks with indices $(h \pm 2\delta, k)$ and $(h, k \pm 2\delta)$. Thus, we observe the formation of larger unit cells with size $1/\delta$ and $1/2\delta$[58]. It is the appearance of these sets of peaks that have led to the discovery of the striped phase[79]. We show the cartoon for this phase for p = 1/8 in Fig. 4.2. In this phase, we have uni-directional stripes of AF-ordered Cu-ions spaced $1/2\delta$ unit cells apart. The AF stripes are in anti-phase, so it takes $1/\delta$ unit cells for the pattern to repeat itself, giving rise to the observed peaks at $(1/2 \pm \delta, 1/2)$. In addition, the holes have accumulated in between the stripes. The positive charges of these holes lead to small lattice distortions every $1/2\delta$ unit cells, which gives rise to satellite peaks $(h \pm 2\delta, k)$ in neutron and X-ray scattering experiments. Thus, both spin order (magnetic stripes) and charge order (in between the magnetic stripes) is observed[80].

The composition p = 1/8 has been studied most extensively, but other composi-

tions reveal a similar appearance of satellite peaks. For p $< 1/8$, we observe that δ = p [81]. In other words, the number of holes per Cu-ion directly scales (inversely) with the separation between stripes. For larger doping levels, it has been observed that δ saturates at 1/8 [82]. We will see in the following paragraphs that our model naturally accommodates this saturation. Note that because of the symmetry of the square lattice, the $h-$ and k-directions are (almost) equivalent.

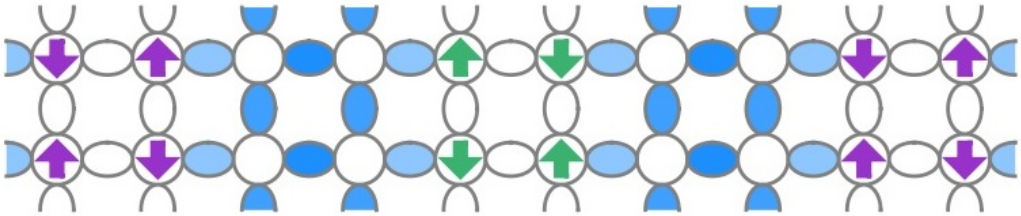

Figure 4.2: Figure adapted from Tranquada *et al.*[58]. The appearance of superlattice peaks at $(1/2 \pm \delta, 1/2)$ and at $(1/2 \pm \delta/2, 1/2)$ leads to the graphic shown here, where we have vertical stripes of alternating charge accumulation and AFM-correlated Cu-moments. The AFM-strips are in anti-phase, leading to a further expansion of the magnetic unit cell (8×2 nuclear units in this sketch).

When the energy cost of the magnetic excitations is plotted versus momentum transfer in the Cu-O plane, then an hourglass shape is observed that is common between the three most studies families of superconductors: LSCO, YBCO, and BISCO. We reproduce this pattern in Fig. 4.3[59]. We observe magnetic excitations dispersing from the incommensurate magnetic superlattice peaks inwards towards $(1/2, 1/2)$, the zone center for the AF-structure of the undoped parent compound. Once at the 'old' zone center, new branches are seen to disperse outward with energies very similar to those in the undoped compounds[58]. Also note that there do not appear to be any branches dispersing outward from the IC-points. For dopings higher than p = 1/8, the response at the IC peaks at the lowest energies (including $E = 0$, the static pattern) disappears; this is referred to as the opening up of a spin gap $E < E_{SG}$, that

is, the dispersion follows the same curvature but no longer has intensity below $E < E_{SG}$[83].

The intensity of the response at $(1/2, 1/2)$ at the middle of the hourglass varies from compound to compound. The peak is especially intense in the bi-layered compound YBCO, and goes under the moniker of 'resonance peak'[58]. On cooling the system down through the superconducting transition temperature, this peak becomes very pronounced, and appears to be (almost) localized in both energy and momentum space[84].

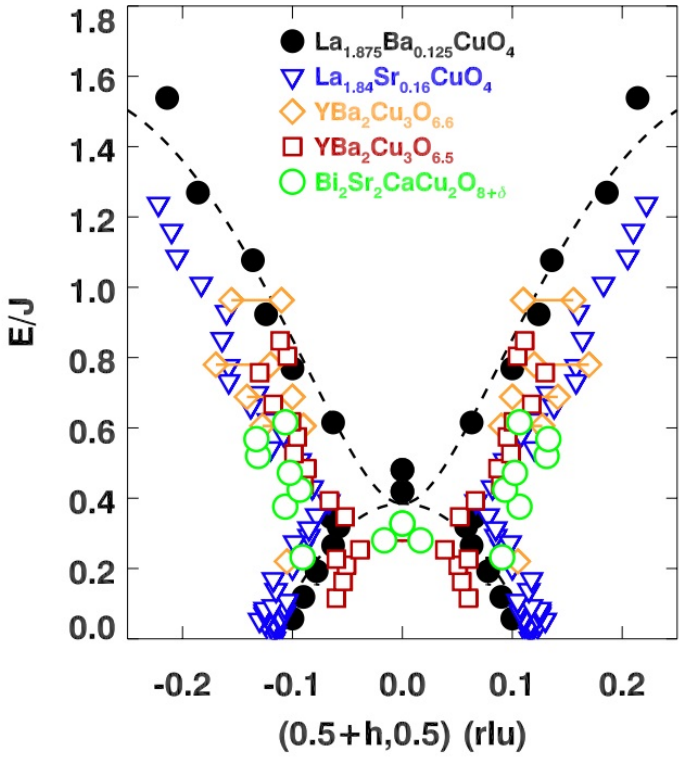

Figure 4.3: Figure reproduced from Fujita *et al.*[59] Shown are the measured excitation energies for two single layer compounds (LSCO and LBSO) and two bi-layered compounds (YBCO and BISCO) as a function of in-plane momentum transfer. The symbols are explained in the legend. When scaling the measured energies with the superexchange energy J from the respective parent compounds, the data collapse onto a single hourglass-like shape. The center point at $(1/2, 1/2)$ is referred to as E_{cross}, and the dashed curves are guides to the eye. Note that not every composition corresponds to the exact same doping level, and that the horizontal axis covers both $(1/2 + h, 1/2)$ as well as $(1/2, 1/2 + h)$. The point $(1/2, 1/2)$ is the AF-zone center of the parent compound.

In summary, much is now known about the magnetic dynamics and about what the various families of cuprates have in common. Whereas early on it was thought that AF order would be destructive to superconductivity as the movement of holes through the lattice would involve spin flipping of the Cu-moments, the views have evolved in that the separation of charge and spin order are now seen as being intimately linked to the mechanism behind Cooper pairing. We refer to two review articles by John Tranquada for further details cementing this new outlook[58, 86]. In the following sections we make the case for how the small lattice distortions accompanying doping can lead to the appearance of the striped phase, the hourglass dispersion, as well as the dependence of δ on doping p.

4.3 Cluster Formation upon Doping through Coulomb Repulsion and Electron-Phonon Coupling

At the heart of all magnetic interactions in the cuprates is the superexchange interaction of the Cu-O-Cu pathway. Given that an exchange interaction is determined by the overlap of atomic orbitals, and given that this overlap depends sensitively on inter-ionic distances, we can expect large effects on the strength of the magnetic interaction when we have small changes in interatomic separations. Thus, we have a similar problem as to what we encountered in the Kondo materials. In here, we discuss how the introduction of holes into the CuO_2 planes can locally enhance the AF-pairing of neighboring Cu-ions, leading to the formation of regions with increased AF ordering tendencies, interspersed with regions of subdued ordering tendencies. We argue that this pattern is enhanced by electron-phonon coupling involving breathing and half-breathing modes[52].

We have seen in the discussion on $CeRu_2Si_2$ and $YbRh_2Si_2$ that the dynamic changes in inter-ionic separations can lead to the appearance of spontaneous magnetic clusters that end up dominating the response at low temperatures. So a natural question to ask is: can something similar take place in the cuprates, another system where the magnetic moments strongly interact with each other and are on the cusp of long range order? The answer is likely yes, and the effect is likely even enhanced by the unscreened Coulomb repulsion between holes and Cu-ions.

The phonon modes of particular interest to this scenario are the breathing and half-breathing modes. These optical modes correspond to ion displacements in the Cu-O plane, bringing groups of ions closer together (breathing), or strips of ions closer together (half breathing)[52]. We show cartoons for these motions in Fig. 4.4. For instance, the half-breathing mode for $(0, 0, 0.25, 0)$ corresponds to a similar striped pattern as the charge ordering observed for p = 1/8.[52] Most interestingly, it is the energy of the half-breathing mode at $(0, 0.25, 0)$ that shows the most changes upon cooling the system down through the superconducting transition. We reproduce a figure from Pinchovius's review in Fig. 4.5 illustrating this phonon anomaly[52].

We now focus on the half-breathing mode for $(0, 0.25, 0)$ for multiple reasons. First, the renormalization of the phonon energy is strongest at this wave vector, corresponding to a wavelength of $\lambda = 4$ times the in-plane size of the nuclear unit cell. Second, the phonon linewidth is largest at this wavevector, indicating a coupling of this mode to other processes in the system. Third, it is known that the incommensurate peak positions δ saturate for doping levels $p > 1/8$, so this particular stripe pattern is relevant to all doping concentrations[82].

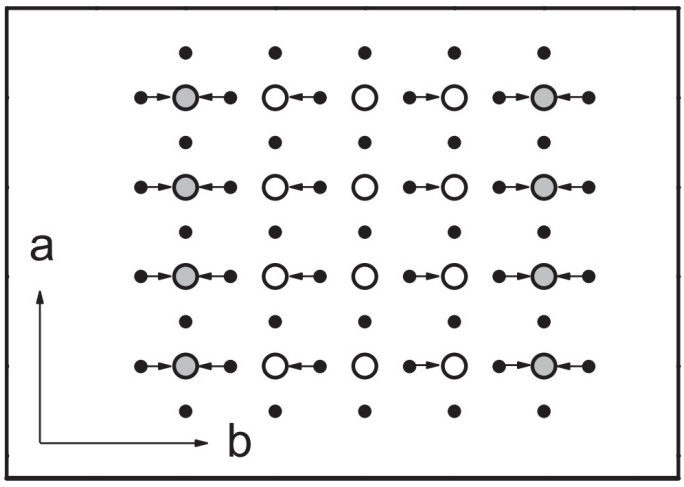

Figure 4.4: Figure reproduced from Pintschovius *et al.*[52] showing the displacement pattern in interatomic distances due to anomalous phonons with wave vector $(0, 0.25, 0)$. Displacements shown are only in the CuO_2 planes which are the dominant displacements. Grey circles indicate that the displacements favor dynamic charge accumulation on every fourth row of copper atoms.

When Cu ions are brought closer together, it enhances the superexchange interaction between them, thereby enhancing the ordering tendencies of the Cu moments within these regions. When the ions move further apart, the superexchange is diminished, reducing the AF correlations in those regions. Thus, this mode appears to be conducive to the formation of the p = 1/8 stripe pattern shown in Fig. 4.2[58]. Should the stripe pattern be connected to the superconducting state, then this naturally explains the observed isotope effect[52]. Electron-phonon coupling is present (and quite strong) in the cuprates, although the coupling is not strong enough to explain the high transition temperatures according to BCS theory[87]. However, the coupling could induce stripes to form, and provided that stripes play a role in the superconducting dynamics, then the coupling sets the stage for the superconducting state, without providing the energy scale for the Cooper pairs.

Could the phonon induced formation of stripes lead to the appearance of isolated

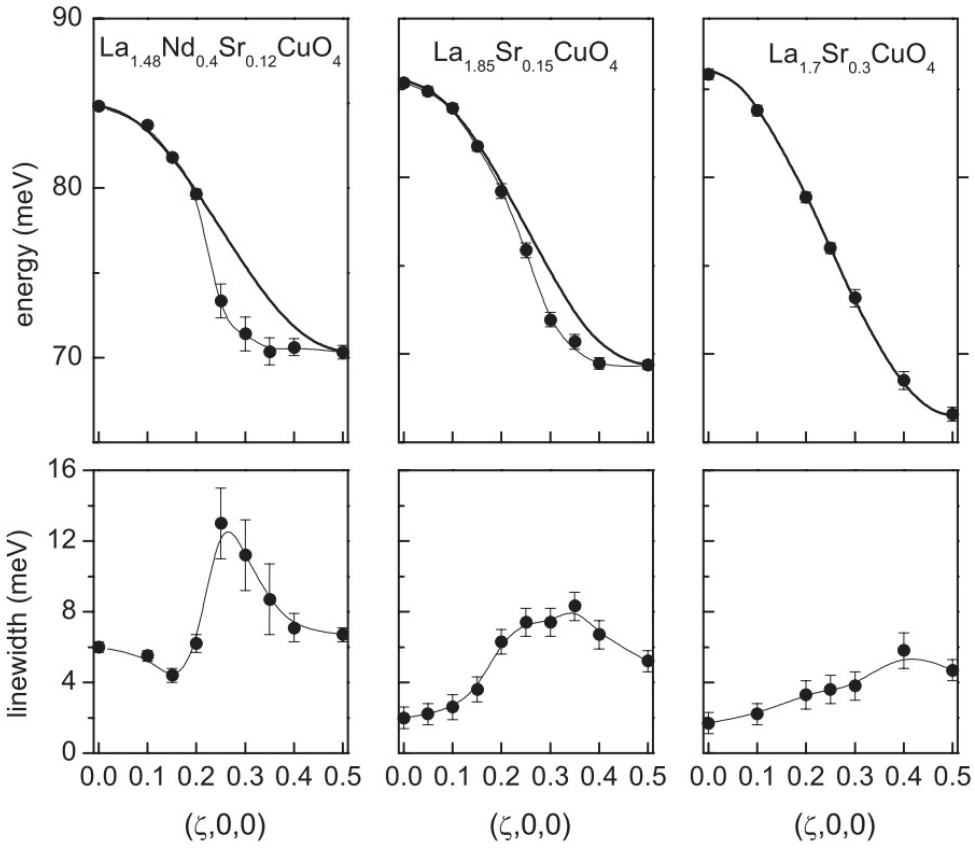

Figure 4.5: Figure reproduced from Pintschovius *et al.*[52]. Top Panel: The striped phase dispersion of Cu-O bond-stretching vibrations in $La_{1.48}Nd_{0.4}Sr_{0.12}CuO_4$ (left), $La_{1.85}Sr_{0.15}CuO_4$ (middle), and $La_{1.7}Sr_{0.3}CuO_4$ (right). Bottom Panel: The phonon linewidths (resolution-corrected) for the phonons shown above. Thin solid lines are guides to the eye while thick solid lines are cosine-functions.

magnetic clusters, and potentially the appearance of super spins as it does in stoichiometric quantum critical systems? The answer is that we do not expect any super spins to appear, but the regions of strong coupling separated by regions of weak coupling might have some minor influence on the magnetic response as probed by neutron scattering. What turns out to be of the utmost importance though is that this segregation of strongly and weakly coupled regions sets the stage for the formation of Cooper pairs. We discuss the latter in the next section, whereas the former (the absence of super spins) is easy to visualize: should magnetic order ensue on the

highly correlated magnetic stripes, then these stripes contain equal amounts of 'up' and 'down' Cu-moments and the super spin would be zero.

As an aside, the appearance of super spins could potentially have led to the formation of Cooper pairs. One electron would emit a phonon, creating a magnetically correlated volume with a super spin. This super spin could interact with the first electron's spin, as well as with the spin of a second electron, creating a magnetically bound Cooper pair. Phonons that could do this would need to have a periodicity different from $2a$, with a the lattice spacing. As far as we can tell, there are no phonons that show strong anomalous behavior that meet this criterion, and we do not pursue the super spin avenue further in this dissertation.

The formation of spin-stripes favors the accumulation of the holes in between the stripes. The energy of a hole depends on how mobile it is: the more mobile, the lower its kinetic energy. The mobility of holes in the AF environment is restricted as hopping along the direction of the stripes needs to be accompanied by spin flips of the Cu moments. When these moments are aligned with their neighbors, holes can only hope diagonally, directly from oxygen to oxygen (hopping between the $2p_x$ and $2p_y$ orbitals). In between the magnetic stripes, however, it is much easier for the holes to hop, thereby reducing their energy. As such, in the presence of static stripes, holes tend to accumulate in between the magnetically ordered stripes, resulting in charge order[80]. Even in the case of dynamic stripes (stripes that appear and disappear), diagonal hopping would see the holes leave the magnetic stripes and accumulate in between them.

When the holes are located predominantly in between the AF-stripes, then the

Coulomb interaction amplifies what gave rise to the formation of highly correlated magnetic stripes in the first place. The accumulation of positive charge in between the stripes pushes the Cu-ions within the stripes even closer together, further enhancing the superexchange mechanism. Thus, the system has a natural tendency towards charge separation, independent of whether the magnetic order was initiated by phonons, or not. In the next section we discuss how the enhanced superexchange interaction can lead to Cooper pairing.

4.4 The Emergence of a Striped Phase and Cooper Pairing

Decades of experimental work has shown that the cuprates have a tendency to form uni-directional stripes of AF correlations, interspersed by regions rich in holes[58]. We show that oxygen holes, in the form of quasiparticles where the hole is spread out over multiple sites, favors the formation of AF-stripes with neighboring stripes in anti-phase. Moreover, for $p < 1/8$, this results in Cooper pairs bonded across the stripes, while for $p > 1/8$ the Cooper pairs are likely still bonded across the stripes but could potentially be restricted to the hole-rich regions. This scenario naturally explains why the periodicity of the AF stripes cannot be less than 8 unit cells (of the nuclear lattice).

While the observation of the stripe pattern through the observation of incommensurate lattice peaks led to the stripe pattern shown in Fig. 4.2, it is not immediately clear what the reason could be for the magnetic stripes to be in anti-phase[58]. It has been proposed that Cooper pairs form within the charge stripes, and that the overall wave function of the superfluid phase is such that its amplitude is maximum

on the charge stripes, and minimum on the magnetic stripes. This pattern goes under the name of Pair Density Wave (PDW) and is sketched in Fig. 4.6[58, 88]. However, since the amplitude of the PDW is small by (construction) on the magnetic stripes, it is unclear why this pattern would favor alternating AF stripes, rather than stripes with the same, or with random relative phases. In addition, it would not explain why the separation between stripes saturates at distances 4 unit cells apart. We offer a different explanation, resulting in Cooper pairs that bond across AF stripes rather than in between AF stripes.

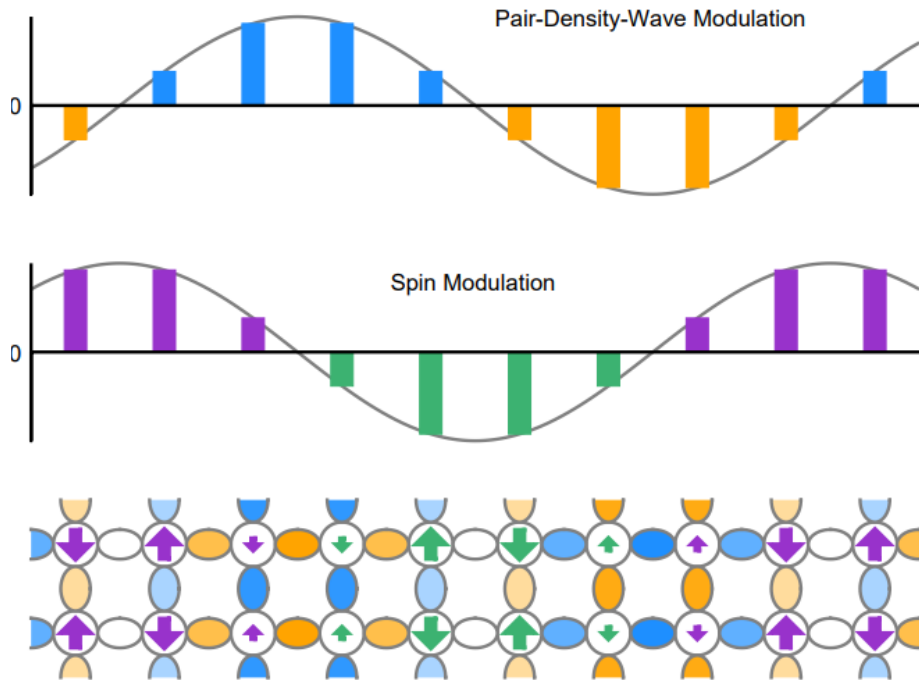

Figure 4.6: The proposed PDW wave function and spin density wave (SDW)[58, 88]. The PDW (top panel) has small amplitude on the AF spin stripes (bottom panel) where the SDW (middle panel) has a large amplitude. Thus, Cooper pairs avoid the AF-stripes, remaining localized in between the stripes. Figure reproduced from Tranquada *et al.*[58].

When a hole is doped into the Cu-O plane, it is known that it mostly resides on the $2p_x$ and $2p_y$ oxygen orbitals[74]. Should this hole not be mobile, then its zero-point energy would be large. This can be estimated very roughly using Heisenberg's

uncertainty principle: $\Delta x \Delta \mathrm{p} > \hbar/2$. Using $a/2$ for the size of the oxygen orbital, we can estimate the zero-point energy to be $(\Delta p)^2/2m > 1$ eV. Should the hole be allowed to hop from site to site (Δx increases), then this energy cost of placing a hole on the oxygen is rapidly reduced. Note that using Heisenberg's uncertainty relation gives us an idea of the energy scale involved, but it also holds for the proper kinetic energy term in the Hamiltonian: the energy scales inversely squared to the gradient of the wave function. We can also readily estimate the energy cost of Coulomb repulsion. Taking the radius of Cu^{2+} to be 73 pm, the Coulomb repulsion between two electrons in the same Cu$d_{x^2-y^2}$ orbital is 10 eV, and the Coulomb repulsion between 2 holes a distance $2a$ apart is 2 eV. These numbers illustrate that these energy scales, even in the presence of some Coulomb screening, are much larger than the energy scale J $\sim$ 0.1 eV associated with the superexchange interaction between two copper moments. This is the reason that once holes are introduced, their mobility quickly destroys AF order[58].

In Fig. 4.7 we sketch our proposal for a somewhat delocalized hole located on the oxygen p-orbitals. We have opted for a cross configuration to respect the square symmetry of the lattice while at the same time not making the delocalization too expansive as Coulomb repulsion between holes would make this unphysical in the first place. In order for this hole to be delocalized in the configuration, all the Cu-moments need to be aligned ferromagnetically, with the missing electron (the hole) having the opposite spin. Note that in the sketch the 'up'-spin electrons of the oxygen (black arrows) are free to wander, greatly reducing their kinetic energy. Keeping the central Cu-moment AF-aligned would only result in the mobility of a single electron.

This also serves as a further illustration as to how quickly AF-order will be destroyed upon hole doping[58].

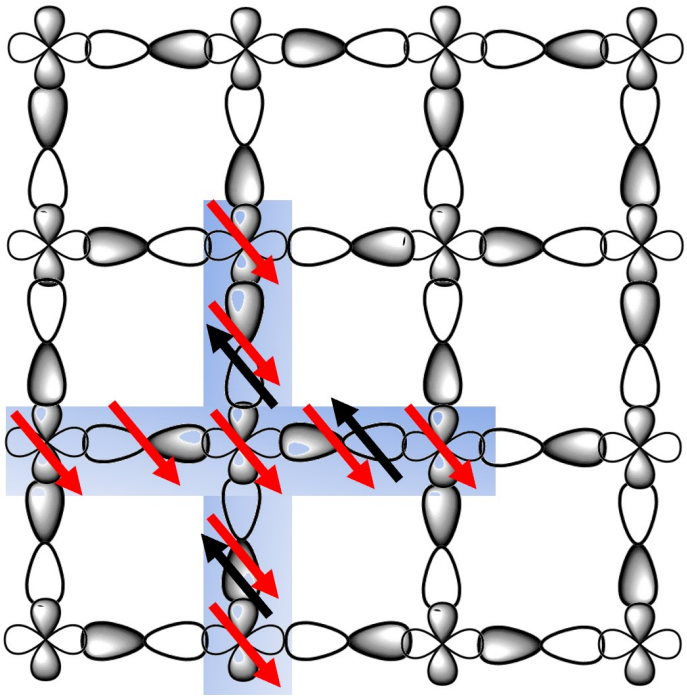

Figure 4.7: Sketch of a single layer of the Cu-O planes in layered cuprate superconductors. Shaded in blue we sketch a delocalized hole (a missing spin) located on an oxygen p-orbital. Note that in the sketch the 'up'-spin electrons of the oxygen (black arrows) are free to wander, greatly reducing their kinetic energy. Down spins are shown as red arrows.

Next, we spread out the holes in the Cu-O planes. We do this for a concentration of p = 1/8, or one hole per 8 copper ions and sketch the situation in panel a) of Fig. 4.8. As can be seen, the holes are at roughly equal distance, minimizing their Coulomb repulsion. Next we have to figure out whether there are preferred spin directions for the Cu-moments associated with this arrangement. It is highly likely that the two Cu-moments situated between two holes in the horizontal direction will align anti-ferromagnetically. The two positive ions have been pushed together more closely through the effective repulsive force between a Cu-ion and a hole, enhancing the superexchange. This alignment reduces the energy of the state on the order of J,

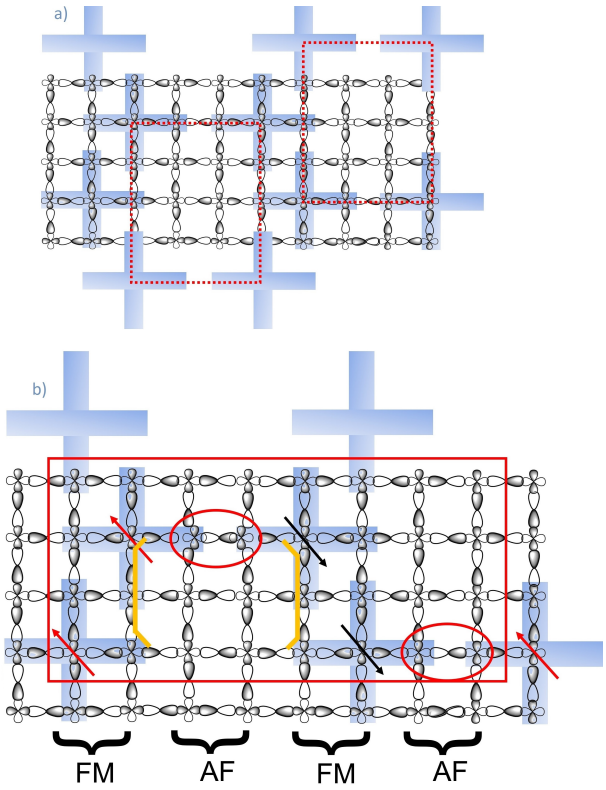

Figure 4.8: Top Panel a): Sketch of a single layer of the Cu-O planes in layered cuprate superconductors. Spreading out of delocalized holes (missing spins) is shown at a concentration of one hole per 8 copper ions (p =1/8). The holes are located in between AF-stripes roughly equal distances apart, minimizing Coulomb repulsion. Bottom Panel b): Sketch of a single layer of the Cu-O planes in layered cuprate superconductors showing FM alignment in between AF-stripes. Hole mobility is greatly increased and now the hole can 'hop' in the vertical direction (the orange line). The two Cu-moments that have been forced closer together are shown as red circles, acting as the glue that binds the Cooper pairs.

about $0.1 - 0.2$ eV. In other words, two holes situated as sketched in panel a) reduces their energy, resulting in an effective attraction (pairing) between the two holes of the order J. Also note that the AF pairing probably forces the overall spin alignment of the Cu-spins that make the hole, but it definitely forces the spin direction of the hole. Since the Cu-moments between the holes are oppositely aligned, the spins of the holes must also be oppositely aligned. In other words, we get a singlet pair of holes, bound together by an energy scale of J.

Before we continue, we remark that the strength of the interaction that favors FM

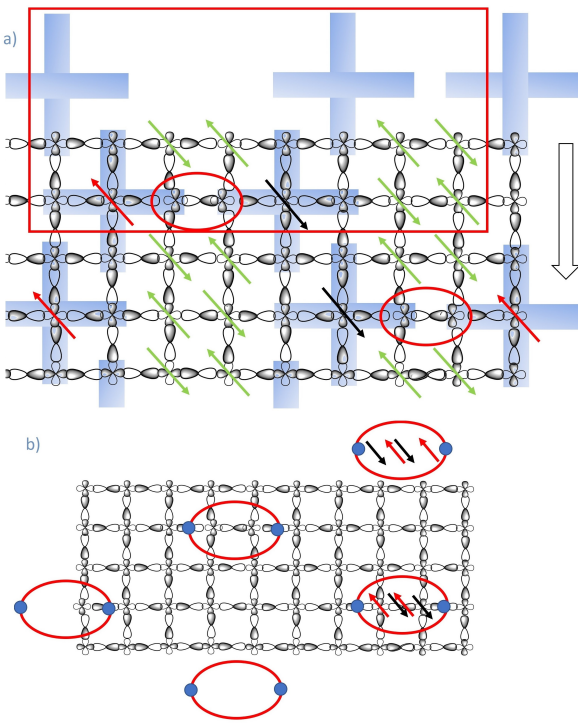

Figure 4.9: Top Panel a): Sketch of a single layer of the Cu-O planes in layered cuprate superconductors after a hole has hopped vertically several times. Antiferromagnetic arrangement between Cu moments in the vertical direction will likely occur as this lowers the energy (shown as green arrows). This results in the antiferromagnetic and ferromagnetic stripes seen. Bottom Panel b): Sketch of 'naked' holes in the Cu-O planes. The holes would still spread out to reduce Coulomb repulsion and would result in the enhancement of the superexchange interaction and formation of Cooper pairs (shown as red circles).

alignment of the Cu spins within a delocalized hole (5 Cu-ion cross) is different from the strength of the interaction between two holes. The latter is enhanced by forcing the Cu-ions closer together. We do not have a solid argument for estimating which one is larger though, so we keep the option open that either energy scale can be the largest when we do numerical calculations.

The alignment of the spins in the vertical direction is likely to be ferromagnetic, but perhaps only weakly so. Should the alignment be FM, then this would greatly enhance the mobility of the hole in the vertical direction. Holes can now travel along the path sketched in panel b) of Fig. 4.8 (orange line). Should the alignment be

AF, then the holes are much less mobile as their motion would involve a spin flip somewhere. It is possible, however, to move without spin flipping as long as the holes move directly from oxygen to oxygen, without 'visiting' the Cu-ions. Given the size of the respective hopping terms that have been estimated from experiments[58] (with $t_{pd} \approx 2t_{pp}$) we consider the latter possibility less likely and we have sketched a FM-alignment in the vertical direction (panel a) of Fig. 4.9).

When the holes travel along the vertical direction along the FM aligned Cu-moments (the direction of the stripes), then the situation after a few hops will be the one sketched in panel a) of Fig. 4.9. These hops can be accommodated independent of whether the spins that were 'unassigned' in panel b) of Fig. 4.8 point up or down. Therefore, it is likely that these Cu-moments will order AF along the vertical direction to lower the energy of the state by a few more tenths of an electron Volt. We sketch these directions in panel a). In short, it is likely that stripes will emerge when holes are traveling in the vertical direction. These stripes consist of Cu-moments aligned predominantly anti-ferromagnetically along one stripe, and ferromagnetically in-between the stripes. Note that the overall alignment along the horizontal direction is such that the direction of the spins in the stripes alternates from one AF (FM) strip to the next AF (FM) strip.

Note that the particular depiction (Fig. 4.7) of a delocalized hole is not essential to this argument. Even 'naked' holes spread apart by Coulomb repulsion would result in an enhancement of the superexchange interaction and in the formation of Cooper pairs consisting of a magnetic hole singlet glued together by a Cu-singlet. We show this in panel b) of Fig. 4.9. The only issue that would be debatable for the 'naked'

holes is whether the vertical mobility of holes would be enhanced by an in-phase arrangement of the AF bonds within a Cooper pair, or an anti-phase arrangement. Since experiment tells us that an anti-phase arrangement occurs, it is likely that Cu spins between the AF-stripes are aligned ferromagnetically near the holes, facilitating hole mobility.

The scenario outlined above comes with a few predictions that appear to be borne out by experiment. First, a minimum hole concentration is needed before the Coulomb force would be able to squeeze two Cu-ions together enough to bind two holes together. When the concentration is too low, holes are kept too far apart to benefit from any increase in superexchange interaction, and Cooper pairs will not form. Experimentally, a hole concentration of 1/16 appears to be sufficient for the onset of superconductivity, corresponding to an average hole separation of $4a$. Second, the sketches in Fig. 4.8 and 4.9 demonstrate that holes move perpendicular to their bonding direction, or at least not parallel to it as this would involve Cu-spin flipping. Thus, at concentrations below p = 1/8, we would expect stripes to still form in the vertical direction, but spaced further apart. Therefore, we expect to observe superlattice peaks at $\delta = \mathrm{p}$ for $\mathrm{p} < 1/8$[81].

An interesting question to ponder is what the hole pattern will be for $\mathrm{p} > 1/8$, when more holes need to be accommodated in the arrangement shown in panel b) of Fig. 4.8. We take p = 1/6, the optimal doping concentration, as an example. The p = 1/8 unit cell of 8×4 nuclear unit cells that accommodated 4 holes now needs to accommodate 6 holes. We can either squeeze the pattern along the horizontal direction (perpendicular to the stripes) or in the vertical direction (along the

stripes). The result of a horizontal compression is shown in panel a) of Fig. 4.10. This appears to be an unlikely possibility as the 'overlap' between the holes would force a greater localization of the holes, increasing their kinetic energy, compared to a vertical compression (panel b) of Fig. 4.10). When we compress along the (vertical) stripe direction, then the holes do not suffer in mobility. Thus, we would not pay the same kinetic energy price, but we would lose the perfect anti-phase AF arrangement along the magnetic stripes. However, every AF bond that has an increased superexchange interaction can still be satisfied, so from kinetic energy arguments, a horizontal compression of the unit cell is not favored over a vertical compression. As a result, we expect to see the IC peak position saturate at $\delta = 1/8$. Of course, this is a well-known experimental observation[82].

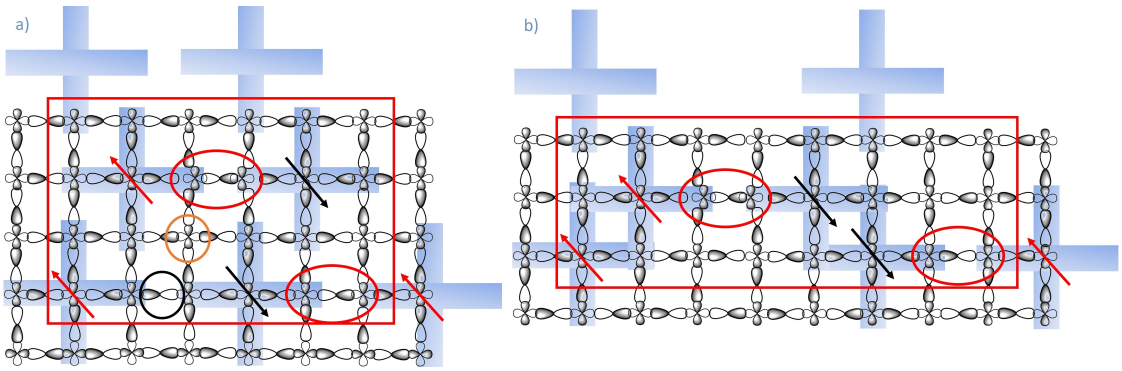

Figure 4.10: Left panel: Schematic showing horizontal compression. Right panel: Schematic displaying vertical compression. The resulting unit cell (red box) has 4 holes per 24 lattice sites. Both panels are at a doping level of p= 1/6.

The consequence of losing a perfect anti-phase stacking arrangement of the AF stripes (holes are now 3 lattice spacings apart along the vertical direction rather than four) is that the static Bragg peak at $(1/2 \pm 1/8, 1/2)$ would disappear, but since the magnetic stripes still exist, we can expect the same magnetic excitations along the stripes to still persist, albeit with an altered intensity in neutron scattering experi-

ments. The result is the development of a spin gap in the experiments. Note that one does not observe the ferromagnetically ordered stripes in experiments probing around $(1/2, 1/2)$ as the magnetic structure factor corresponding to these spin arrangements equals zero.

In summary, using basic energy consideration arguments combined with an increased superexchange mechanism strength when Cu-ions are forced closer together, we arrive at incommensurate lattice peaks with $\delta = \mathrm{p}$ for $\mathrm{p} < 1/8$, as well as a saturation of δ at a value of $1/8$ for $\mathrm{p} > 1/8$. The observation of a spin gap in neutron scattering experiments goes hand-in-hand with this scenario. What it does not automatically imply though is that Cooper pairs remain bonded across the AF stripes. It is quite possible that the holes, located within the FM stripes, form Cooper pairs for $\mathrm{p} > 1/8$. These holes would be very mobile in their FM surroundings, and the energy gain of ordered AF stripes would still be present. However, it would appear that Cooper pairs within FM stripes would form a triplet, at least in the cartoon of what a hole is. As far as we are aware, there is no experimental evidence to back up this possibility of a triple state.

4.5 Magnetic Excitations and the hourglass Dispersion

The presence of a static striped phase allows for the determination of the magnetic excitations through linear spin wave theory. We explore these theoretical spectra as a function of coupling strength between the Cu-ions within the stripes and as a function of the coupling strength between the stripes themselves. We find magnetic dispersion curves that are similar to the experimentally observed hourglass dispersion

and offer a slightly different interpretation of what the upper and lower branches of the hourglass curve signify. Even though the static long-range order of the stripes disappears for high hole dopings, the survival of shorter ranged dynamic correlations between neighboring stripes indicates that the underlying mechanism of superexchange enhancement remains the most relevant feature of the electronic response in the cuprates.

We focus on the stripe pattern for p = 1/8 as this doping level has been studied extensively[58]. We discuss the results of linear spin wave theory for two arrangements: one a highly simplified magnetic unit cell consisting of four nuclear units (panel a of Fig. 4.11) and the other the unit cell pattern of Fig. 4.2, but with added FM correlations (panel b of Fig. 4.11). The latter pattern corresponds to panel a) in Fig. 4.9.

The toy model shown in panel a) of Fig. 4.11 has the advantage that it can be solved exactly (within the linear approximation) so that the influence of different ratios of antiferromagnetic (J_{AFM}) and ferromagnetic (J_{FM}) couplings can be studied. We defer the details of the calculation to Appendix D, here we simply list the spin wave energies E for the two branches below:

$$\begin{aligned} E^2 =& A^2 + B^2 - C^2 \pm 2B\sqrt{A^2 - C^2 sin(2q_x a)} \\ A =& \frac{3}{2}J_{FM} + \frac{1}{2}J_{AFM} - J_{FM}cos(q_y a) \\ B =& \frac{1}{2}J_{FM} \\ C =& \frac{1}{2}J_{AFM} \end{aligned} \tag{4.1}$$

We plot the spin wave energies in Fig. 4.12. There are two things to bear in mind when looking at these dispersions. First, in an experiment we tend to observe

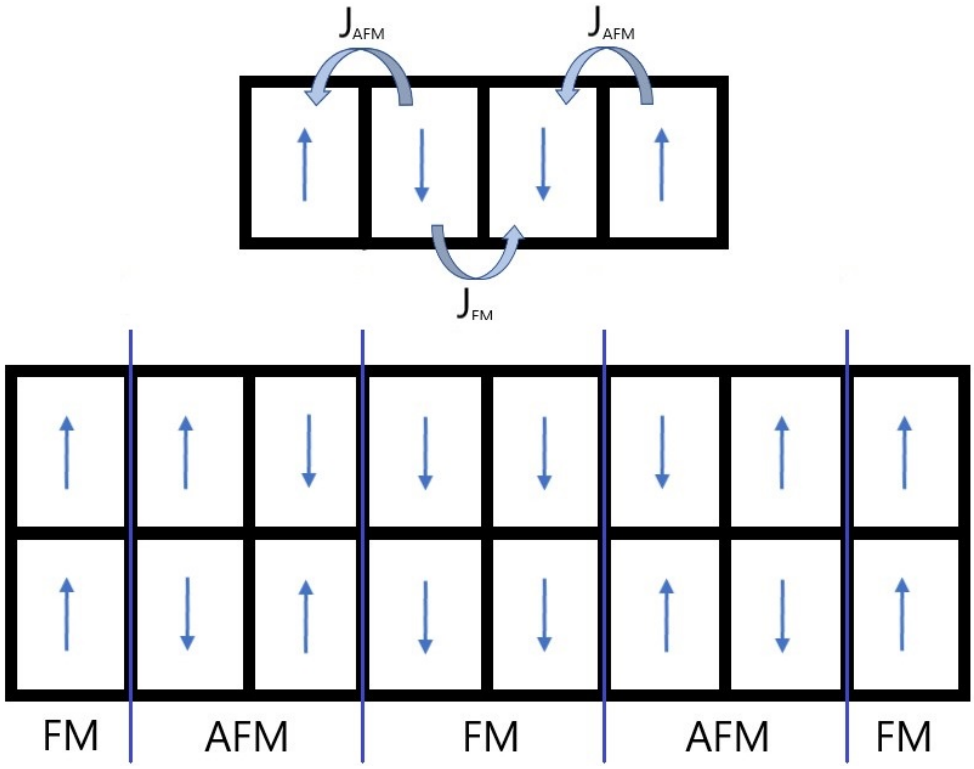

Figure 4.11: Top panel: Schematic showing the magnetic ordering for a 4×1 unit cell. Bottom Panel: Schematic displaying the magnetic ordering for a 8×2 unit cell. Interactions J_{FM} and J_{AFM} are also shown.

excitations along the stripes and perpendicular to the stripes simultaneously as it is experimentally known that the stripe direction alternates from layer to layer (along the c-axis)[58]. Second, these dispersions do not include the magnetic structure factor that determines the cross section for a neutron being able to excite these branches. For instance, the neutron cross-section for this structure at $(1/2, 0)$ equals zero, whereas it is maximum for $(1/4, 0)$. Combining the two branches into one plot and only plotting them for momentum transfers in the zones where the structure factor does not vanish, we arrive at the dispersion (shown in Fig. 4.13) that neutrons would measure in this hypothetical system.

The toy model has some interesting features, such as already indicating that the hourglass shape is the result of a superposition of excitations perpendicular and par-

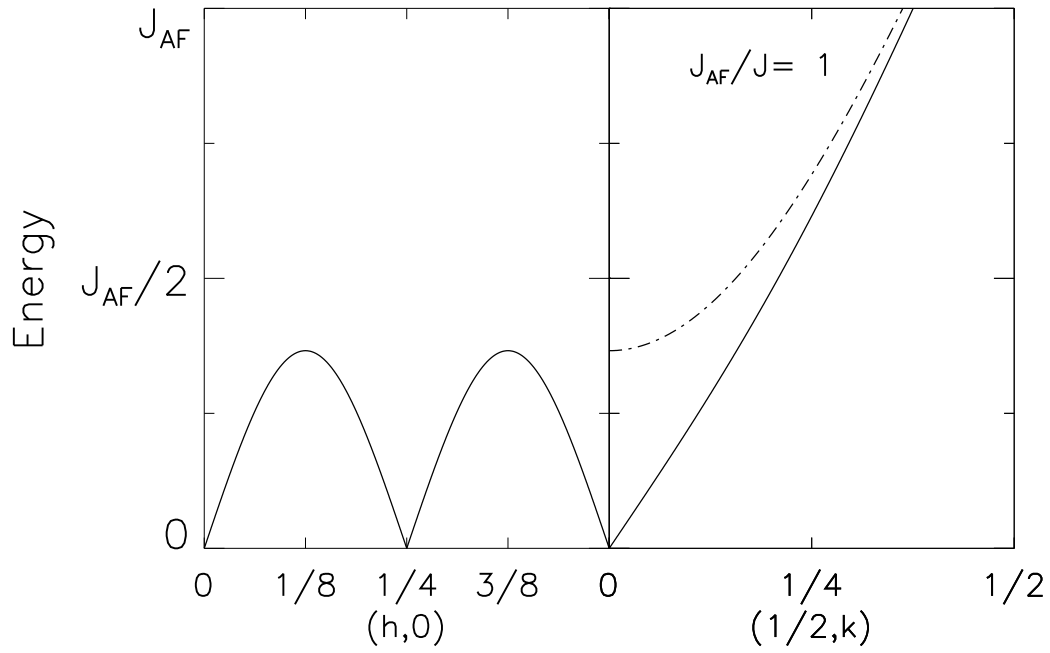

Figure 4.12: Spin wave dispersion for the 4×1 unit cell along h and along k (solid lines). The dotted curve is the dispersion for $(3/8, k)$.

allel to the stripes. It also shows that the dashed curve in Fig. 4.3 that is drawn through the experimentally measured magnetic excitations for the lower branch of the hourglass is without merit. The point $(1/2, 1/2)$ corresponds to a zone center, not to a zone boundary.

The maximum E_{max} of the dispersion along the horizontal direction (corresponding to excitations perpendicular to the stripes in the cuprates) is given by

$$E_{max}^2 = J_{FM}(J_{FM} + J_{AFM}) - J_{FM}[J_{FM}^2 + 2J_{FM}J_{AFM}]^{0.5}. \tag{4.2}$$

This maximum depends on both exchange parameters. It is interesting to take the limit $J_{FM} \gg J_{AFM}$ as this effectively mimics an isolated AF-chain. Taking this limit, the maximum of the dispersion reduces to E_{max}=$J_{AFM}/2$, close to the theoretical result[58] for an AF-chain ($E_{max} \approx J_{AFM}/2$). Therefore, we expect the full model to be able to include the excitations that are expected for uncorrelated AF-chains for

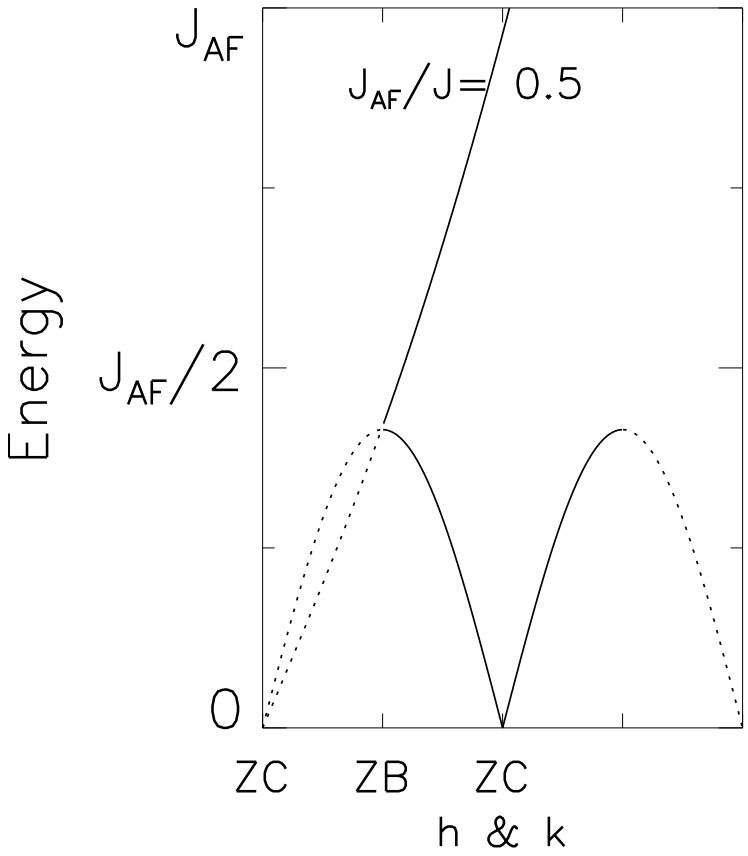

Figure 4.13: Overlaid dispersion with inclusion of the magnetic structure factor. Solid lines give the most prominent features in a neutron scattering experiment.

higher doping levels (p $>$ 1/8)[58].

Next we discuss the spin wave results for the full model shown in the bottom panel of Fig. 4.11. We did not attempt to solve this analytically as it involves finding the eigenvalues of a 32x32 matrix. Rather, we have solved the eigenvalue problem numerically using standard computer software and following the equations from the 1968 treatise written by S. Tjablikow[85]. We include the program for this in Appendix D and plot the dispersion in Fig. 4.14 for three ratios J_{AFM}/J_{FM}.

As expected, the dispersion now has zone centers at integer multiples of $1/\delta$, reflecting the size of the magnetic unit cell. We also see the appearance of many

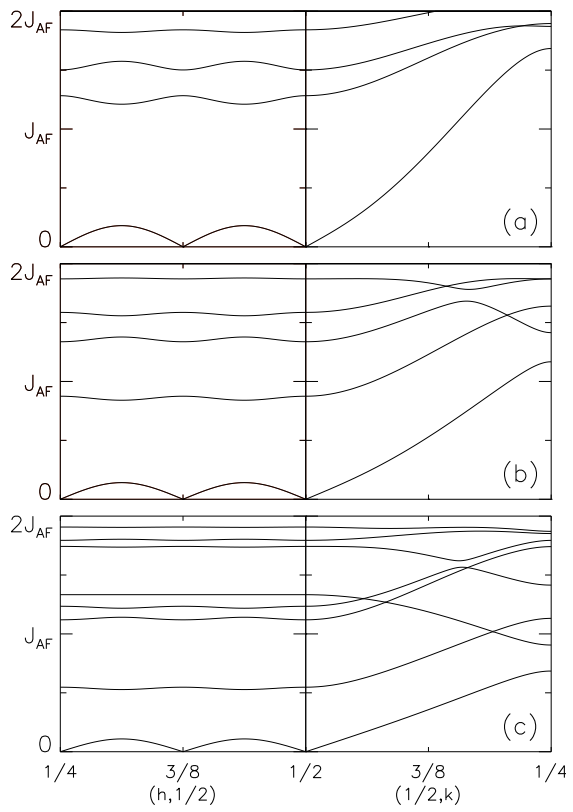

Figure 4.14: Dispersion for the full unit cell along h and k. Panel a) was calculated for a ratio of $J_{FM}/J_{AFM} = 2$, panel b) for $J_{FM} = J_{AFM}$, and panel c) for $J_{FM}/J_{AFM} = 0.5$.

higher energy modes, but well separated from the modes we already identified with the toy model. The most notable difference from the view of comparing the dispersion to experimental values is that the peak of the dispersion for momentum transfers perpendicular to the chain direction no longer reaches $J_{AFM}/2$. Playing around with the ratio J_{AFM}/J_{FM} the highest value we obtained was $E_{max} \approx 0.3 J_{AFM}$.

Another difference is the appearance of an optical branch at the zone center in the energy range of neutron scattering experiments for $J_{FM} < J_{AFM}$. While this branch has no weight in a neutron scattering experiment off of a perfectly ordered sample, once the chains lose their horizontal phase arrangement this branch would acquire some intensity (at the expense of the lower part of the hourglass). It is possible that

the excitations at $(1/2, 1/2)$ observed in (some) neutron scattering experiments[58] (and referred to as E_{cross}[58]) do indeed reflect excitations that propagate along the chain direction, but in a system where the phase arrangement between the chains has been distorted.

Within the Cooper pairing model, there is a subtle difference between single layer compounds such as LSCO and multi-layered compounds such as YBCO. Experimentally, this difference is seen most markedly as the appearance of a resonance peak at $(1/2, 1/2)$ at finite energy ($E = 41$ meV for optimally doped YBCO)[58]. This peak appears upon cooling through the superconducting transition, and is localized both in energy as well as in momentum space. We believe that this peak might reflect a much different process from the ones we described using spin wave theory. We detail this in the following, but we urge the reader to digest this with caution as this is rather speculative.

Should we be correct in the assertion that Cooper pairs are bonded across an AF-correlated pair of Cu-ions, then we expect such entities to exist both in single layered as well as in bi-layered compounds. However, in bi-layered compounds the Cu-ions in the two layers that form the bi-layer are also correlated with each other. The strength of this coupling is not negligible and is given by $J_\perp \approx 10$ meV. We sketch this situation in Fig. 4.15. At low temperatures, we expect all four Copper moments in this Cooper pair to be aligned anti-ferromagnetically.

It is possible to excite this system, even without breaking the Cooper pair. In order to show this, we have calculated the energy levels for the four-copper system using the rules of angular momentum addition. We show the levels in Fig. 4.16. The

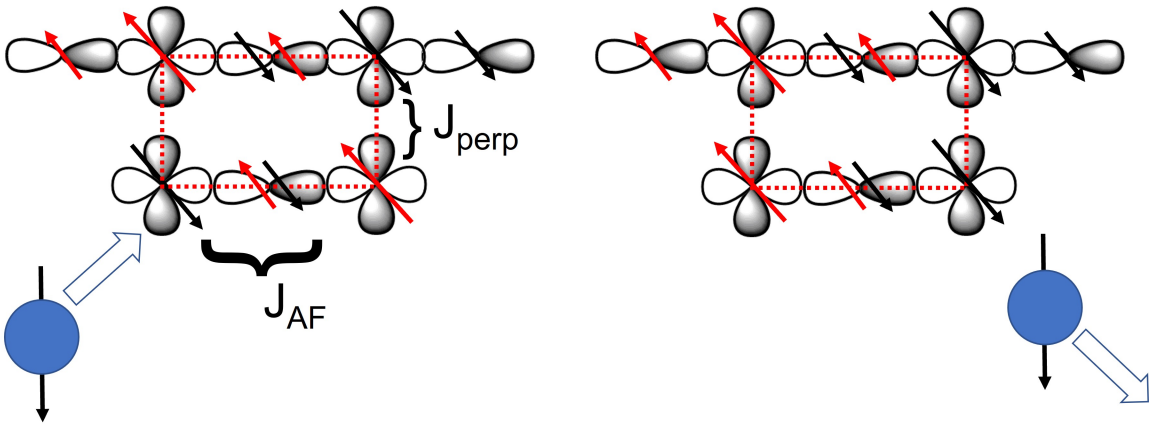

Figure 4.15: Side view of the Cooper pair unit in YBCO. A neutron (blue ball) can interact with this Cooper pair and flip the direction of the two copper moments without breaking up the Cooper pair.

lowest energy transition is between two ($L = 1$, $\ell_z = 0$) states with an excitation energy corresponding to $4J_\perp$, or approximately 40 meV. Visually, this excitation can be viewed as a simultaneous spin flip of the two Cu-moments that are not directly involved in the Cooper pair (right panel of Fig. 4.15). Should this excitation be responsible for the resonance peak, then it directly explains why it only shows as a peak both in energy and in momentum transfer. The sharpness in momentum is directly related to the finite-size effects we detailed when we discussed the ordering of moments on clusters (Section 1.4). Here, the longest wavelength of an excitation able to excite the system corresponds to $2a$. That is, we would see a response at momentum transfers of 1/2 reciprocal lattice units, but no other momentum transfers would be allowed close to this value.

Headings *et al.* have performed [60] polarized neutron scattering experiments of the resonance peak, and observed a signal corresponding to the resonance peak in the neutron spin-flip channels. As the transition between the two $\ell_z = 0$ states would be a non spin-flip transition, these results appear to rule out our interpretation of the

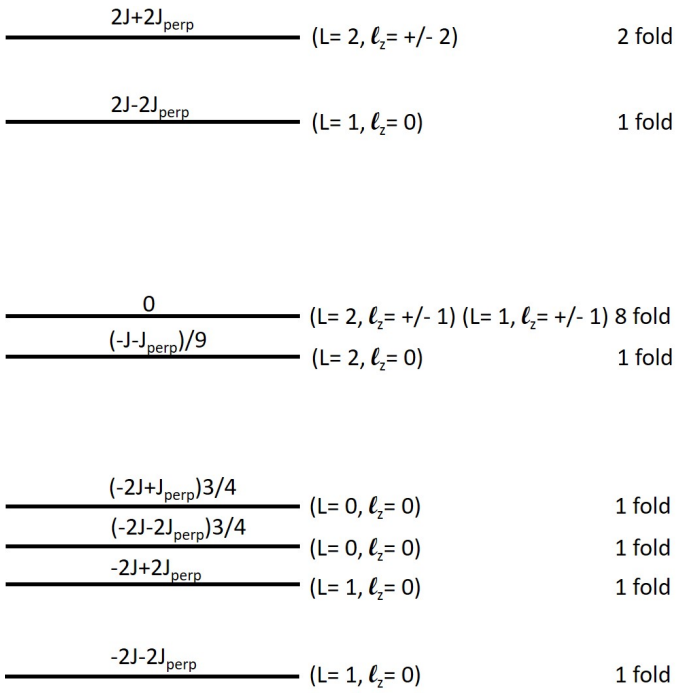

Figure 4.16: The excitation energies of the four-Cu system calculated using the rules of addition of angular momentum together with their degeneracies. The lowest energy transition corresponds to $4J_\perp$, or approximately 40 meV.

resonance peak. However, when we look at the details of the experimental set-up, it is not as simple, even to the point that Headings's findings are actually consistent with our interpretation. We list the argument below, but since this argument goes into the details of what is actually measured in polarized neutron scattering experiments, the reader may want to skip to the end of this section where we summarize the findings from spin wave theory.

It is possible for a neutron to scatter in a non-flip process, but still be registered as having its spin flipped. The essence of the argument is the following: imagine a neutron is prepared with its spin polarized along a certain direction (let's say the x-direction). Next, it gets scattered by the sample in a process where its spin along a different direction (let's say the y-direction) is not flipped, such as scattering by the Cooper pair unit we have described. Next, the scattered neutron is probed to see

whether its polarization along the x-direction has changed. For the scattering process described here, in half of the cases we will find that the direction of polarization has indeed changed. Not because of a spin-flip process, but simply because the spin of this spin-1/2 particle was measured along another direction (y-direction), erasing all information of the spin direction perpendicular to this (y-)direction. Thus, in order to ascertain that Headings *et al.*[60] were indeed looking at a true spin-flip process, we need to look at the details of the experimental setup.

In their polarized neutron scattering experiments, Headings *et al.*[60] measured the response for neutrons polarized along the direction of momentum transfer (which made an angle of 21 degrees with the Cu-O planes), along a vector within the plane, and along a vector perpendicular to both, that is, a vector at an angle of 69 degrees to the plane. Neutrons only scatter magnetically if there is a component of the Cu-spin perpendicular to the direction of momentum transfer (intensity $\sim$ 1-cos$^2\alpha$ with α the angle between the Cu-spin and the direction of momentum transfer). Another complication is that the Cu-spins are confined to within the planes, but can still point in any planar direction. Finally, spin excitations are transverse excitations, implying that we also need a component of the neutron spin perpendicular to the copper spin in order to get scattering.

We have evaluated these three intensity considerations numerically by averaging over all possible spin directions of the Cu-moments in the plane, and calculating the cross-sections for the three polarization directions. Then we 'erased' the initial polarization for events where the direction of the neutron spin was probed perpendicular to the initial polarization direction. In doing so, we found that we could expect non-flip

scattering events in the spin-flip channel with an intensity ratio of roughly a factor of 2 between the along-Q and perpendicular-to-Q polarization directions. This ratio was consistent with the reported experimental data[60]. We also calculated the cross-sections for the non-flip channel (the channel that is 'contaminated' by phonon scattering), but within the experimental accuracy we could not tell whether the calculated level of scattering was present, or absent in this channel. Thus, we concluded that it is quite possible that the resonance peak is associated with scattering by a Cooper pair assembly, but until there is an experiment with higher accuracy in the non-flip channel we cannot be confident in this conclusion.

In summary, we tried to make the following points in our discussion of the magnetic excitations:

- As long as there is some coupling between the chains, then we can expect a well-defined AF-dispersion in the direction perpendicular to the chains.

- The maximum of this dispersion is lower than that of an isolated AF-chain when probed along the chain direction.

- There is no evidence for any dispersion curve connecting the incommensurate lattice point $(1/2+\delta, 1/2)$ at $E = 0$, to excitations at $(1/2, 1/2)$ at finite energy; these two points are not part of the same branch of dispersions.

- The top part of the hourglass represents excitations along the chain direction, the lower part is associated with excitations perpendicular to it.

- Within a phase of AF-chains, any intensity at $(1/2, 1/2)$ can only arise from disorder among the chain arrangements, such as a dynamic character for the

chains location and phase.

- The resonance peak in the bi-layered compounds might be associated with directly probing a Cooper pair at an energy that happens to coincide with E_{cross}.

We have left one issue untouched: why does the lower part of the hourglass only disperse inwards [toward $(1/2, 1/2)$], but not outward as it does for other striped non-superconducting compounds? Note that this issue is independent of whether the model (Fig. 4.8 and 4.9) or some other model is correct. Whenever we have a superlattice peak, we expect to see two branches emanate from it. After all, what system would it be where excitations can only propagate from left to right, but not from right to left? We have not been able to find an explanation for this in the literature, only mentions that intensity is transferred to the inward branch without detailing a mechanism for this transfer. We also do not have an explanation. On the one hand, we can see that the inward branch should be favored over the outward branch as soon as disorder is introduced. In the extreme case of the stripes becoming uncorrelated from each other, we expect all the intensity to be around $(1/2, 1/2)$ at the expense of the superlattice peak intensity. In addition, the dispersion is very steep, and as such, we would not be able to observe two branches coming from the zone center within the resolution of the instrument. Only high resolution experiments on hypothetical perfectly arranged AF stripes would allow us to do this. In short, we do not know whether the observed absence of outward dispersion presents a real issue, or merely reflects the large degree of disorder in the locations and phases of the AF stripes. We note, that this does not seem to have troubled anyone in the literature either.

4.6 Comparison to the Superfluid Phase of ^{4}He and Superconducting Transition Temperature

The energy scale of the Cooper pairs in the cuprates appears to be much higher than the superconducting transition temperature; this is in contrast to BCS superconductors where the energy scale Δ of the Cooper pairs is comparable to the transition temperature: $\Delta = 1.76 k_B T_c$[61]. In this section, we make a comparison between the superfluid phase of ^{4}He and the superconducting phase of the cuprates to argue that the the transition temperature in the cuprates is not related to the pairing energy, but to that of low lying magnetic excitations. As such, the transition temperature is not linked to the breaking up of Cooper pairs, but rather to an energy gap that Cooper pairs need to bridge in order to scatter inelastically. This section is the most speculative of this chapter.

Ever since the discovery of superfluity in helium-4 there have been parallels drawn between the flow without viscosity in He and the flow of electrons without resistance in superconductors. This goes back to the early days of the two fluid model, and persists today with more accurate models and theoretical understanding[61]. However, in these comparisons the superfluid phase is often mischaracterized, in addition to the comparisons only being qualitative. In here we make a more accurate comparison with the aim of trying to find the energy scale in superconductors that determines the transition temperature.

Liquid ^{4}He undergoes a second order phase transition at $T = 2.17$ K from a normal fluid phase into a superfluid phase where the liquid can flow through thin capillaries without viscosity[61]. Neutron scattering experiments have revealed that the pre-

diction by Fritz London that a Bose condensate forms in He was correct, with the condensate fraction determined to be around 8%. This is similar to superconductors where electrons condense into Cooper pairs. Unfortunately, in comparing the two systems there is little distinction made between the condensate and the superfluid fraction in He, whereas the two are very different entities. While the condensate fraction reaches 8% at $T = 0$ K, the superfluid fraction (the fraction of the fluid that partakes in frictionless flow) reaches 100%.

Another way to appreciate the difference between the condensate and the superfluid fraction is by looking at an ideal Bose gas of non-interacting atoms. This gas also undergoes a phase transition, but here 100% of the atoms form the condensate while the system is not superfluid (0% superfluid fraction). At the heart of this distinction is that the condensate is a property of the ground state, but the superfluid fraction is a property of the excited states. We have a similar situation in the superconductors: the ground state is characterized by a condensation into Cooper pairs (not a condensation of pre-formed Cooper pairs), while the superconducting properties are given by the gap between the ground state and the excited states. The situation in helium is often viewed, incorrectly, as being almost identical with the excited states being associated with kicking a particle out of the Bose condensate. However, as Feynman already showed, the gap between the ground state and excited states in He is due to Bose statistics, not to the energy scale of the Bose condensate. We expand on this in the following so as to arrive at the energy scale that does determine the superfluid transition temperature and to look for a similar scale in the cuprates.

In order for a fluid flowing through a capillary to slow down, it needs to transfer its

energy and momentum into internal degrees of freedom of the liquid. In other words, there should be internal friction, allowing the fluid to heat up. Should a minimum energy be required to excite an internal degree of freedom, then flow velocities below that minimum requirement have no means of slowing down. An everyday analogue would be to go shopping in a dollar store with 50 cents: ultimately, we leave the store still holding the 50 cents. Bearing in mind, that the velocities are associated with the slope of dispersion curves. We illustrate in Fig. 4.17[61] what determines the critical flow velocity below which the flow cannot degrade.

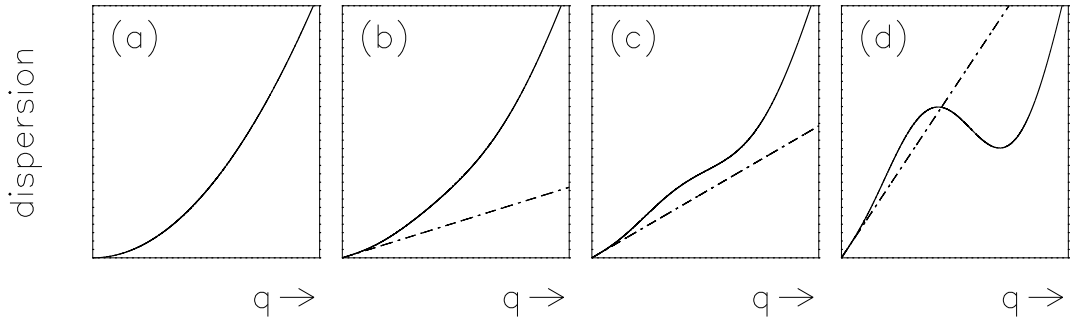

Figure 4.17: Figure reproduced from Montfrooij *et al.*[61]. Left panel a) shows the quadratic dispersion as a function of momentum transfer $\hbar q$ for a non-interacting system of bosons. This system is 100% Bose condensed, but it is not a superfluid. Left Middle panel (b): Turning on the interaction between the bosons results in a low-q renormalization of the dispersion, resulting in a superfluid with a critical velocity determined by the slope shown by the dashed curve. Right Middle panel (c): Increasing the interaction strength sees structure appearing in the dispersion curve. Right panel (d): The interaction has been increased until it represents the interaction between helium atoms. The critical velocity is now determined by the minimum of the dispersion (no longer by the dashed curve). Note that the renormalization of the curve at low q is still essential to the argument of there existing a critical velocity.

Looking at panel (a) of Fig. 4.17 we see the quadratic dispersion of an ideal Bose gas. The ground state energy (including the condensate) constitutes the horizontal axis at $E = 0$. We see directly that this ideal Bose gas is not superfluid as the minimum slope of the dispersion equals zero. Bogoliubov[89] showed that by including a small interaction between the atoms, that the lower part of the dispersion is renor-

malized, and now the excitation energy is linear in momentum transfer. In other words, we observe a finite slope, and therefore, there is a lower critical velocity that is not equal to zero. Increasing the interaction further, we see that the atoms start to carve out their own space and more structure appears in the dispersion. A minimum develops for wavelengths corresponding to the interatomic separations. In essence, the cost of imposing a density fluctuation in the liquid is lowest when the wavelength matches the distance that atoms would already like to be at in the first place. In a solid, this minimum (called the roton minimum in He) would go all the way to zero and we would recover the phonon dispersion originating from a Bragg point. Notice how the minimum velocity is now given by the curve through the origin and tangent to the roton minimum; it is no longer determined by the low-q part of the dispersion.

Feynman explained how the roton minimum is a consequence of the Bose nature of the ^{4}He atoms, not of the presence of the condensate. These arguments were quantified by Montfrooij *et al.*[61] who showed that the entire dispersion curve can be calculated from first principles based on the notion that the excited states are characterized by density fluctuations that cannot decay because of the roton gap. The agreement between these calculations and experiment turned out to be highly accurate. Moreover, it was possible to relate the superfluid transition temperature T_λ directly to the minimum velocity v_c obtained from the dispersion curve in a simple equation:

$$\frac{1}{2}m(2v_c^2) = \frac{3}{2}k_B T_\lambda. \tag{4.3}$$

In a thesis on strongly correlated electron systems the point is not to go into the details of superfluid helium, but rather to illustrate that it is not necessarily the size of

the gap between the ground state and the excited states that is important, but rather the critical velocity associated with it. This is particularly relevant to the cuprates as they much more closely resemble the situation in He than BCS superconductors do. The Cooper pairs are very strongly bonded, and the transition temperature is well below the energy scale of this bond. This is similar to the situation in He where superflow does not break down because the bosons (atoms) break up, in contrast to BCS superconductors where the Cooper pairs do break up. This leads us to the question: is there an equivalent of a critical flow velocity in the superconductors? Note that a relation like the one shown above (Eq. 4.3) does not hold for superconductors as electrons do not obey the same velocity distribution as bosons do (not even electrons bound in Cooper pairs), it merely illustrates that there exists a critical velocity for (composite) bosons to be able to slow down.

In order to develop an idea of the energy scale involved, we look at the maximum critical current densities that have been achieved in the cuprates. The highest value we came across was 8×10^6 A/cm^2[58]. Bearing in mind that the supercurrent flows through the Cu-O planes, and that a Cooper pair has a charge of $2e$, we can convert the value for of critical current to a critical flow velocity as follows. We use $4\times4\times12$ Å^3 as the typical unit cell size. A current density of 8×10^6 A/cm^2 corresponds to 5×10^{25} electrons/s.cm^2 passing by. Since the cross section of a unit cell equals 4×12 Å^2, we have that 2.4×10^{11} electrons flow through a single unit cell every second. At optimal doping in YBCO we have 1/3 of a charge carrier (1/6 per layer in the bi-layer) per unit cell. Therefore, the charge contained in $3\times2.4\times10^{11}$ unit cells needs to pass through a single unit cell. The length of that many unit cells in a row equals

$3\times2.4\times10^{11}\times4$ Å= 300 m. Therefore, the average speed of an electron equals 300 m/s, equivalent to 2 meV.Å. This is the value we need to compare the slope of a dispersion to when looking for critical velocities.

The energy values discussed so far when dealing with spin wave theory and the resonance peak are far too high to be of relevance. For instance, the resonance peak would correspond to a velocity of 40 meV/($\pi/4\sqrt{2}$/Å)= 36 meV.Å. However, we are looking for energy gaps of the order of 3 meV at the $(1/2, 1/2)$ point. As it turns out, energy gaps of this magnitude are present in the magnetic excitation spectrum of the cuprates and are known as the anisotropy gap.

Because of spin anisotropy the Cu-moments are confined to point in the Cu-O plane, where they are free to rotate. This is why the system is known as a good approximation to a 2D Heisenberg anti-ferromagnet. Because of this anisotropy, it costs a finite amount of energy to point the spins perpendicular to the Cu-O plane. When doing linear spinwave theory on the AF parent compounds, we find that this results in a spin gap at the zone center with an energy of $J\sqrt{2\alpha_D}$. The actual value of the anisotropy parameter α_D is difficult to determine, with estimates putting it somewhere around 3 x 10^{-4} in YBCO. In other words, the anisotropy gap $J\sqrt{2\alpha_D}$ is of the order of 3 meV ($J \approx 100$ meV), of the same order as hinted at by the reasoning provided earlier on the critical current. Of course, this can simply be a numerical coincidence, and it can also be that the comparison to superfluid helium does not hold water, but it certainly would appear to be an avenue worth exploring as none of the other energy scales discussed in the literature correspond to the observed transition temperatures.

4.7 Conclusions

We have applied the findings on the importance of small changes in inter-ionic separations to the response of a system to the cuprates. We have identified that the increase in superexchange interaction when two Cu-ions are pushed closer together should have ramifications for the understanding of the interplay between electronic excitations and magnetic ones. We have identified particular phonon modes that would be important in this process, the very same phonon modes that show anomalous behavior upon cooling down through the superconducting transition. It is not clear whether this represents electron-phonon coupling in the BCS sense, or whether the phonon energies simply become renormalized because the Coulomb repulsion between holes sets up the same ionic displacements that the phonon is trying to create.

We combined the increased likelihood of two individual Cu ions aligning antiferromagnetically (where the superexchange is enhanced) with mobility arguments for the holes. Doing so, we arrived at a Cooper pairing mechanism and a striped pattern for regions of antiferromagnetic and ferromagnetic Cu-moment pairing. The periodicity of these regions matches those observed in experiments. We applied spin wave theory to these patterns to shed light on the famous hourglass dispersion measured in the cuprates, arguing that the lower part represents excitations perpendicular to the stripes, and the upper part being excitations that propagate along the stripes. We also discussed the resonance peak and how it might be related to probing a Cooper pair directly, but we could only conclude that this interpretation was consistent with the overall scenario, not evidence for it.

We ended by suggesting that the relevant energy scale at the heart of the super-

conducting transition temperature might actually be the spin anisotropy of the Cu moments that forces them to point in a direction in the Cu-O planes, rather than perpendicular to it. We made this argument by drawing upon the lessons learned from the superfluid transition in helium-4. Even if the arguments in that section might prove to be fallacious, the conclusion that the spin anisotropy might be the relevant energy scale in the cuprates could well be correct.

Appendices

Appendix A

RKKY Interaction - Hamiltonian

The Ruderman-Kittel-Kasuya-Yoshida (RKKY) interaction is a long range coupling mechanism mediated by conduction electrons, in which interactions of conduction electrons with magnetic moments induce a coupling of localized magnetic moments. Conduction electrons interact with magnetic moments through an exchange interaction, the strength of which is defined as J. This interaction was first proposed as an explanation for the uncharacteristically large nuclear spin resonance seen in silver by M.A. Ruderman and C. Kittel in 1954 at th University of California, Berkeley. T. Kasuya and K. Yoshida later generalized the theory to what is known today as the RKKY interaction.

First, the material considered must be able to be described by a crystalline lattice and can be described by a set of plane wave solutions to the Schrodinger Equation of the form $\Psi(\boldsymbol{r}) = e^{i\boldsymbol{k}\cdot\boldsymbol{r}}u(\boldsymbol{r})$, where $\boldsymbol{r}$ is position, Ψ is the wave function, $\boldsymbol{k}$ is the crystal momentum wave vector, and u is a function with identical periodicity as the crystal. These solutions are colloquially known as Bloch States. Next, assume N electrons in the crystal with well defined positions $\boldsymbol{R}_i$ and localized spins $\vec{S}_i$ for $i = 1, ..., N$; the

Hamiltonian can be written as

$$\boldsymbol{r}H = \sum_{\sigma=\uparrow\downarrow}\sum_{\boldsymbol{k}} E(\boldsymbol{k}) c^{\dagger}_{s\boldsymbol{k}} c_{s\boldsymbol{k}} + \sum_{i=1}^{N}\sum_{s,s'=\uparrow\downarrow}\sum_{\boldsymbol{k},\boldsymbol{k}'} e^{i\mathbf{R}_i\cdot(\boldsymbol{k}'-\boldsymbol{k})} J_{\boldsymbol{k}\boldsymbol{k}'} \vec{S}_i \cdot (c^{\dagger}_{s\boldsymbol{k}} \vec{\sigma_{ss'}} c_{s'\boldsymbol{k}'}) \quad \text{(A.1)}$$

where $\boldsymbol{k}$ is the Block momentum vector, $\vec{\sigma}$ is a a vector whose x,y,z components are the Pauli matrices, and $c^{\dagger}_{s\boldsymbol{k}}(c_{s\boldsymbol{k}})$ are the creation and annihilation operations, respectively, of an electron with spin s.

The conduction electrons mediating the interaction partially occupy the conduction band and only conduction electrons close to the Fermi Surface therefore contribute strongly to the interaction strength. The energy of such electrons can be written as $E(\boldsymbol{k}) = \hbar^2\boldsymbol{k}^2/2m^*$ for $\boldsymbol{k} \leq \boldsymbol{k}_F$ where $\boldsymbol{k}_F$ is the momentum at the Fermi Level and m^* is the effective mass of the "heavy electron" in the crystal. Using second order perturbation theory concerning J, we can write the matrix element H_{ij}, the interaction between two localized moments, as

$$H_{ij} = \frac{\vec{S}_i \cdot \vec{S}_j}{4} \frac{|J|^2 m_*}{(2\pi)^3 R_{ij}^4 \hbar^2} \left[2k_F R_{ij}\cos(2k_F R_{ij}) - \sin(2k_F R_{ij})\right]. \quad \text{(A.2)}$$

From this expression, the interaction strength of $J \sim J^2$ and is oscillatory in nature. Therefore small changes in the distance between neighbors, $\boldsymbol{R}_i$, can alter the strength of J and can induce either ferromagnetic or antiferromagnetic coupling between two magnetic moments.

Appendix B

Two and Three Level Systems

Consider a crystal solid comprised of N distinguishable atoms each with two distinct energy levels ϵ and $\epsilon + \Delta$ corresponding to spin up or spin down respectively. This system is colloquially known as a two level system.

The partition function for such a system can be written as

$$Z = [g_1 e^{-\epsilon/k_B T} + g_2 e^{-(\epsilon+\Delta)/k_B T}]^N = [e^{-\epsilon/k_B T}(g_1 + g_2 e^{-\Delta/k_B T})]^N, \tag{B.1}$$

where g_1 and g_2 are the degeneracies for the first and second energy level. We can easily write down the energy, E, for the two level system as well

$$E = N[\frac{g_1 \epsilon e^{-\epsilon/k_B T} + g_2(\epsilon+\Delta)e^{-(\epsilon+\Delta)/k_B T}}{e^{-\epsilon/k_B T}(g_1 + g_2 e^{-\Delta/k_B T})}] = N[\epsilon + \frac{g_2 \Delta e^{-(\epsilon+\Delta)/k_B T}}{g_1 + g_2 e^{-(\epsilon+\Delta)/k_B T}}]. \tag{B.2}$$

Using the partition function, the free energy, F, can be written as $F = -k_b T \ln(Z)$,

$$F = N[\epsilon - k_b T \ln(g_1 + g_2 e^{-\Delta/k_B T})]. \tag{B.3}$$

The specific heat can be found using $C = \mathrm{d}E/\mathrm{d}T$,

$$C = N k_b (\frac{\Delta}{k_b T})^2 \frac{g_1}{g_2} \frac{e^{\Delta/k_B T}}{[1 + \frac{g_1}{g_2} e^{\Delta/k_B T}]^2}. \tag{B.4}$$

Integrating C or using $S = -\mathrm{d}F/\mathrm{d}T$, we can calculate the entropy, S,

$$S = N k_b [\ln(g_1 + g_2 e^{-\Delta/k_B T}) + \frac{\Delta e^{-\Delta/k_B T}}{T[\frac{g_1}{g_2} + e^{-\Delta/k_B T}]}]. \tag{B.5}$$

Assuming an effective magnetic moment p_1 and p_2 (in units of μ_B) respectively, the susceptibility, χ, is given by

$$\chi = [\frac{N{\mu_B}^2}{3k_bT}]\frac{p_1^2 + p_2^2\frac{g_2}{g_1}e^{-\Delta/k_BT}}{1+\frac{g_2}{g_1}e^{-\Delta/k_BT}}. \tag{B.6}$$

For a three level system, consider the same system as the two level system; a crystal solid comprised of N distinguishable atoms each albeit with three distinct energy levels. Without loss of generality, the energy levels can be chosen to be 0, ϵ and $\epsilon + \Delta$.

The partition function for such a system can be written as

$$Z = [g_1 + g_2e^{-\epsilon/k_BT} + g_3e^{-(\epsilon+\Delta)/k_BT}]^N = [g_1 + e^{-\epsilon/k_BT}(g_2 + g_3e^{-\Delta/k_BT})]^N, \tag{B.7}$$

From the partition function, we can calculate the appropriate derivatives from above in order to calculate the necessary property.

Appendix C

Magnetic Units - Gaussian (CGS) and SI (MKS) Units

In magnetic systems and experiments, Gaussian-CGS units are commonly used. The standard units are centimeters (cm), grams (g), and seconds (s) and while not as common, the gauss (G) and the oersted (Oe) are used as well. In contrast, SI units use meters (m), kilograms (kg), seconds (s), amperes (A), and moles (mol). The unit of a tesla (T) is also commonly used in SI units and can be written as

$$[\mathrm{T}] = \frac{[\mathrm{Vs}]}{[\mathrm{m}^2]} = \frac{[\mathrm{N}]}{[\mathrm{Am}]} = \frac{[\mathrm{J}]}{[\mathrm{Am}^2]} = \frac{[\mathrm{kg}]}{[\mathrm{Cs}]} = \frac{[\mathrm{Ns}]}{[\mathrm{Cm}]} = \frac{[\mathrm{kg}]}{[\mathrm{As}^2]} \tag{C.1}$$

where [C] = coulombs, [J] = joules, [N] = newtons, and [V] = volts. Constants for magnetic systems can be written as

$$\mu_B = 9.274 \times 10^{-21} \frac{[erg]}{[\mathrm{G}]} = 9.274 \times 10^{-24} \frac{[\mathrm{J}]}{[\mathrm{T}]}. \tag{C.2}$$

$$\mu_0 = \frac{[\mathrm{Tm}]}{[\mathrm{A}]} = \frac{[\mathrm{N}]}{[\mathrm{A}^2]} = \frac{[\mathrm{H}]}{[\mathrm{m}]}. \tag{C.3}$$

where [H] = Henry. In Gaussian units,

$$\mu_0 = 1. \tag{C.4}$$

In Gaussian-CGS units, [emu] is also commonly used and can be written as

$$1[\text{emu}] = 10^{-3}\frac{[\text{J}]}{[\text{T}]} = 1.0783 * 10^{20}[\mu_B]. \tag{C.5}$$

In magnetization:

$$1\frac{[\text{emu}]}{[\text{mol}]} = \frac{[1.0783 * 10^{20}[\mu_B]]}{[6.023 * 10^{23}[\text{Fu}]]} = \frac{1}{5585}\frac{[\mu_B]}{[\text{Fu}]} \tag{C.6}$$

where [Fu] = formula units or particles, which could be atoms, molecules, electrons, etc... depending on the system. In susceptibility:

$$1\frac{[\text{emu}]}{[\text{mol}]} * \frac{[1[\mu_B]/[\text{Fu}]]}{[5585[emu]/[\text{mol}]]} * \frac{10^4[\text{G}]}{[\text{T}]} = \frac{1.7905[\mu_B]}{[\text{FuT}]}. \tag{C.7}$$

In Gaussian units,

$$B[\text{G}] = H[\text{Oe}] + M[\text{G or Oe}]. \tag{C.8}$$

Magnetization, M, can be defined as

$$M = \frac{magnetic\,moment}{per\,unit\,volume}. \tag{C.9}$$

which can also be given as $[\mu_B]/[\text{Fu}]$. DC susceptibility is given $\chi = M/H$ while the ac-susceptibility is given by $\chi = \mathrm{d}M/\mathrm{d}H$.

Appendix D

Dispersion Program

We have solved the eigenvalue problem numerically using standard computer software and following the equations from the 1968 treatise written by S. Tjablikow[85]. We include the program for this below. The program was used to calculate the dispersion seen in Fig. 4.14.

```
 function spinwavematrixLSCOsmall,x,h,k,l,jab=jab,jaf=jaf
 ; returns eigenvalues for a given (h,k,l)
 ; x is a dummy variable)
 h=(double(h))(0) & k=double(k) & l=double(l)
 if not keyword_set(jab) then jab=1.d0  ; ferromagnetic exchnage
 if not keyword_set(jaf) then jaf=1.d0  ; af exchange


 diag=lindgen(32)*33
 mat=dcomplexarr(16,16)
 sab=mat & rab=mat ; the S and R matrices from page 111 in Tjablikow



 ; we only look at nearest neighbors, take a=b=c=one
 ; use extended 8x2x1 unit cell
 nx=float(8) & ny=float(2) & nz=float(1)
 astar=dcomplex(0,1)*2.d0*!dpi/1.
 bstar=dcomplex(0,1)*2.d0*!dpi/1.
 cstar=dcomplex(0,1)*2.d0*!dpi/1.
 ; phase factors for nearest neighbors
 horpos=exp(astar*scalar_product([h,k,l],[1./nx,0,0])) & conhor=conjugate(horpos)
 verpos=exp(bstar*scalar_product([h,k,l],[0.,1./ny,0])) & conver=conjugate(verpos)
 zpos=exp(cstar*scalar_product([h,k,l],[0.,0,1./nz]))  & conz=conjugate(zpos)
 ; first fill out the sab diagonal

 n=[0,3,4,7] & for i=0,n_elements(n)-1 do sab(n(i),n(i))=2.0*jab
 n=[8,11,12,15] & for i=0,n_elements(n)-1 do sab(n(i),n(i))=0.5*jaf+1.5*jab
 n=[1,2,5,6] & for i=0,n_elements(n)-1 do sab(n(i),n(i))=0.5*jab+1.5*jaf
  n=[9,10,13,14] & for i=0,n_elements(n)-1 do sab(n(i),n(i))=2.*jaf

 ; do all neighbor pairs by only taking left-right and down-up directions to avoit
double counting
 n= 0 & mu=n+8 & mr=n+1 & if mr/8*8 eq mr then mr=mr-8 & if mu gt 15 then mu=mu-16
 sab(n,mu)=-0.5*jab*(conver+verpos) & sab(n,mr)=-0.5*jab*conhor &
sab(mr,n)=conjugate(sab(n,mr)) & sab(mu,n)=conjugate(sab(n,mu))

 n= 1 & mu=n+8 & mr=n+1 & if mr/8*8 eq mr then mr=mr-8 & if mu gt 15 then mu=mu-16
 rab(n,mu)=0.5*jaf*(conver+verpos) & rab(n,mr)=0.5*jaf*conhor & rab(mr,n)=rab(n,mr)
& rab(mu,n)=rab(n,mu)

 n= 2 & mu=n+8 & mr=n+1 & if mr/8*8 eq mr then mr=mr-8 & if mu gt 15 then mu=mu-16
 rab(n,mu)=0.5*jaf*(verpos+conver) & sab(n,mr)=-0.5*jab*horpos &
sab(mr,n)=conjugate(sab(n,mr)) & rab(mu,n)=rab(n,mu)

 n= 3 & mu=n+8 & mr=n+1 & if mr/8*8 eq mr then mr=mr-8 & if mu gt 15 then mu=mu-16
 sab(n,mu)=-0.5*jab*(verpos+conver) & sab(n,mr)=-0.5*jab*horpos &
sab(mr,n)=conjugate(sab(n,mr)) & sab(mu,n)=conjugate(sab(n,mu))

 n= 4 & mu=n+8 & mr=n+1 & if mr/8*8 eq mr then mr=mr-8 & if mu gt 15 then mu=mu-16
```

```
 sab(n,mu)=-0.5*jab*(verpos+conver) & sab(n,mr)=-0.5*jab*horpos &
sab(mr,n)=conjugate(sab(n,mr)) & sab(mu,n)=conjugate(sab(n,mu))

 n= 5 & mu=n+8 & mr=n+1 & if mr/8*8 eq mr then mr=mr-8 & if mu gt 15 then mu=mu-16
 rab(n,mu)=0.5*jaf*(verpos+conver) & rab(n,mr)=0.5*jaf*horpos & rab(mr,n)=rab(n,mr)
& rab(mu,n)=rab(n,mu)

 n= 6 & mu=n+8 & mr=n+1 & if mr/8*8 eq mr then mr=mr-8 & if mu gt 15 then mu=mu-16
 rab(n,mu)=0.5*jaf*(conver+verpos) & sab(n,mr)=-0.5*jab*conhor &
sab(mr,n)=conjugate(sab(n,mr)) & rab(mu,n)=rab(n,mu)

 n= 7 & mu=n+8 & mr=n+1 & if mr/8*8 eq mr then mr=mr-8 & if mu gt 15 then mu=mu-16
 sab(n,mu)=-0.5*jab*(conver+verpos) & sab(n,mr)=-0.5*jab*conhor &
sab(mr,n)=conjugate(sab(n,mr)) & sab(mu,n)=conjugate(sab(n,mu))

 n= 8 & mu=n+8 & mr=n+1 & if mr/8*8 eq mr then mr=mr-8 & if mu gt 15 then mu=mu-16
 rab(n,mr)=0.5*jaf*conhor & sab(n,mu)=-0.5*jab*(conver+verpos) &
sab(mu,n)=conjugate(sab(n,mu)) & rab(mr,n)=rab(n,mr)


 n= 9 & mu=n+8 & mr=n+1 & if mr/8*8 eq mr then mr=mr-8 & if mu gt 15 then mu=mu-16
 rab(n,mu)=0.5*jaf*(verpos+conver) & rab(n,mr)=0.5*jaf*horpos & rab(mr,n)=rab(n,mr)
& rab(mu,n)=rab(n,mu)

 n= 10 & mu=n+8 & mr=n+1 & if mr/8*8 eq mr then mr=mr-8 & if mu gt 15 then mu=mu-16
 rab(n,mu)=0.5*jaf*(conver+verpos) & rab(n,mr)=0.5*jaf*conhor & rab(mr,n)=rab(n,mr)
& rab(mu,n)=rab(n,mu)

 n= 11 & mu=n+8 & mr=n+1 & if mr/8*8 eq mr then mr=mr-8 & if mu gt 15 then mu=mu-16
 sab(n,mu)=-0.5*jab*(verpos+conver) & sab(n,mr)=-0.5*jab*horpos &
sab(mr,n)=conjugate(sab(n,mr)) & sab(mu,n)=conjugate(sab(n,mu))

 n= 12 & mu=n+8 & mr=n+1 & if mr/8*8 eq mr then mr=mr-8 & if mu gt 15 then mu=mu-16
 rab(n,mr)=0.5*jaf*horpos & sab(n,mu)=-0.5*jab*(verpos+conver) &
sab(mu,n)=conjugate(sab(n,mu)) & rab(mr,n)=rab(n,mr)

 n= 13 & mu=n+8 & mr=n+1 & if mr/8*8 eq mr then mr=mr-8 & if mu gt 15 then mu=mu-16
 rab(n,mu)=0.5*jaf*(conver+verpos) & rab(n,mr)=0.5*jaf*conhor & rab(mr,n)=rab(n,mr)
& rab(mu,n)=rab(n,mu)

 n= 14 & mu=n+8 & mr=n+1 & if mr/8*8 eq mr then mr=mr-8 & if mu gt 15 then mu=mu-16
 rab(n,mu)=0.5*jaf*(verpos+conver) & rab(n,mr)=0.5*jaf*horpos & rab(mr,n)=rab(n,mr)
& rab(mu,n)=rab(n,mu)

 n= 15 & mu=n+8 & mr=n+1 & if mr/8*8 eq mr then mr=mr-8 & if mu gt 15 then mu=mu-16
 sab(n,mu)=-0.5*jab*(conver+verpos) & sab(n,mr)=-0.5*jab*conhor &
sab(mr,n)=conjugate(sab(n,mr)) & sab(mu,n)=conjugate(sab(n,mu))

 sab=conjugate(transpose(sab))
```

```
uber=dcomplexarr(32,32)
uber(0:15,0:15)=conjugate(sab)
uber(0:15,16:31)=-conjugate(rab)
uber(16:31,0:15)=rab
uber(16:31,16:31)=-sab

H = LA_ELMHES(uber, q,PERMUTE_RESULT = permute, SCALE_RESULT = scale)

; Compute eigenvalues

eigenvalues = LA_HQR(h, q, PERMUTE_RESULT = permute)

eigenvectors = LA_EIGENVEC(H, Q, PERMUTE_RESULT = permute, SCALE_RESULT = scale)

eigenvalues=float(eigenvalues)
ind=where(eigenvalues ge 0)
eigenvalues=eigenvalues(ind)
ss=sort(eigenvalues) & eigenvalues=eigenvalues(ss)
return,eigenvalues

 end
```

Bibliography

[1] Philip Phillips, *Advanced Solid State Physics*, Westview Press, Boulder, Colorado (2003).

[2] G.R. Stewart, Rev. Mod. Phys. **73**, 797 (2001); **78**, 743 (2006).

[3] L.D. Landau, JETP, Vol. 3, No. 6, p. 920 (1956).

[4] M. A. Ruderman and C. Kittel ,Phys. Rev. 96, 99 (1954).

[5] T. Kasuya, Prog. Theor. Phys. 16, 45 (1956).

[6] K. Yosida, Phys. Rev.106, 893 (1957).

[7] M. C. Aronson, R. Osborn, R. A. Robinson, J. W. Lynn, R.Chau, C. L. Seaman, and M. B. Maple ,Phys .Rev. Lett. 75, 725 (1995).

[8] A. Schröder G. Aeppli, R. Coldea, M. Adams, O. Stockert, H. Löhneysen, E. Bucher, R. Ramazashvili, and P. Coleman, Nature 407, 351 (2000).

[9] M. C. Aronson, R. Osborn, R. Chau, M. B. Maple, B. D.Rainford, and A. P. Murani, Phys. Rev. Lett. 87, 197205 (2001).

[10] W. Montfrooij, M. C. Aronson, B. D. Rainford, J. A. Mydosh, A. P. Murani, P. Haen, and T. Fukuhara, Phys. Rev. Lett. 91, 087202 (2003).

[11] J. Kondo, Prog. Theor. Phys. 32, 37 (1964); J. Phys. Soc. Jpn. 74, 1 (2005).

[12] P. W. Anderson, Journal of Physics C: Solid State Physics 3, 2436 (1970).

[13] K. Wilson, Rev. Mod. Phys. 47, 773 (1975).

[14] S. Sachdev, *Quantum Phase Transitions*, Cambridge University Press, Cambridge (1999).

[15] Sven Friedemann et al., New Journal of Physics 15, 093014 (2013)

[16] Qimiao Si *et al.*, Nature (London) **413**, 804 (2001).

[17] John A. Hertz, Phys. Rev. B **14**, 1165 (1976).

[18] A.J. Millis, Phys. Rev. B **48**, 7183 (1993).

[19] A.H. Castro-Neto and B.A. Jones, Phys. Rev. B 62, 14975 (2000).

[20] O.O. Bernal, D.E. MacLaughlin, H.G. Lukefahr, and B. Andraka, Phys. Rev. Lett. 75, 2023 (1995).

[21] S. Lipinski, Czech. J. of Phys. 52, 287 (2002).

[22] Yoshikazu Tabata, *Non-Fermi Liquid Behavior in* $Ce(Ru_{1-x}Rh_x)_2Si_2$, Gradaduate School of Science, Osaka University (2001).

[23] T. Endstra, G.J. Nieuwenhuys, and J.A. Mydosh, Phys. Rev. B48, 9595 (1993).

[24] T. Moriya and T. Takimoto, J. Phys. Soc. Jpn.64, 960 (1996).

[25] M. B. Fontes, M. A. Continentino, S. L. Budko, M.El-Massalami, L. C. Sampaio, A. P. Guimarães, E. Baggio-Saitovitch, M. F. Hundley, and A. Lacerda, Phys. Rev. B53 ,11678 (1996).

[26] D. Takahashi, S. Abe, D.A. Tayurskii, K. Matsumoto, H. Suzuki, and Y. Onuki, Phys. Rev. B67, 180407 (R) (2003).

[27] Hiroaki Kadowaki, Masugu Sato, and Shuzo Kawarazaki, Phys. Rev. Lett. 92, 097204 (2004).

[28] Hiroaki Kadowaki, Yoshikazu Tabata, Masugu Sato, Naofumi Aso, Stephane Raymond, and Shuzo Kawarazaki, Phys. Rev. Lett. 96, 016401 (2006).

[29] J. Flouquet, S. Kambe, L.P. Regnault, P. Haen, J.P. Brison, F. Lapierre, and P. Lejay, Physica B215, 77 (1995).

[30] G.L. Squires, *Introduction to the Theory of Thermal Neutron Scattering*, Dover Publications, Mineola, New York (1996).

[31] D.E. MacLaughlin, .H. Heffner, J.E. Sonier, G.J. Nieuwenhuys, R. Chau, M.B. Maple, B. Andraka, G.M. Luke, Y. Fudamoto, Y.J. Uemura, A.Amato, C. Baines, Phys. B: Condens. Matt. 289, 15 (2000).

[32] Bouchette, J. Phys. Cond. Matt. 13, 10901 (2001).

[33] Wouter Montfrooij, Tom Heitmann, Yiming Qiu, Shannon Watson, Ross Erwin, Wangchun Chen, Yang Zhao, Meigan Aronson, Yingkai Huang, and Anne de Visser, Phys. Rev. B99, 195113 (2019).

[34] T. Heitmann, J. Gaddy, J. Lamsal, and W. Montfrooij, J. of Physics conference series **391**, 012018 (2012).

[35] T. Willers, D. T. Adroja, B. D. Rainford, Z. Hu, N. Hollmann, P. O. Körner, Y.-Y. Chin, D. Schmitz, H. H. Hsieh, H.-J. Lin, C. T. Chen, E. D. Bauer, J. L. Sarrao, K. J. McClellan, D. Byler, C. Geibel, F. Steglich, H. Aoki, P. Lejay, A. Tanaka, L. H. Tjeng, and A. Severing, Phys. Rev. B 85, 035117 (2012).

[36] Michael Shatruk, Journal of Solid State Chemistry 272, 198 (2019).

[37] Shuzo Kawarazaki, Masugu Sato, Hiroaki Kadowaki, Yoshiyuki Yamamoto, and Yoshihito Miyako, J. Phys. Soc. Jpn. 66, 2473 (1997).

[38] W. Montfrooij, J. Lamsal, M. Aronson, M. Bennett, A. deVisser, H. Y. Kai, N. T. Huy, M. Yethiraj, M. Lumsden, and Y. Qiu, Phys. Rev. B76, 052404 (2007).

[39] S. Doniach, in *Valence Instabilities and Narrow Band Phenomena*, edited by R. Parks, Plenum (1977).

[40] T. Heitmann, J. Gaddy, and W. Montfrooij, J. of Mod. Phys. **5**, 649 (2014).

[41] Dietrich Stauffer and Amnon Aharony, *Introduction to Percolation Theory* CRC, Boca Raton, FL (1994).

[42] J. Gaddy, T. Heitmann, and W. Montfrooij, J. Appl. Phys. 115,17E110 (2014).

[43] M. J. Besnus, J. P. Kappler, P. Lehmann, and A. Meyer, Solid State Commun. 55, 779 (1985).

[44] A. Lacerda, A. de Visser, P. Haen, P. Lejay, and J. Flouquet, Phys. Rev. B 40, 8759 (1989).

[45] J.-G. Park, J. Phys.: Condens. Matt. 6, 9383 (1994).

[46] Tom Heitmann, Jagat Lamsal, Shannon Watson, Ross Erwin, Wangchun Chen, Yang Zhao, Wouter Montfrooij, AIP Advances 7, 055701 (2017).

[47] A. Amato, R. Feyerherm, F.N. Gygax, A. Schenck, J. Flouquet, and P. Lejay, Phys. Rev. B 50, R619 (1994).

[48] Takahashi et al., Physica B 284-288, 1269 (2000).

[49] Casimir and Du Pré, Physica 78 (Utrecht) 507 (1938).

[50] José A. Hoyos and Thomas Vojta, Phys. Rev. B **74**, 140401 (R) (2006).

[51] Tranquada, J., Sternlieb, B., Axe, J. et al. Nature 375, 561–563 (1995).

[52] L. Pintschovius, Physica Status Solidi B, vol. 242, no. 1, pp. 30–50 (2005).

[53] Coleman, P. Nature 410, 320–321 (2001).

[54] Y. Onuki, R. Settai, K. Sugiyama, T. Takeuchi, T. C. Kobayashi, Y. Haga, and E. Yamamoto, J. Phys. Soc. Japan 73, 769 (2004).

[55] S. Fayfar, A. Bretaña, and W. Montfrooij. Phys. Rev. E 104, 034110 (2021).

[56] S. Fayfar, A. Bretaña, and W. Montfrooij. J. Phys. Commun. 5 015008 (2021).

[57] A. Bretaña, S. Fayfar, and W. Montfrooij. Phys. Rev. B 104, 085135 (2021).

[58] J.M. Tranquada, Advances in Physics (2021).

[59] M. Fujita, H. Hiraka, M. Matsuda, M. Matsuura, J. M. Tranquada, S. Wakimoto, G. Xu, and K. Yamada, J. Phys. Soc. Jpn. 81, 011007 (2012).

[60] N.S. Headings, S.M. Hayden, J. Kulda, N. Hari Babu, and D.A. Cardwell, Phys. Rev. B 84, 104513 (2011).

[61] Wouter Montfrooij and Ignatz de Schepper, *Excitations in Simple Liquids, Liquid Metals ans Superfluids*, Oxford University Press, Oxford (2010).

[62] Trovarelli O, Geibel C, Mederle S, Langhammer C, Grosche F M, Gegenwart P, Lang M, Sparn G and Steglich F Phys. Rev. Lett. 85, 626 (2000).

[63] Gegenwart P, Custers J, Geibel C, Neumaier K, Tayama T, Tenya K, Trovarelli O and Steglich F Phys. Rev. Lett. 89, 056402 (2002).

[64] M. Yano, A. Sekiyama, H. Fujiwara, Y. Amano, S. Imada, T. Muro, M. Yabashi, K. Tamasaku, A. Higashiya, T. Ishikawa, Y. Ōnuki, and S. Suga Phys. Rev. B 77, 035118 (2008).

[65] P. Gegenwart, Y. Tokiwa† , J. Custers, C. Geibel and F. Steglich, J. Phys. Soc. Japan 75, 156 (2004).

[66] J. Custers, P. Gegenwart, H. Wilhelm et al. Nature 424, 524-527 (2003).

[67] J. Custers, P. Gegenwart, C. Geibel, F. Steglich, P. Coleman, and S. Paschen Phys. Rev. Lett. 104, 186402 (2010).

[68] P. Gegenwart, Y. Tokiwa, K. Neumaier, C. Geibel, F. Steglich Physica B 359-361 (2005).

[69] P. Gegenwart, J. Custers, Y. Tokiwa, C. Geibel, and F. Steglich Phys. Rev. Lett. 94, 076402 (2005).

[70] H. Tsujii, E. Tanaka, Y. Ode, T. Katoh, T. Mamiya, S. Araki, R. Settai, and Y. Ōnuki Phys. Rev. Lett. 84, 5407 (2000).

[71] B. Keimer, A. Aharony, A. Auerbach, R. J. Birgeneau, A. Cassanho, Y. Endoh, R. W. Erwin, M. A. Kastner, and G. Shirane, Phys. Rev. B 45, 7430–7435 (1992).

[72] P. W. Anderson, Science 235, 1196 (1987).

[73] B. Lake, D. A. Tennant, C. D. Frost, and S. E. Nagler, Nat. Mater. 4, 329–334 (2005).

[74] C. T. Chen, F. Sette, Y. Ma, M. S. Hybertsen, E. B. Stechel, W. M. C. Foulkes, M. Schulter, S.-W. Cheong, A. S. Cooper, L. W. Rupp, B. Batlogg, Y. L. Soo, Z. H. Ming, A. Krol, and Y. H. Kao, Phys. Rev. Lett. 66, 104–107 (1991).

[75] S. A. Trugman, Phys. Rev. B 37, 1597–1603 (1988).

[76] M. Fujita, K. Yamada, H. Hiraka, P. M. Gehring, S. H. Lee, S. Wakimoto, and G. Shirane, Phys. Rev. B 65, 064505 (2002).

[77] A. R. Moodenbaugh, Y. Xu, M. Suenaga, T. J. Folkerts, and R. N. Shelton, Phys. Rev. B 38, 4596 (1988).

[78] G. Yu, Y. Li, E. M. Motoyama, and M. Greven, Nat. Phys. 5, 873–875 (2009).

[79] J.M. Tranquada, G.D. Gu, M. H¨ucker, Q. Jie, H.J. Kang, R. Klingeler, Q. Li, N. Tristan, J.S. Wen, G.Y. Xu, Z.J. Xu, J. Zhou, and M. v. Zimmermann, Phys. Rev. B 78-174529 (2008).

[80] M. Dumm, S. Komiya, Y. Ando, and D.N. Basov, Phys. Rev. Lett. 91 (2003).

[81] M. Enoki, M. Fujita, T. Nishizaki, S. Iikubo, D.K. Singh, S. Chang, J.M. Tranquada, and K. Yamada, Phys. Rev. Lett. 110 (2013).

[82] R.J. Birgeneau, C. Stock, J.M. Tranquada, and K. Yamada, J. Phys. Soc. Jpn. 75 (2006).

[83] P. Dai, H.A. Mook, R.D. Hunt, and F. Dogan, Phys. Rev. B 63 (2001).

[84] Y. Sidis, S. Pailh‘es, B. Keimer, C. Ulrich, and L.P. Regnault, Phys. Stat. Sol. (b) 241 (2004).

[85] S. W. Tjablikow, *Quantentheoretische Methoden des Magnetismus*, B. G. Teubner (1968).

[86] J.M. Tranquada, AIP Conf. Proc. 1550, 114-187 (2013).

[87] S. Raghu, S.A. Kivelson, and D.J. Scalapino, Phys. Rev. B 81 (2010).

[88] E. Berg, E. Fradkin, E.A. Kim, S.A. Kivelson, V. Oganesyan, J.M. Tranquada, and S.C. Zhang, Phys. Rev. Lett. 99 (2007).

[89] N. N. Bogoliubov, Nuovo Cimento 7, 794 (1958).

[90] J. Custers, Private Communication (2022).

Figure D.1: Alex Bretaña in his first year at the University of Missouri working towards his Ph.d. in physics (this document).

VITA

Alex Bretaña was born in St. Louis, Missouri on May 25th, 1993 and graduated from Fort Zumwalt East High School in 2011.

Alex began attending the University of Missouri - St. Louis (UMSL) in 2011 as an undecided major but after falling in love with physics in Dr. Bernard Feldman's introductory physics lectures, he graduated with a Bachelor of Science in Physics in May 2016 from UMSL.

Alex began working towards his graduate degrees at the University of Missouri in August of 2016 and later joined Dr. Wouter Montfrooij's lab studying percolation and cluster formation in quantum critical systems.

Alex received his Master of Science Degree in Physics in July 2020 with Dr. Montfrooij as his adviser. Alex successfully defended his dissertation in April of 2022 and earned his Doctor of Philosophy in Physics.